Chapter 4. MESOSCALE AND SUBMESOSCALE PHYSICAL–BIOLOGICAL INTERACTIONS

GLENN FLIERL

Massachusetts Institute of Technology

DENNIS J. MCGILLICUDDY

Woods Hole Oceanographic Institution

Contents

1. Introduction

In the 1960s and 1970s, physical oceanographers realized that mesoscale eddy flows were an order of magnitude stronger than the mean currents, that such variability is ubiquitous, and that the transport of momentum and heat by transient motions significantly altered the general circulation of the ocean (see Robinson, 1983). Evidence that eddies can also profoundly alter the distributions and the dynamics of the biota began to accumulate during the latter part of this period (e.g., Angel and Fasham, 1983). As biological measurement technologies continue to improve and interdisciplinary field studies to progress, we are developing a clearer picture of the spatial and temporal structure of biological variability and its association with the mesoscale and submesoscale band (corresponding to length scales of ten to hundreds of kilometers

The Sea, Volume 12, edited by Allan R. Robinson, James J. McCarthy, and Brian J. Rothschild
ISBN 0-471-18901-4

and time scales of days to years). In addition, biophysical modelling now provides a valuable tool for examining the ways in which populations react to these flows.

Oceanic physics affects oceanic biology on a wide range of spatial and temporal scales. Stommel (1963) classified physical oceanographic phenomena in such terms, and Haury et al. (1978) built up an analogous view of the biology (see also Marquet et al., 1993). If we focus on the interactions between physics and biology, we can identify a number of distinct regimes in space–time. At the scale of an individual organism, the interaction is mediated through the forces the fluid applies to the organism, and vice versa (drag, propulsion, pressure, buoyancy), through the delivery of chemicals necessary for life and the removal of inimical ones, and through environmental conditions such as temperature which affect biochemical rates. At scales large enough to include multiple individuals, the fluid carries the signals that alert one organism to the presence of others, alter the encounter rates (Rothschild and Osborn, 1988), and mix the populations.

For larger scales, ocean physics plays a significant role in setting the spatial and temporal distributions of the biota. Primarily, the fluid flow acts to transport biological quantities, both by translation of the material contained in a water parcel at the flow velocity, *advection*, and by dispersal to neighboring parcels, *diffusion*. Both the steady component such as the general circulation (global or regional) and the unsteady parts such as surface and internal waves and mesoscale or submesoscale eddies can contribute to transport of organisms. Although biological movements, especially in the vertical, may overcome the fluid motions, most of the biota fit in the category of *plankton*, meaning that they are carried along by the water in its movement.

Mesoscale and submesoscale flows accommodate a diverse set of physical–biological interactions which influence the distribution and variability of various plankton populations in the sea. These complex, yet highly organized motions continually deform and rearrange the hydrographic structure of the near-surface region in which plankton reside. In the most general terms, the eddies have a twofold impact on the biota; in addition to transport, they can also modulate the rates of biological processes. The most common manifestations of the latter are associated with vertical movements which can affect the availability of both nutrients and light to phytoplankton and thereby alter the rate of primary production. Mesoscale and submesoscale flows can produce vertical motions in two different ways: (1) directly, as part of the inherent physics of baroclinic (vertically varying) flows and (2) indirectly, by interactions within the surface boundary layer between the eddy flows and those forced by the atmosphere.

In this chapter we examine mesoscale and submesoscale physical and biological dynamics, review and synthesize our existing understanding of the local impacts of the eddies, and discuss their effects on global-scale biological distributions.

2. Eulerian versus Lagrangian Models

2.1. Eulerian View

Some biological–physical models have been formulated in terms of the position, velocity, and state of each individual (see Chapter 12); however, the more common approach is to model the biological properties as *fields*, continuous functions of space and time representing properties such as the biomass per unit volume or the density of

particular species or even age/weight classes within species. For this kind of model, the governing equations simply state that changes in the amount of p_i material in a small volume are produced by fluxes across the surface bounding the volume and by internal changes associated with the biological dynamics; in differential form, this gives

$$\frac{\partial}{\partial t}\, p_i = -\nabla \cdot \mathbf{J}_i + \mathcal{P}_i(\mathbf{p}, \mathbf{x}, t)$$

where $\mathbf{J}_i$ is the flux (transport across a unit area normal to the vector per unit time) and $\mathcal{P}_i$ represents the rate of biological creation or destruction of the quantity.[1] The flux $\mathbf{J}_i$ includes the contributions from both the organized motion across the surface and the stochastic mixing, produced by random swimming or by physical processes—fluctuations in molecular motion or small-scale turbulence. The stochastic transport will be represented by the product of a tensor diffusivity κ_i and the gradient of the quantity. (We shall discuss the degree to which such a parameterization applies to mesoscale eddies below.) The flux from the organized movement is $\mathbf{V}_i p_i$, where the velocity $\mathbf{V}_i$ is the sum of the fluid motion $\mathbf{u}$ and directed swimming/sinking/floating $\mathbf{u}_{\text{bio}}$:

$$\mathbf{J}_i = \mathbf{V}_i p_i - \kappa_i\, \nabla p_i = \mathbf{u} p_i + \mathbf{u}_{\text{bio}} p_i - \kappa_i\, \nabla p_i$$

so that

$$\frac{\partial}{\partial t}\, p_i + \nabla \cdot (\mathbf{V}_i p_i) = \mathcal{P}_i(\mathbf{p}, \mathbf{x}, t) + \nabla \cdot \kappa_i\, \nabla p_i \tag{1}$$

Although working with such field equations is routine, we should not forget that many subtle and difficult questions arise in any attempt to derive them rigorously. For example, how valid is the continuum approximation—are the organisms densely distributed enough that we can get a good estimate of p_i and its derivatives. [See Siegel (1998), who examines some of the implications of the discrete nature of plankton distributions.] Are the encounter rates of predators and prey functions only of the densities, or do the details of the spatial/temporal probability distributions matter (e.g., what role does patchiness play)? Can we really know the mean velocities $\mathbf{u}_{\text{bio}}$ or understand what they depend on? If the biological movements are an important part of the diffusion, is the $\mathbf{J} = -\kappa_i\, \nabla p_i$ form really appropriate and is κ_i independent of the densities of the predators or of the prey? We cannot deal with such questions in any detail here, but wish to remind readers (especially modelers!) of the need for critical review of the assumptions built into any biological model.

2.2. *Advection: Lagrangian View*

We have presented the *Eulerian* description above (equation 1); the fields are represented by the values at fixed spatial points as functions of time, $\mathbf{p}(\mathbf{x},t)$. This approach

[1]Boldface is used to represent vectors, either three-dimensional for spatial locations and velocities or N-dimensional when used as a shorthand for the concentrations of N different biological variables, $\mathbf{p} = (p_1, p_2, \ldots, p_N)$.

to continuum dynamics offers advantages for both numerical implementation and incorporation of processes such as differential biological movement and diffusion, which exchange material beween fluid parcels. However, since we are considering complex space- and time-dependent flows and nonlinear biology, we are generally forced to rely on numerical simulations of these equations. Although such calculations produce estimates of the transport by the flow directly, it can be quite difficult to sort out the less direct effects—the interaction with the biological dynamics and the alteration of the local densities, which, in turn, modifies the fluxes.

There is a second way of describing continuum fields in fluids—the *Lagrangian* description—which can be helpful in understanding the effects of flow. Conceptually, we think of marking a fluid parcel by putting dye in a small region and then recording the time dependence of the biological quantities in the dyed area, wherever it may move. The Lagrangian description generally assumes that any biologically determined velocities are the same for all interacting components (e.g., predator–prey) occupying the volume; differential movement would imply that the interactions could no longer be restricted to a single fluid parcel. Thus, this approach is appropriate for an advection-dominated system, with either a homogeneous population or, more likely, components that do not move with respect to the water.

We shall distinguish the Lagrangian description of a field $\tilde{\mathbf{p}}_i(\mathbf{x}_0,t)$ by a tilde and note that it is parameterized by the initial position of the fluid parcel, $\mathbf{x}_0$, and time. The fluid physics and biological movement determine the trajectories $\tilde{\mathbf{x}}(t)$:

$$\frac{d}{dt}\,\tilde{\mathbf{x}}(\mathbf{x}_0,t) = \mathbf{V}_i(\tilde{\mathbf{x}}(\mathbf{x}_0,t),t), \qquad \tilde{\mathbf{x}}(\mathbf{x}_0,0) = \mathbf{x}_0$$

In this representation, the biological dynamics is simpler:

$$\frac{d}{dt}\,\tilde{p}_i(\mathbf{x}_0,t) = \mathcal{P}_i(\tilde{\mathbf{p}},\tilde{\mathbf{x}}(t),t) \tag{2}$$

but the trajectory calculations can be difficult, processes that exchange properties with the surroundings are not easily included, and building a picture of the spatial distribution from information on a set of complex, intertwined trajectories can be difficult. The Eulerian and Lagrangian descriptions are related by

$$\mathbf{p}(\tilde{\mathbf{x}}(t),t) = \tilde{\mathbf{p}}(\mathbf{x}_0,t)$$

That is, if we track a parcel initially at $\mathbf{x}_0$ and find it is at a particular location at time t, the Eulerian description must have the same value for the quantity at that particular point and time.

The dynamical equation 2 makes it clear that the effects of advection are twofold:

1. The flow transfers temporal variability into spatial variability (i.e., equation 2 gives us $\mathbf{p}$ not at a fixed location but at a moving location). If we do wish to know what value of $\mathbf{p}$ would be observed at a particular location $\mathbf{x}_{\text{obs}}$ at time t_{obs}, we can, in principle, back the trajectory up to find the initial position, apply the initial condition at that point, and then integrate forward to

find $\mathbf{p}(\mathbf{x}_{\text{obs}}, t_{\text{obs}})$. Robinson (1997) considers several flow patterns and gives an excellent summary of the types of temporal-spatial patterns which can arise from pure advection.

2. The flow also converts spatial variation of the environment or parameters into explicit time variations in the coefficients of the equation. If the biological interaction terms do depend explicitly on space, meaning that one or more parameters is a function of $\mathbf{x}$, the motion of the parcel sweeps such a parameter through a range of values over the time history of the parcel.

Both of these effects can be important. For example, we can think of the release of pelagic larvae from a benthic organism as an example of temporal development giving spatial patterns as the flow transports the larvae from the spawning site, so that the different stages appear at different downstream locales. But the survival rate could also depend on space (e.g., particular spots may harbor predators) so that the second effect also comes into play. When discussing the influence of ocean eddies, we must include both processes.

As an example, let us consider phytoplankton in a light field which decays exponentially with depth subject to eddy-induced vertical motions, idealized as a near-surface strain field varying sinusoidally in time:

$$\mathbf{u} = \alpha \cos(\omega t) \times (-x, 0, z)$$

The vertical position satisfies

$$\frac{d}{dt}\,\tilde{z} = \alpha \cos(\omega t)\tilde{z}$$

and the trajectories are given by

$$\tilde{z} = z_0 \exp\left(\frac{\alpha}{\omega} \sin\, \omega t\right)$$

with z_0 related to the average depth of the parcel by

$$\langle \tilde{z} \rangle = z_0 I_0 \left(\frac{\alpha}{\omega}\right)$$

(I_0 being the modified Bessel function); the ratio $\langle \tilde{z} \rangle / z_0$ increases as the amplitude increases, since the parcels of fluid have larger downward excursions than upward ones (Fig. 4.1).

Consider a simple biological model where we assume that phytoplankton grow at a rate that is proportional to the light level and have a death rate that increases with the population density

$$\frac{d}{dt}\,\tilde{P} = r_0 e^{\tilde{z}/h}\tilde{P} - d_0\tilde{P} - d_1\tilde{P}^2 \tag{3}$$

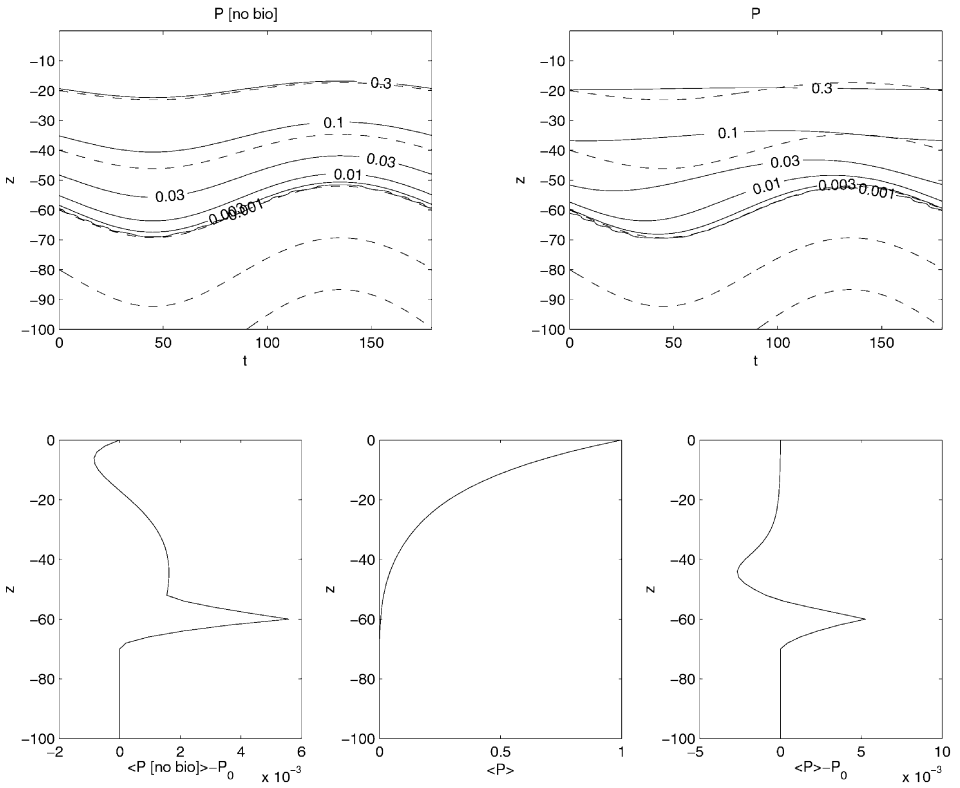

Fig. 4.1. Trajectories under periodically varying strain field (dashed curves), the phytoplankton concentration (solid curves) and the difference between the time mean and P_0. Left, purely advected case; right, including biological dynamics. The lower middle picture shows $\langle P \rangle$.

In the absence of motion, the equilibrium distribution is simple:

$$P_0(z) = \begin{cases} \dfrac{r_0}{d_1}\, e^{z/h} - \dfrac{d_0}{d_1}, & z > -h(\ln r_0 - \ln d_0) \\ 0, & \text{below} \end{cases}$$

To illustrate just the transformation of spatial to temporal/spatial variability, consider the case in which we start with the state above and simply turn on advection without permitting any biological changes ($\mathcal{P} = 0$):

$$\frac{d}{dt} P_{[\text{no bio}]} = 0 \Rightarrow \tilde{P}_{[\text{no bio}]}(z_0, t) = P_0(z_0) \Rightarrow P_{[\text{no bio}]}(\tilde{z}(z_0, t), t) = P_0(z_0)$$

Figure 4.1 shows the time history of $P_{[\text{no bio}]}$ and the mean values observed at different depths (note that these means will depend critically on the initial conditions).

When the biological terms are also active, so that the environmental variability

along the path comes into play, the system comes into a final oscillatory state (Fig. 4.1) that is independent of the initial conditions (as long as P is nonzero along trajectories that can support some population). In the surface regions, the biological terms dominate and we see little effect from the movements; at the deepest level, advection is dominant and P is nearly constant on trajectories. At intermediate depths, both factors enter, and P oscillates but is out of phase with the displacements because the time scales for growth at these depths are comparable to the period of the motion. The deviations from the rest state P_0 now depend on ratios of the growth rate, r_0 or d_0, the frequency, ω, and amplitude, α, of the motion.

We can see from this example some of the differences between the Lagrangian and Eulerian means. To find the average following the motion, we divide equation 3 by $\tilde{P}$ and integrate over the period (usually different from the Eulerian period, but not in this case)

$$\langle \tilde{P} \rangle = \frac{r_0}{d_1 T} \left[\int_0^T dt \exp\left(\frac{\tilde{z}(t)}{h} \right) \right] - \frac{d_0}{d_1}$$

The Lagrangian average values are higher than P_0 would be at the average depth of the trajectory (Fig. 4.1) for the reasons given by Holloway (1984) and Joyce (1988): The curvature in the light field implies that the increase while the phytoplankton are near the surface is larger than the decrease while they are deep. The Eulerian picture is more complicated: The deep mean values are increased because some plankton are temporarily carried below the depths where they would normally die or do less well, but then are returned to higher light levels. Nearer the surface, however, $\langle P \rangle$ is reduced by the eddy fluxes, which are on average negative—downward-moving water has higher P levels than upward-moving water, since the former has recently passed through higher light levels (see the trajectory crossing 30 m in Fig. 4.1). In effect, this loss acts as an increase in the death rate, reducing the supportable population. The vertically integrated amount of phytoplankton is not significantly altered by the fluid motion; however, changes in the mean properties do occur with more complex biological models.

3. Biological Dynamics

The subject of biological modeling is, of course, huge (see Murray, 1990), and we address only a few relevant aspects that arise when building a model of a biological system for incorporation with a physical model. To be compatible with Eulerian advection and diffusion, the variables must represent densities (amount per unit volume or per unit mass of water) of the property. If, for example, p_k is the number per unit volume of euphausiids of age k, we can mix water containing 5-day-old animals with another parcel containing 10-day-olds to obtain water with nonzero values for both p_5 and p_{10}. In contrast, a variable such as euphausiid age cannot really be diffused properly (especially when we try to mix with water that has no euphausiids). The biological reaction terms $\mathcal{P}_i$ must be local, expressing the rates of changes of properties within a blob of fluid in terms of the values of all the variables in that blob. Again, it is important to review and reexamine critically the choices built into our models, so that we can develop a sense of how general the results might be.

Modelers have approached biological dynamics in two different ways, depending on their objectives. *Food web* models consider processes that transfer material such as carbon or nitrogen from one group of organisms to another or to a particulate or dissolved phase. (Frequently, nitrogen is used because it may limit the uptake; however, problems with more than one limiting substance are increasingly interesting.) Thus, we might consider a model with several trophic levels, with phytoplankton, which take up carbon from the inorganic pool, being consumed by zooplankton, which are, in turn, eaten by fish (Fig. 4.2*a*); when these die, they produce detritus, which bacteria turn back into inorganic material. As variables, we might use the carbon content of each group. *Structured population models* represent the life cycle of a particular species, such as a copepod, from hatching, through larval and copepodid stages, to adults. The variables might be the number in each of the stages, and the dynamics will represent the birth, death, and molting processes that alter these numbers (Fig. 4.2*b*). Which of these approaches (or a hybrid such as splitting the zooplankton into different stages and classifying the larval fish by their weight, etc.) one chooses depends on the questions one wishes to answer. Unfortunately, we have no assurance that the dynamics of interest is not strongly affected by our vast simplifications of the natural system. Thus, we generally have to regard our models as ways of exploring processes, rather than as exact simulations, especially for the long time scales characterizing mesoscale eddies.

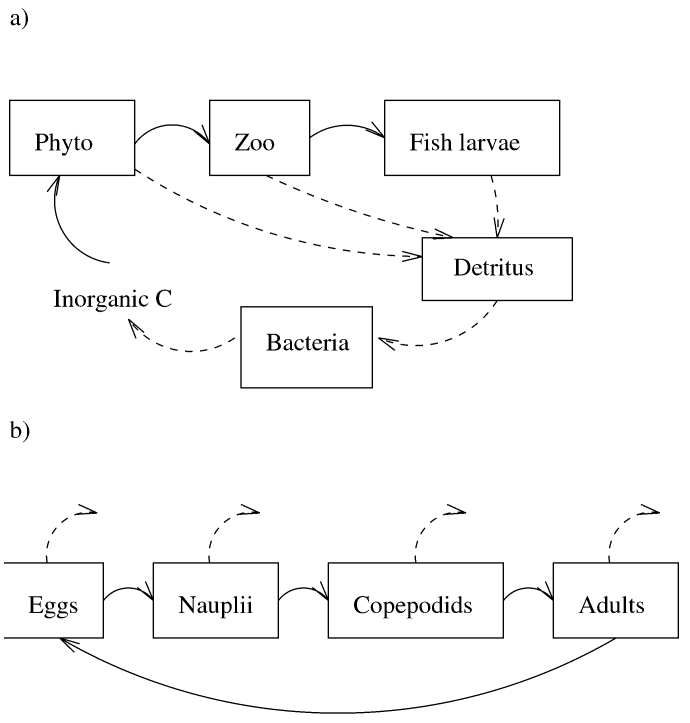

Fig. 4.2. (*a*) Food web and (*b*) structured population models. The solid arrows show transfers of carbon or numbers per cubic meter from box to box. The dashed arrows represent losses by processes such as excretion, predation, and death.

3.1. Examples

In much of the rest of the chapter, we consider two examples: a typical nutrient/phytoplankton/zooplankton system

$$\begin{aligned}
\frac{\partial}{\partial t} P + \nabla \cdot (\mathbf{u}P) &= \nabla \cdot \kappa \, \nabla P + \text{uptake}(P, N) - \text{grazing}(P, Z) - \text{death}(P) \\
\frac{\partial}{\partial t} Z + \nabla \cdot (\mathbf{u}Z + \hat{\mathbf{z}} w_Z Z) &= \nabla \cdot \kappa \, \nabla Z + \text{assimilation}(P, Z) - \text{death}(Z) \\
\frac{\partial}{\partial t} N + \nabla \cdot (\mathbf{u}N) &= \nabla \cdot \kappa \, \nabla N - \text{uptake}(P, N) + \text{supply}(N) \\
&\quad + \text{regeneration}(P, Z)
\end{aligned} \tag{4}$$

(see Steele, 1974, Sarmiento et al., 1993, for two examples among many) and an age-stage structured copepod model (Davis, 1984).

The NPZ equations 4 are similar to a wide variety of models that aggregate various components of the planktonic ecosystem using a single currency (e.g., nitrogen). Such models range in complexity from three components (e.g., Steele and Henderson, 1981; Frost, 1993) to more sophisticated formulations that treat dissolved organic materials and the microbial loop (e.g., Fasham et al., 1990) and even species or functional groups within particular classes of organisms (e.g., Moisan and Hofmann, 1996). We consider the conservative version of equations 4 with any nitrogen that leaves the phytoplankton or zooplankton compartments turning immediately into dissolved nutrient. We use the Michaelis–Menten (1913) form for the uptake and the Ivlev (1955) form for the grazing:

$$\begin{aligned}
\text{uptake}(P, N) &= u e^{z/h} \, \frac{PN}{N + k_s} \\
\text{grazing}(P, Z) &= \frac{g}{v} \, Z(1 - e^{-vP}) \\
\text{death}(P) &= d_P P \\
\text{assimilation}(P, Z) &= a \times \text{grazing}(P, Z) \\
\text{death}(Z) &= d_Z Z \\
\text{supply}(N) &= 0 \\
\text{regeneration}(P, Z) &= d_P P + d_Z Z + (1 - a) \times \text{grazing}(P, Z)
\end{aligned} \tag{5}$$

with h being the e-folding depth for the light. The last two ensure that the NPZ system is conservative, with the volume-integrated $N_T \equiv P + Z + N$ constant in time. Indeed, we can replace the N equation with

$$\frac{\partial}{\partial t} N_T + \nabla \cdot (\mathbf{u} N_T + \hat{\mathbf{z}} w_Z Z) = \nabla \cdot \kappa \nabla N_T$$

which implies that N_T will become uniform in the absence of zooplankton swimming.[2] Note that $N = N_T$ deep in the water column where the light level is too low to support phytoplankton. In this biological model and, we might infer, in much more complex models, biological transport (swimming, sinking of detritus, etc.) plays an important role in setting the structure of the deep nutrient fields.

For the copepod model, the primary variables are the number per unit volume in a particular age class within a particular stage (e.g., 3-day-old nauplii). The number densities then satisfy

$$\frac{\partial}{\partial t} n_i + \nabla \cdot (\mathbf{u} n_i) = \nabla \cdot \kappa \nabla n_i + L_{ij} n_j \tag{6}$$

with L_{ij} a matrix containing the probabilities of surviving, molting, and reproducing. In general, the elements in L_{ij}, especially the reproduction terms, can depend on the population density $\mathbf{n}$; indeed, nonlinearity is essential to prevent indefinite growth of the population in the long term. (Of course, it can also lead to complex dynamics; see Caswell, 1989). We will be studying this model for shorter time scales and will simply specify the new eggs n_1 as a function of time and space. We can then use constant values for the matrix elements. The complexity then arises from the large number of variables, 150 to 200 age-stage classes in the Davis (1984) model.

3.2. Equilibria and Stability

In the absence of motion or mixing, the dynamics of the biological system is characterized by the equilibria, their stability, and the attractors. The equilibria correspond to points $\mathbf{p} = \overline{\mathbf{p}}$, where

$$\mathcal{P}_i(\overline{\mathbf{p}}, \mathbf{x}, t) = 0 \tag{7}$$

We cannot expect to find steady solutions when the interaction terms depend explicitly on time (although we can look at quasisteady cases); however, the equilibria even in the time-independent case are still functions of $\mathbf{x}$, so that the solutions will have significant gradients that can be acted on by advection and diffusion.

For our NPZ model, we show the equilibrium solution as a function of depth in Fig. 4.3. In the upper water column, the phytoplankton have a constant value, fixed by the grazing, which reduces P down to the level where the zooplankton stop growing. Higher nutrient uptake near the surface supports higher values of Z. At the bottom of the euphotic zone, the zooplankton die out, leaving a very thin transition region where there is enough light to support phytoplankton but not enough of them to support zooplankton. A few meters deeper and the light level is too low, leaving only nutrients.

[2] Mathematically, the system is also reduced in order by one; we can solve just the P and Z equations, using $N = N_T - P - Z$ in the uptake term.

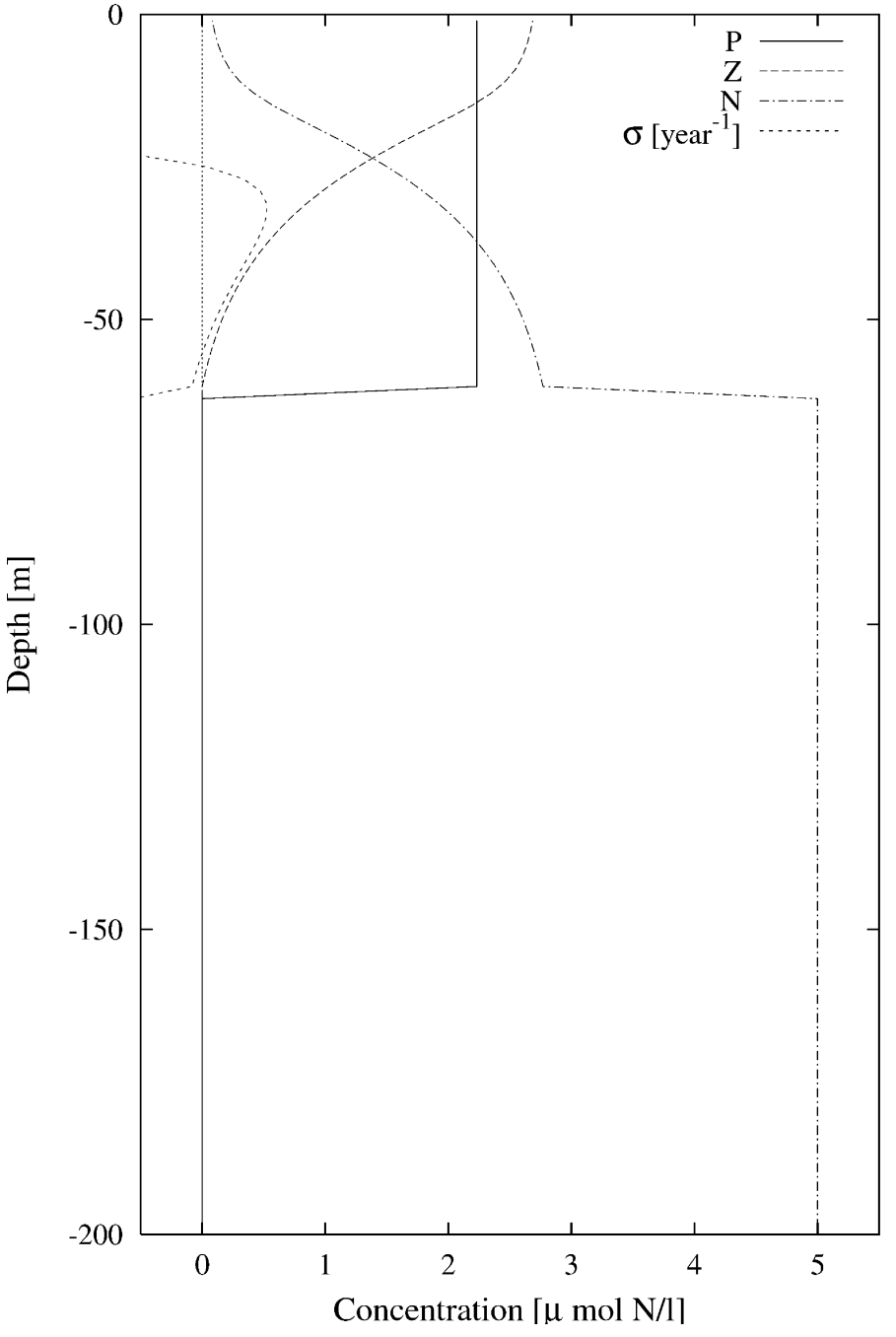

Fig. 4.3. Equilibria for equation 4 as functions of depth. The dotted line shows the growth rate σ for perturbations to the biological variables at the particular depth, ignoring any coupling between different depth ranges. The parameter values (in units of μmol N and days) that we have used are: $u = 0.6$, $k_s = 0.1$, $N_T = 5$, $d_P = 0.016$, $g = 0.1$, $v = 0.1$, $a = 0.4$, $d_Z = 0.08$, $h = 17$ m.

TABLE I
Stability of NPZ Model

Depth Range (m)	Basic State	Eigenvalues	Nonlinear Structure
0–10	$P+Z$	Real, <0 monotonic stability	Stable point
10–20	$P+Z$	Complex, Re < 0, stable spiral	Spiral to stable point
20–45	$P+Z$	Complex, Re > 0, unstable spiral	Stable limit cycle
45–55	$P+Z$	Complex, Re < 0, stable spiral	Spiral to stable point
55–60	P	Real, < 0 monotonic	Decay of Z
>60	N only	Real, < 0 monotonic	Decay to 0

Once we know the equilibria, we can compute their stability, using the linearized equations

$$\frac{\partial}{\partial t} p_i' = \frac{\partial \mathcal{P}_i}{\partial p_j} p_j'$$

The eigenvalues σ of the matrix $\mathcal{P}_{ij} \equiv \partial \mathcal{P}_i / \partial p_j$ determine whether trajectories near the equilibrium point will return to it (if all Re $\sigma < 0$) either directly (Im $\sigma = 0$) or as damped oscillations (Im $\sigma \neq 0$). Alternatively, the equilibrium point may be unstable with some trajectories diverging from the neighborhood of the equilibrium (some Re $\sigma > 0$) directly or as a growing oscillation. For our example, the stability calculation shows a complex structure (Table I) with monotonic stable points, stable spirals, and unstable spirals. As is typical, the stability properties depend strongly on the parameters; for example, the profile with $N_T = 3$ is everywhere stable, while that with $N_T = 10$ is unstable from the surface to nearly the bottom of the euphotic zone.

3.3. *Physically Induced Perturbations*

We have looked at the effects of the flow with a Lagrangian approach; let us now consider the ways they enter in the Eulerian system, equation 1. We can gain insight into the dynamics by regarding the perturbations induced by the flow and diffusion as small (even though this may not be always the case). If we write $\mathbf{p} = \bar{\mathbf{p}}(\mathbf{x}) + \mathbf{p}'(\mathbf{x}, t)$, where $\bar{\mathbf{p}}(\mathbf{x})$ is the equilibrium state considering only the biological processes described above, and then linearize the biological interaction terms, we have

$$\frac{\partial}{\partial t} p_i' = \frac{\partial \mathcal{P}_i}{\partial p_j} p_j' - \nabla \cdot (\mathbf{V}_i \bar{p}_i) + \nabla \cdot \kappa_i \nabla \bar{p}_i \tag{8}$$

The spatial structure in the parameters leads to gradients in the equilibrium states; the flow and diffusion working against these gradients generate time-dependent or steady forcing of biological perturbations. The response to this forcing—the distance the system moves away from equilibrium—is proportional (in a sense to be discussed below) to the time scale for decay of biological perturbations to the local equilibrium. For a particular biological model, there will be an entire set of such decay rates (given by the eigenvalues of $\mathcal{P}_{ij}$) corresponding to different biological structures (the associated eigenvectors), and both will vary from place to place. Since these time

scales are sensitive to the exact choices for the biological reaction terms, we can expect that response to eddy motions will be rather model-dependent.

To understand fully the impact of ocean eddies on the biology, then, we need to examine both the processes that produce spatially variable biology in the absence of flow (recognizing that temporal variability in $\mathcal{P}_i$ can be significant also) and the development of biological perturbations. However, there are additional, more subtle aspects that we may need to consider as well; in particular, the equilibrium states may depend on quantities such as the amount of dissolved nutrient in the deep water, which, in turn, is set by the remineralization process and transport by the general circulation and by the eddies. To approach such problems, we write explicit equations for both the mean field (which we can think of as the expected value when we take lots of experiments from an ensemble of initial eddy field conditions) and for the perturbations.

Mean Field Form

We shall consider a simple version of the mean field equations where we assume that the system is statistically homogeneous in the horizontal directions and that the biological component of the velocity—the swimming—is at most vertical and varies only with depth: $\mathbf{V}_i = \mathbf{u} + w\hat{z} + \varpi_i(z)\hat{z}$, where $\mathbf{u}$ is the horizontal component of the fluid velocity, w the vertical component, $\hat{z}$ the local vertical unit vector, and $\overline{\omega}_i$ represents the biological motion relative to the water. Then

$$\frac{\partial}{\partial t}\,\overline{p}_i + \frac{\partial}{\partial z}\,\varpi_i\overline{p}_i = \mathcal{P}_i(\overline{p}) + \frac{1}{2}\,\frac{\partial^2\mathcal{P}_i}{\partial p_j \partial p_k}\,\overline{p_j' p_k'} - \frac{\partial}{\partial z}\,\overline{w' p_i'} + \frac{\partial}{\partial z}\,\kappa_i\,\frac{\partial}{\partial z}\,\overline{p}_i$$

$$\frac{\partial}{\partial t}\,p_i' + \overline{\mathbf{u}}\cdot\nabla p_i' + \frac{\partial}{\partial z}\,\varpi_i p_i' = \mathcal{P}_i(\overline{p} + \mathbf{p}') - \mathcal{P}_i(\overline{p}) - w'\,\frac{\partial}{\partial z}\,\overline{p}_i + \nabla\kappa\,\nabla p_i'$$

$$\simeq \mathcal{P}_{ij} p_j' - w'\,\frac{\partial}{\partial z}\,\overline{p}_i + \nabla\kappa\,\nabla p_i' \tag{9}$$

Now the perturbations induced by the eddies acting upon the mean feed back upon the structure of the mean. This interaction takes place in two ways: (1) the vertical eddy flux of a property $\overline{w' p_i'}$ can be convergent or divergent, and (2) the biological nonlinearities are altered in the mean. The eddy flux can be understood simply: Upwelling water will usually carry higher nutrients than downwelling water which has passed through high-light regions where the phytoplankton are able to use and deplete the dissolved nutrient. Even in a case with equal amounts of upwelling and downwelling, there will be a net upward flux of nutrients. The eddy effects on the biological reaction terms arise from the simple fact that the mean of the product of two fluctuating series is not the same as the products of the means $\overline{PN} \neq \overline{P}\;\overline{N}$.

In principle, when the biological dynamics is stable at every point, we should be able to solve the forced problem (with the $w'\;\partial/\partial_z\;\overline{p}_i$ generating time- and space-dependent fluctuations) and determine the mean and transient response. Several difficulties may occur with such a program: (1) the nonlinearity in the biological reaction terms may be strong enough that the linearization of the perturbation equation may not be valid, and (2) the assumption that the $\overline{\mathbf{p}}$ equilibrium is stable may not hold.

In some cases, vertical diffusion can stabilize the system overall, by balancing the

growth in the unstable region with outward diffusive fluxes. This can happen when the diffusive time scale $\delta z^2/\kappa$ required to spread across the unstable band of width δz is smaller than the growth time, $1/\mathrm{Re}(\sigma)$. To find the conditions more precisely, we need to solve the stability problem, including the diffusion (and mean vertical motions such as migration or sinking, as well):

$$\sigma p_i' = \mathcal{P}_{ij} p_j' + \frac{\partial}{\partial z}\ \kappa\ \frac{\partial}{\partial z}\ p_i'$$

and look for globally growing modes. We have done this for the NPZ model by discretizing in the vertical and finding the largest growth rate for coupled modes, then adjusting κ until $\sigma = 0$; the result is $\kappa = 3 \times 10^{-4}$ cm^2 s^{-1} (smaller than the estimate above, presumably because the diffusion couples the growing mode and the damped modes present in the purely biological problem).

A second possibility is that the growing perturbations can change the mean values in such a way that the mean fields become stable again. This happens in a number of fluid problems; for example, convection alters the mean vertical profile until it is very close to stable.

3.4. Unstable Points, Limit Cycles, and Chaos

What happens when the equilibrium is truly unstable? For the purely biological dynamical system, we can examine the trajectories in phase space (which has p_1, p_2, p_3, ... as coordinates). For a two-component system, the trajectories have a limited flexibility, since they cannot cross each other. They must either condense to a point or to a stable limit cycle. These are known as *attractors* and are characterized by the convergence of the rates-of-change vectors nearby.

We illustrate the nonlinear behavior of our example NPZ system by showing the phase-plane diagrams at different vertical levels (Table 4.1, Fig. 4.4). The unstable spirals (around depths of 30 m) can be seen to result in limit cycles; in other parts of the water column, the equilibrium is stable and approached either monotonically (though perhaps with a bloom in P) or in a damped oscillation.

The two-component system can exhibit other behaviors of interest for models of ocean dynamics. For example, a so-called "type 3" grazing function

$$\mathrm{grazing}(P, Z) = gZ\ \frac{P^2}{P^2 + k_P}$$

with curvature of both signs leads to a structure characterized as an *excitable medium* (Truscott and Brindley, 1994). We can characterize the behavior by examining the phase plane (Fig. 4.5), which shows the evolution from various initial values of P and Z and also the *null clines*—lines (or surfaces) where $\mathcal{P}_i = 0$. The equilibria are intersections of these null clines; in the excitable medium case there is one such intersection off the axes, and it corresponds to a stable equilibrium (but would be unstable if it were on the right side of the minimum in the $\mathcal{P}_1$ null cline rather than on the left). However, small perturbations that leave the system below the local minimum in the null cline $\mathcal{P}_1 = 0$ will lead to large swings as P increases to the other branch

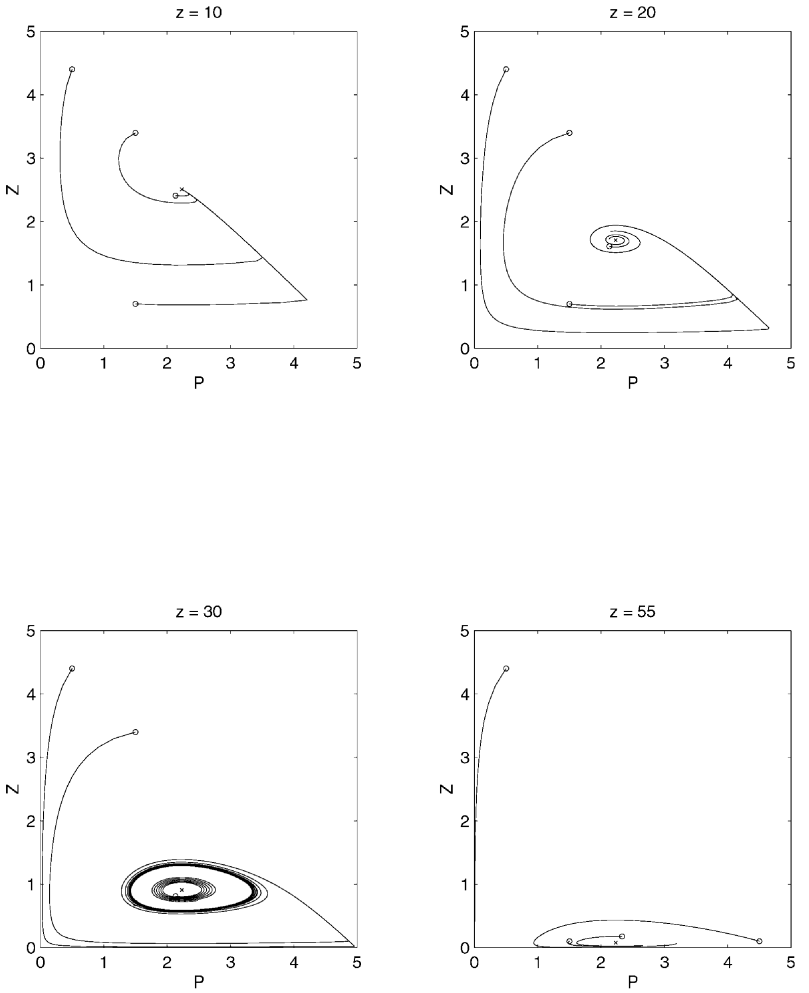

Fig. 4.4. Phase-plane diagrams at different depths showing characteristic trajectories.

and then returns (Fig. 4.5*a*). Thus, this kind of system will be particularly sensitive to the forcing provided by the physics.

Another form giving large responses is the multiple equilibria system (Fig. 4.5*b*) which we construct by changing the zooplankton death to a quadratic function (Steele and Henderson, 1981). For some parameter values, we find two stable states, with an unstable equilibrium in between. For other parameters, we have only a single, non-trivial, stable equilibrium or only the trivial solution. Small changes in the parameters can lead to switching states. In both of these cases, the linear equations are not adequate to describe the fluctuations.

As we move to three or more components, the trajectories can become much more complex (see Hastings and Powell, 1991). Attractors may still exist, but they can be of high enough dimension that trajectories can move chaotically on them. For example, adding a higher trophic level (e.g., fish)

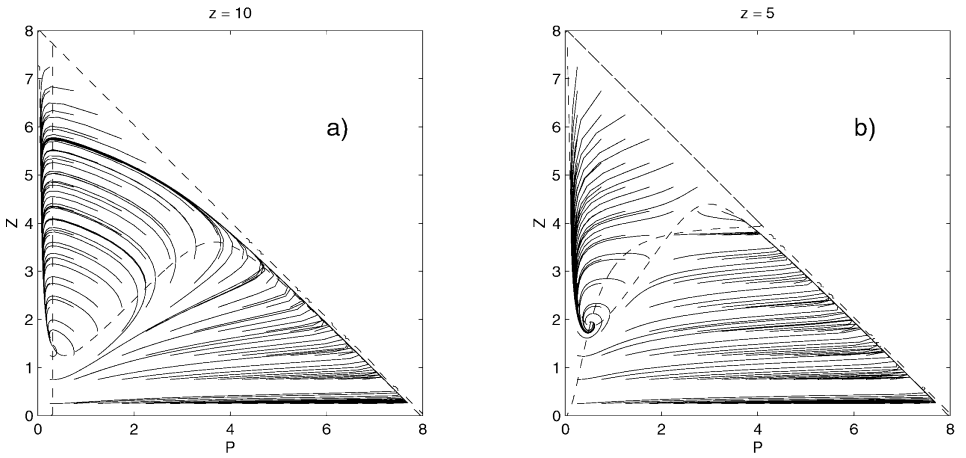

Fig. 4.5. Null clines [dashed curves, $\mathcal{P}_1 = 0$ descends from upper left to a minimum, rises to a maximum, and the proceeds toward $P = 5$; $\mathcal{P}_2 = 0$ is vertical on (*a*) and rises from the origin and levels out in (*b*)] and trajectories for (*a*) excitable media case and (*b*) multiple equilibrium case.

$$\frac{\partial}{\partial t} F + \nabla \cdot (\mathbf{u}F + \mathbf{u}_F F) = \nabla \cdot \kappa_F \nabla F + \text{feeding}(F, Z) - \text{death}(F)$$

can give erratic cycles even in the absence of flow (Fig. 4.6).

Advection-diffusion acting on such more naturally time-dependent systems may be expected to have significant effects, perhaps even causing chaotic motion (Pascual, 1993). In such cases we can no longer ignore the nonlinearity in the fluctuation equations and will have to examine the dynamics in detail, usually via numerical simulation.

3.5. Time-Dependent Coefficients

As we have seen, one of the primary effects of the physics, viewed in the Lagrangian frame, is to cause variations in the parameters of the biological model. For example, the light levels alter as a parcel moves vertically, and these changes result in different photosynthesis rates for phytoplankton. Variable coefficients can lead to periodic, quasiperiodic, or chaotic behavior (Strogatz, 1994). Even in the two-component system, variations in the coefficients allow trajectories starting from the same point to have different histories, and a single trajectory can now fill (in the fractal sense) spatial regions. In Fig. 4.7 we show an example in which the depth of a parcel oscillates by 3.5 m around the nominal depth of 30 m with a period of 181 days. The biological model is the NPZ model discussed above; it has a limit cycle in the unperturbed case. We also show the excitable media and multiple equilibrium cases.

We close this section with some cautionary remarks. As modelers, we often do not fully explore the dynamical system structure of a biological model to determine its behavior over reasonable ranges of the parameters or consider seriously the effects of using alternative functional forms. Indeed, we often assume that the ocean should be rather regularly behaved and select a model that has a very stable equilibrium

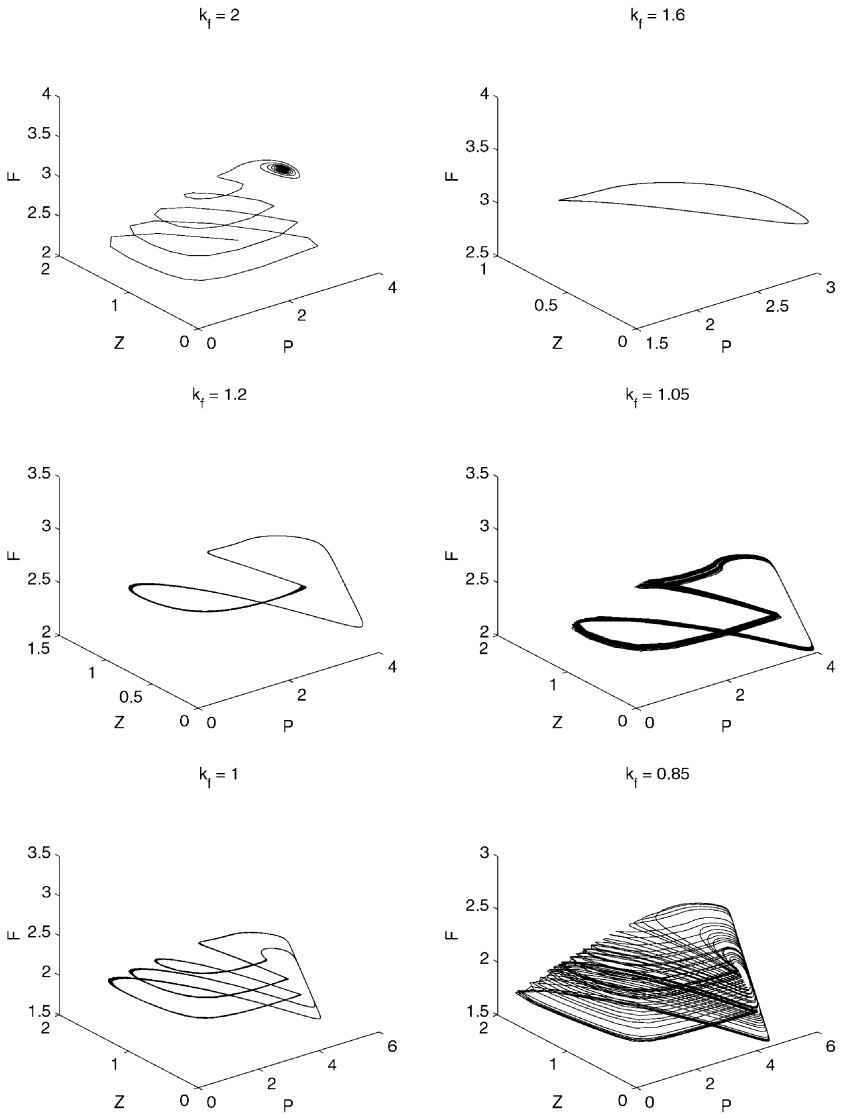

Fig. 4.6. Transition to chaos in the three-component model, with feeding = $a_f g_f ZF/(k_f + Z)$, death (F) = $d_f F$, death (Z) = feeding/a_f, and $N = N_T - P - Z - F$. Plots show spiral approach to stable point, limit cycles (including multiple periods) and chaos.

point (e.g., by using a Z^2 death term); variability then arises from the physics and/or external imposed stochastic events (wind events, predation, anthropogenic influences, etc.). However, it is quite likely that the biology of interest, when considered more fully, may have intrinsic oscillatory or chaotic time dependence. Since the response to physical variability will differ depending on the nature of the attractors, whether equilibria, limit cycles, or chaotic, we may still be missing important elements of the biophysical interactions.

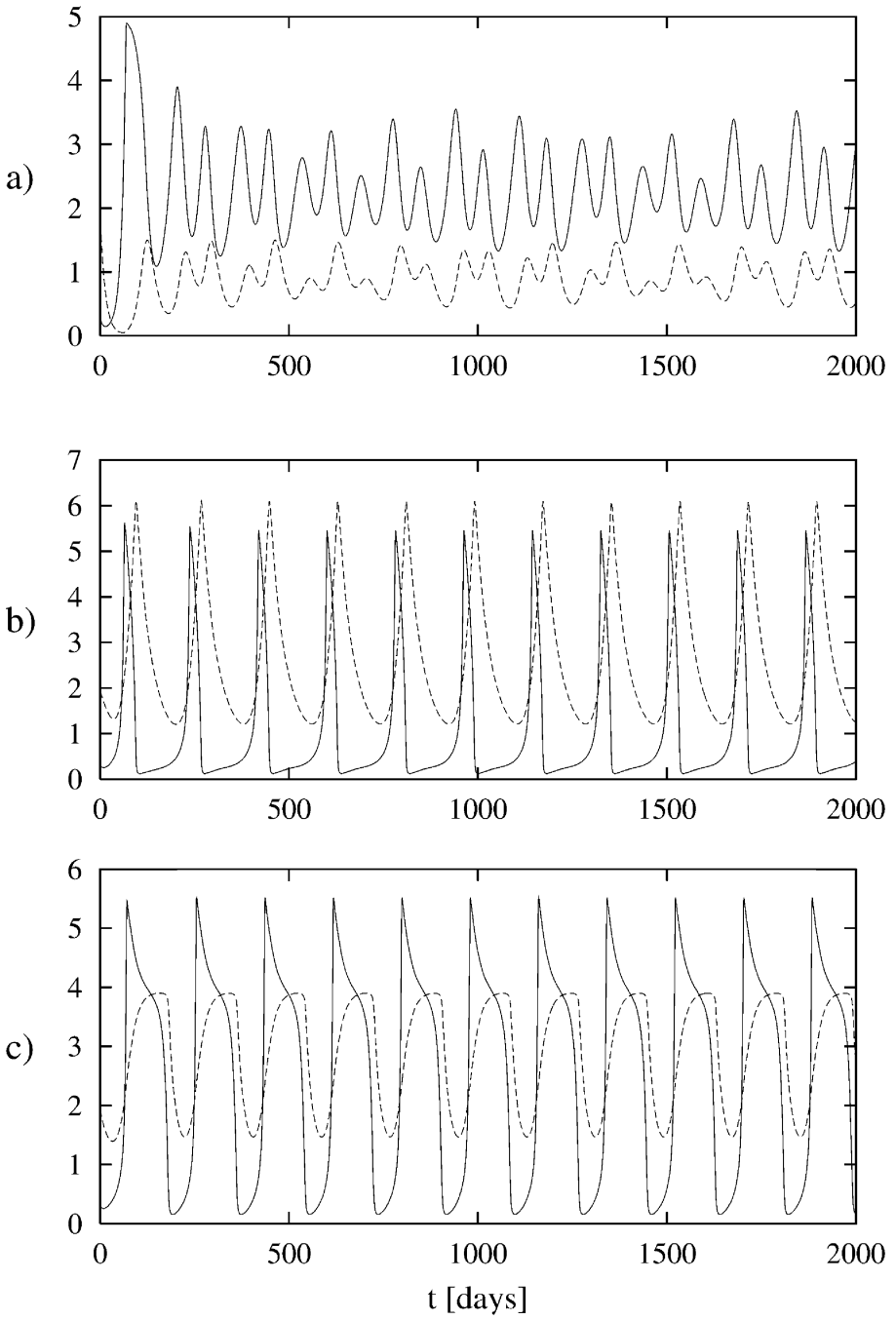

Fig. 4.7. Response of the phytoplankton (solid curves) and zooplankton (dashed curves) to depth variations $z = 30$ m + 3.5 m $\times$ cos($2\pi t/181$ days). The light decreases exponentially with depth. (*a*) Standard NPZ dynamics (see $z = 30$ m in Fig. 4.4); (*b*) excitable media (equation 5a); (*c*) multiple equilibria (equation 5b).

4. Review of Eddy Dynamics

We begin with a quick review of the dynamics of mesoscale eddies and jets with the goal of understanding the velocity structures and transports in such features. Much of the work in ocean modeling uses the *primitive equations*, which approximate the original Navier–Stokes system by assuming that (1) the vertical force balance is hydrostatic and the fluid occupies a shell that is thin compared to Earth's radius, (2) the vertical component of the Coriolis force is neglected, and (3) the gravitational force (which includes the centrifugal terms associated with Earth's rotation and also defines the vertical direction $\hat{\mathbf{z}}$) is regarded as having constant magnitude. In observations, the pressure serves as a measure of depth, and it is convenient to follow this in the theoretical development as well. We define the vertical coordinate z to be $-p/\rho_0 g$, where ρ_0 is a reference density. The vertical velocity w is defined as the rate of change of this quantity following the fluid parcel. The isopycnal-following RAFOS floats provide direct measurements of this quantity (see Bower, 1991). We shall use the notation $\mathbf{u}$ for the horizontal velocities. With these definitions, the conservation of mass equation

$$\nabla \cdot \mathbf{u} + \frac{\partial}{\partial z} w = 0 \tag{10}$$

simply states that horizontal convergence must be balanced by vertical stretching of the distance between isobars. This follows from the fact that there is a constant mass per unit area contained between two isobars for a hydrostatic fluid.

Newton's equations relating forces to accelerations become

$$\frac{\partial}{\partial t} \mathbf{u} = -2\boldsymbol{\Omega}_{\text{eff}} \times (\mathbf{u} + w\hat{\mathbf{z}}) - \nabla(\phi + \tfrac{1}{2}\mathbf{u} \cdot \mathbf{u}) + b\hat{\mathbf{z}} \tag{11}$$

(neglecting viscosity and diffusion). The terms on the right-hand side (in reverse order) represent

1. Buoyancy forces with light fluid tending to rise and heavy fluid to sink. The buoyancy (actually, the potential buoyancy) is given by $b = g(\rho_0 - \rho)/\rho - g^2/\bar{c}_s^2$, where the second term gives the compressibility effects, $\bar{c}_s^2$ being the average sound speed.
2. Pressure forces, including the Bernoulli effect. These are written in terms of the geopotential anomaly ϕ rather than the pressure—essentially, the component of the gravitational force along the pressure surface acts to accelerate the fluid horizontally. (The geopotential is the sum of the gravitational and centrifugal potentials; thus, a particle on a surface of constant geopotential will feel only forces normal to the surface—the mass times the gravitational acceleration vector $\mathbf{g}$. For practical purposes, ϕ is equal to $|\mathbf{g}|$ times the height.)
3. Acceleration associated with a reference frame that is rotating (locally) at a rate

$$2\boldsymbol{\Omega}_{\text{eff}} \equiv f\hat{\mathbf{z}} + \nabla \times \mathbf{u} \tag{12}$$

where f is the Coriolis parameter 4π sin (latitude)/day and $\nabla \times \mathbf{u}$ is the curl of the velocity, known as the *vorticity*. The Coriolis parameter is twice the rotation rate of Earth (as felt by a pendulum, for example) at the given latitude, and as we shall see, the vorticity is twice the rotation rate of a fluid parcel relative to Earth.

Since vorticity plays a central role in eddy dynamics, let us consider what it means in some detail. Suppose we lay out in the fluid a small circle of dye with radius ϵ. The rotation rate of this ring (ignoring the planetary rotation, which can be added back in) would be

$$\Omega_{\text{eff}} = \frac{1}{\epsilon} \langle u_{\text{tangential}} \rangle = \frac{1}{2\pi\epsilon^2} \oint \mathbf{u} \cdot d\mathbf{s}$$

Stokes' theorem then gives

$$\Omega_{\text{eff}} = \frac{1}{2\pi\epsilon^2} \int\int (\nabla \times \mathbf{u}) \cdot \hat{\mathbf{n}}\, dA = \frac{1}{2\pi\epsilon^2}\, \pi\epsilon^2 (\nabla \times \mathbf{u}) \cdot \hat{\mathbf{n}} = \frac{1}{2} (\nabla \times \mathbf{u}) \cdot \hat{\mathbf{n}}$$

Since $\Omega_{\text{eff}} = \hat{\mathbf{n}} \cdot \mathbf{\Omega}_{\text{eff}}$, we can see that the vector vorticity is just twice the effective rotation vector. Because the rotation time of Earth is short compared to the movement and evolution of the eddies, we must include the effective rotation rate associated with the spin of the planet; for a basically horizontal circuit, this is 2π sin(latitude)/day, giving a vorticity $f\hat{\mathbf{z}}$.

The system of equations is closed by a thermodynamic equation (cf. Charney and Flierl, 1981); we shall ignore the distinction between temperature and salinity stratification to deal only with the buoyancy (which includes both). By using pressure coordinates, we have avoided the traditional Boussinesq approximation that the variations in specific volume are small compared to the reference value. But we shall make a similar simplification by assuming that buoyancy forces are weak compared to gravity and the sound speed is nearly uniform. The thermodynamic equation then becomes

$$\frac{\partial}{\partial t} b + \mathbf{u} \cdot \nabla b + w \frac{\partial}{\partial z} b = 0 \tag{13}$$

We shall use the set of equations 10 to 13—the primitive equations—hereafter. In general, because these equations have three time derivatives, three wavelike motions occur: two gravity waves (traveling in opposite directions) and one Rossby wave. Mesoscale dynamics is concerned with the latter, which is the low-frequency mode.

4.1. Geostrophic Flow

In the vertical, the gravitational and pressure forces are nearly in balance. In the horizontal, we find a similar nearly balanced situation for mesoscale and larger-scale flows: the Coriolis forces and the pressure forces (gradients in geopotential in the equations above) balance to within order 20%:

$$f\hat{\mathbf{z}}\times\mathbf{u}\simeq-\nabla\phi\Rightarrow\mathbf{u}=\frac{1}{f}\,\hat{\mathbf{z}}\times\nabla\phi \tag{14}$$

To see why this might be true, we adopt the approach of scale analysis, although we shall not be formal about it. The basic idea is that we can estimate the sizes of terms if we specify the velocity scale U (the characteristic magnitude of $\mathbf{u}$ and a length scale L. By the latter, we really mean something like the maximum value of ϕ divided by the maximum value of $\nabla\phi$ (or similar quantities estimated from $\mathbf{u}$ or b). We then estimate the size of each term using $\nabla\sim 1/L$ and compare them. For a time scale, we use the advective time L/U. For the horizontal momentum equations, we have

$$\frac{\partial}{\partial t}\,\mathbf{u}+(\nabla\times\mathbf{u}+f\hat{\mathbf{z}})\times(\mathbf{u}+w\hat{\mathbf{z}})=-\nabla\left(\phi+\frac{1}{2}\,\mathbf{u}\cdot\mathbf{u}\right)$$

$$UU/L \quad (U/L,\ f)\times(U,W) \quad \boldsymbol{\Phi}/L \quad U^2/L$$

$$U/fL \quad (U/fL,1)\times(1,W/U) \quad \boldsymbol{\Phi}/fUL \quad U/fL$$

The second line shows the scales of each term, and the third line shows the ratio to the Coriolis term. Mesoscale motions are characterized by a small value of the *Rossby number* $\mathrm{Ro}=U/fL$; for example, a typical midocean eddy might have $U\sim$ 0.2 m s^{-1} and $L\sim 50$ km with $f\sim 10^{-4}$ s^{-1}, giving $\mathrm{Ro}=0.04$. Even a strong current such as the Gulf Stream with $U\sim 1$ m s^{-1} has Ro only 0.2. As we shall see, W/U is small; thus the Coriolis term dominates and we must choose a magnitude fUL for geopotential anomalies to balance Coriolis accelerations.

The geostrophic equation 14 with the hydrostatic equation

$$\frac{\partial}{\partial z}\,\phi=b \tag{15}$$

allow diagnosis of the horizontal velocities and density from the geopotential field; however, hydrographic data really give us only b and, via the *thermal wind* equation (derived by eliminating ϕ from equations 14 and 15), the vertical shear:

$$\frac{\partial}{\partial z}\,\mathbf{u}=\frac{1}{f}\,\hat{\mathbf{z}}\times\nabla b$$

The geostrophic/hydrostatic equations do not provide any estimate of the vertical velocity or any prediction for the changes in the flow. To find these we need to include higher-order corrections.

One other important implication of geostrophic balance is that the divergence of the horizontal velocities is small compared to the vorticity:

$$\nabla\cdot\mathbf{u}\simeq\nabla\cdot\frac{1}{f}\,\hat{\mathbf{z}}\times\nabla\phi=-\frac{1}{f^2}\,\nabla f\cdot\hat{\mathbf{z}}\times\nabla\phi\simeq-\frac{1}{f}\,\mathbf{u}\cdot\nabla f\sim\frac{\beta U}{f}$$

so that $|\nabla\cdot\mathbf{u}|/|\hat{\mathbf{z}}\cdot(\nabla\times\mathbf{u})|$ is order $\beta_*=|\nabla f|L/f\equiv\beta L/f$, where β measures the gradient of f—the Coriolis parameter increases northward because of the sin(*latitude*)

factor. The nondimensional parameter $\beta_* = \beta L/f$ for the 50-km length scale and $\beta \sim 2 \times 10^{-11}$ m^{-1} s^{-1} is about 10^{-2} which is O(Ro). The vertical velocity scale is $W = (\beta L/f)\ U\ (H/L)$ where H is the depth scale; this is weaker than one would expect from inspecting the mass conservation equation 10. Thus, vertical advection $[O(W/H)]$ will generally be quite small compared to horizontal advection $[O(U/L)]$ unless the property changes rapidly over a vertical scale that is small (order Ro) compared to the fluid depth, as biological properties may well do.

4.2. *Potential Vorticity*

The component of effective rotation normal to buoyancy surfaces $q = 2\mathbf{\Omega}_{\text{eff}} \cdot \nabla b$, known as Ertel's potential vorticity (PV), is the most significant dynamical variable for mesoscale flows for several reasons: It is a scalar conserved property (cf. Pedlosky, 1979), and if the flow is roughly in geostrophic balance, knowledge of the PV (and boundary conditions) is enough to determine the velocities.

We can understand the conservation of PV fairly easily if we return to the concept of a ring of dyed fluid. The net force arising from the $\nabla[\phi + \frac{1}{2}|\mathbf{u}|^2]$ terms is given by the difference of the quantity in brackets from the beginning to the end; for a closed circuit, this is zero. The buoyancy forces could cause torques (if, e.g., we tilt the ring up toward the north and have light fluid on the east side and heavy fluid on the west), but we can eliminate these by embedding the ring in a constant b surface. Then the integrated tangential velocity (the *circulation*) will not change with time. What happens if the distance between buoyancy surfaces expands? The area and circumference must shrink (of course, the circle will also generally distort, but that is not a problem). To preserve the circulation, the tangential velocity must grow as the circumference shrinks, implying that the vorticity grows. This is analogous to the ice-skater effect: Spin increases as the moment of inertia decreases. Since the circulation $2\mathbf{\Omega}_{\text{eff}} \cdot \hat{\mathbf{n}} A = 2\mathbf{\Omega}_{\text{eff}} \cdot \nabla b/|\nabla b|$ and the mass between neighboring buoyancy surfaces $A/|\nabla b|$ are both conserved, we can indeed see that the potential vorticity q does not change with time, following the fluid.

McWilliams (1976) has computed maps of potential vorticity (in the approximate quasigeostrophic (QG) sense described below) from the Mid-Ocean Dynamics Experiment. The eddies appear as blobs of high PV, with cyclonic (counterclockwise in the northern hemisphere) flow, and low PV with anticyclonic (clockwise) flow. A section of Ertel's PV, from cold- and warm-core rings [Olson (1980) and Flierl (1987), respectively] shows similar high- or low-PV centers. With the identification of high/low PV with cyclonic/anticyclonic flow, we can begin to view the ocean eddy field as sets of vortices that interact with each other and with the gradient in PV associated with the latitudinal variations of f.

4.3. *Quasigeostrophic Equations*

The QG equations state that an approximate form of the potential vorticity

$$Q = \nabla^2 \psi + f + \frac{\partial}{\partial z} \frac{f^2}{N^2} \frac{\partial}{\partial z} \psi \tag{16}$$

is conserved following the geostrophic flow

$$\frac{\partial}{\partial t} Q + \mathbf{u} \cdot \nabla Q = 0, \qquad \mathbf{u} = \hat{\mathbf{z}} \times \nabla \psi \tag{17}$$

Here $\psi = \phi/f$ is the *stream function* for the flow, meaning that $\psi(\mathbf{x}_2, z) - \psi(\mathbf{x}_1, z)$ measures the volume transport per unit depth between the two points $\mathbf{x}_2$ and $\mathbf{x}_1$. The Brunt–Väisälä frequency (squared) N^2 is defined as the mean value of $\partial b/\partial z$. The assumptions required for the QG equations to be a good approximation are that the β-effect is weak and the Rossby number is small, $\beta L/f \sim U/fL \ll 1$ and that the vertical and horizontal scales of the motion are related: $NH/fL \sim 1$. Like Ertel's potential vorticity, the QG PV has contributions from planetary rotation, local spin of the parcels (the relative vorticity $\zeta = \hat{\mathbf{z}} \cdot (\nabla \times \mathbf{u}) = \nabla^2 \psi$) and the thickness between buoyancy surfaces $[(\partial/\partial z)\ (f^2/N^2)\ (\partial/\partial z)\ \psi]$.

The QG equations have several advantages: the system is first order in time (whereas the full dynamics is third order) and the relationship between the PV, Q, and the flow, ψ, is linear so that the total flow is the superposition of the velocities associated with each vortex. Thus, intuition about how a vortex will be moved by its neighbors, intuition that is only approximate in the full system of equations, corresponds exactly to the mathematics in the QG system. (Of course, our intuition may not be terribly reliable when dealing with a system with many vortices—indeed, only four are required to produce chaotic motion; Aref, 1983.) Concomitantly, the QG equations are missing features of the original primitive equations system: asymmetries between cyclones and anticyclones (see below), interactions with steep topography and with gravity waves, rapid frontogenesis, and so on.

The QG equations can be split into two time evolution equations, one for the vertical component of the relative vorticity,

$$\hat{\mathbf{z}} \cdot (\nabla \times \mathbf{u}) = \frac{\partial}{\partial x} v - \frac{\partial}{\partial y} u = \nabla^2 \psi$$

and one for the buoyancy anomalies. This form shows the role of the vertical velocity explicitly:

$$\frac{\partial}{\partial t} \nabla^2 \psi + J(\psi, \nabla^2 \psi + f) = f \frac{\partial w}{\partial z}$$

$$\frac{\partial}{\partial t} \frac{\partial \psi}{\partial z} + J\left(\psi, \frac{\partial \psi}{\partial z}\right) + w \frac{N^2}{f} = 0 \tag{18}$$

where J is the Jacobian derivative, $J(A, B) \equiv \hat{\mathbf{z}} \cdot (\nabla A \times \nabla B)$, an antisymmetric, bilinear form. These reduce to equations 16 and 17 when we eliminate the vertical velocity. The content here is pretty much the same as discussed before: vertical stretching of a water column ($\partial w/\partial z > 0$) causes closed contours to shrink and the vorticity to increase; alternatively the parcel of fluid can change its planetary vorticity. The vertical motions also uplift or depress the isopycnals (and, of course, the biota). We can use either of these equations to estimate w.

4.4. *Level and Layer Models*

Numerical studies of the dynamics require some form of discretization; often a fairly fine vertical grid is used in the near-surface layers for accuracy. However, even the coarsest resolution, a two-level or two-layer model, can offer significant insights into the important physical processes at work. In this case, the vertical velocity (which is constrained to be zero on the top and the bottom) has only one degree of freedom in the vertical: its value at the middle (usually thermocline) depth. In the *level model* we solve for w at a fixed depth and discretize the horizontal velocities above and beneath the thermocline. For the *layer model*, we assume that the pycnocline [at $z = -h(x, y, t)$ is a material surface separating light, constant buoyancy fluid from heavier fluid. The vertical velocity is calculated at this moving interface:

$$w = -\frac{D}{Dt}\, h, \qquad \frac{\partial w}{\partial z} = \frac{1}{h}\, \frac{D}{Dt}\, h \tag{19}$$

(in the upper layer) as sketched in Fig. 4.8. The horizontal velocities are independent of depth within each layer, the vertical change in the horizontally varying pressures can be related to the jump in buoyancy, and the total depth is assumed to be fixed:

$$\frac{\partial}{\partial t}\, \mathbf{u}_i + (\zeta_i + f)\hat{\mathbf{z}} \times \mathbf{u}_i + \nabla \tfrac{1}{2}|\mathbf{u}_i|^2 = -\nabla \phi_i, \qquad \phi_1 = \phi_2 + g' h$$

$$\frac{\partial}{\partial t}\, h_i + \nabla \cdot (\mathbf{u}_i h_i) = 0, \qquad h_1 = h, \quad h_2 = H - h \tag{20}$$

with $g' = b_1 - b_2$. The potential vorticity in each layer,

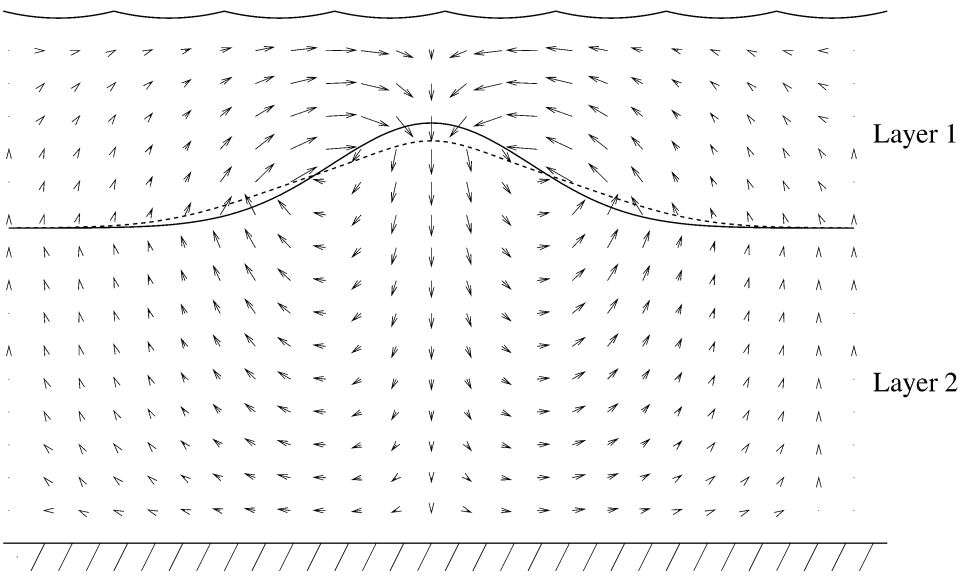

Fig. 4.8. Two-layer model, showing the vertical velocities and the divergent part of the horizontal velocities associated with deepening of the thermocline in the center of the feature.

$$q_i = \frac{f + \zeta_i}{h_i}$$

is conserved. This system of equations (or its quasigeostrophic analog) contains some representation of the effects of stratification and has proved to be an excellent tool for understanding the basic processes governing the eddy field.

4.5. Advection of Biological Properties

The primary effect of the fluid upon the biota is, of course, advection, which we can represent as the *material derivative*

$$\begin{aligned}\frac{D}{Dt}\, p_i &\equiv \frac{\partial}{\partial t}\, p_i + \mathbf{u} \cdot \nabla p_i + w\, \frac{\partial}{\partial z}\, p_i \\ &= \frac{\partial}{\partial t}\, p_i + \nabla \cdot (\mathbf{u} p_i) + \frac{\partial}{\partial z}\, (w p_i)\end{aligned}$$

Primitive equation models represent the advection fully, often using the flux form to ensure conservation of material. When we are using the quasigeostrophic approximation, the material derivative becomes

$$\frac{D}{Dt}\, p_i \simeq \frac{\partial}{\partial t}\, p_i + J(\psi, p_i)$$

if the vertical scale of p_i is similar to that of the flow. Often, however, the biological fields will vary rapidly in the vertical, so that $\partial/\partial z$ of these quantities can easily be order Ro^{-1} compared to the vertical derivatives of physical properties (e.g., for a Rossby number of 0.05 and currents decaying over the top 1 km, we would require a biological scale order 50 m). In that case we must also keep the vertical advection term[3]

$$\frac{D}{Dt}\, p_i \simeq \frac{\partial}{\partial t}\, p_i + J(\psi, p_i) + w\, \frac{\partial}{\partial z}\, p_i$$

5. Rossby Waves and Biological Dynamics

To illustrate some of the basic aspects of mesoscale physical–biological coupling, we begin with freely propagating Rossby waves, which are analytical solutions to the QG equations 16 and 17. Although such motions do not exhibit the strong nonlinearity characteristic of oceanic mesoscale and submesoscale phenomena, they constitute a framework for examining some simple processes. In this first example we consider the role of horizontal advection in a channel of length L with stress-free walls at

[3] A somewhat tricky question is whether the last term should be written in flux form, given the fact that the horizontal advection by the geostrophic flow can be so expressed. However, using flux form for the vertical advection keeps some terms which are small while neglecting others of the same order, and that appears to be problematical.

$y = 0$ and $y = W$. The depth-independent (*barotropic*) Rossby wave solution to the QG equations has a stream function

$$\psi = \frac{U_0}{l} \sin[k(x - ct) + \theta] \sin ly \tag{21}$$

and a PV field

$$Q = f - \frac{U_0}{l(k^2 + l^2)} \sin[k(x - ct) + \theta] \sin ly$$

Substituting these into equations 16 and 17 gives the propagation speed or the frequency of a wave:

$$c = -\frac{\beta}{k^2 + l^2}, \qquad \omega = -\frac{\beta k}{k^2 + l^2} \tag{22}$$

The characteristic frequencies are small—order $\beta L/f$—compared to the lowest inertial-gravity frequencies (which run from f to N) and get smaller as the wave scale decreases. We can understand fairly easily the physics behind the restoring forces that make the system oscillate. Suppose that the contours of Q are shifted north and south around the latitude circle (Fig. 4.9*a*); the relative vorticity on the northward-shifted parts of the contours is negative (since f is higher and $\nabla^2\psi + f$ is constant on the contour), while the southward-shifted particles have positive relative vorticity. The flow will be clockwise (positive ψ) around the negative-vorticity regions and counterclockwise (negative ψ) around the positive-vorticity regions—characteristically, when we solve the Poisson equation 17, we find that ψ has the opposite sign from Q, is scaled by L^2, and is smoother. Thus the flow will tend to shift the Q contours (which move like dye lines in the fluid) northward on the eastern side of the peaks and southward on the western side, and the original pattern shifts westward with time.

As an example of the effects of the horizontal advection, consider the eddy transport version of Wroblewski's (1980) analysis of the offshore distribution of copepod life stages. We will use the more complex life-stage model of Davis (1984) (equation 6) and suppose that there is a source of eggs at $t = 0$ in a nearshore strip. The distribution of the various classes at later times is governed by

$$\frac{\partial}{\partial t} n_i + J(\psi, n_i) = L_{ij} n_j + \nabla\kappa \ \nabla n_i + s(\mathbf{x})\delta_{i1}\nu(t)$$

with n_1 representing the concentration of new eggs, $\nu(t)$ being the temporal variation of spawning, and $s(\mathbf{x})$ giving the spatial distribution. This linear problem can be solved in terms of the Green's function for the physics—the distribution that a passive tracer would have at time t if injected at time t' with concentration $s(\mathbf{x})$—and the biological evolution, which is exponential. The copepod distribution is given by

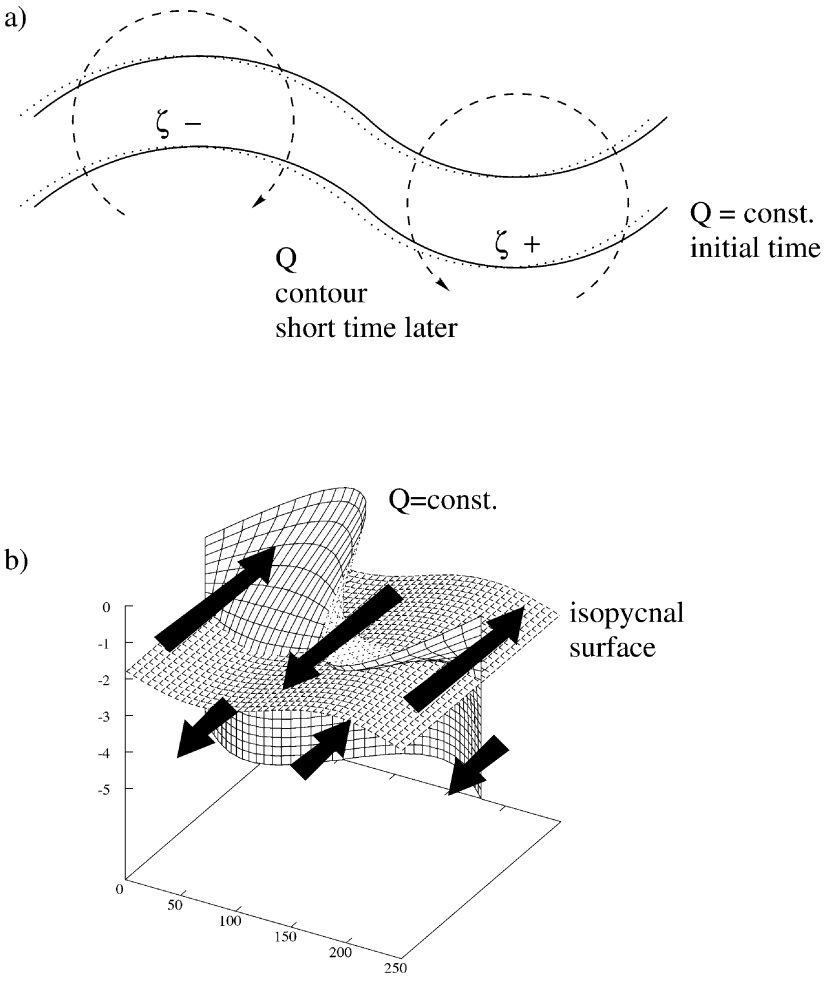

Fig. 4.9. Rossby wave dynamics: (*a*) barotropic, showing the contours of constant $Q = \zeta + \beta y$ at the initial time, the sign of the relative vorticity ζ, and the position of the Q contours at a slightly later time after the advection by the induced flows; (*b*) baroclinic, showing the Q contour in x and z and the depth of the thermocline, deeper in low-surface Q regions (weak stratification), which occur where the Q contour is displaced northward. The arrows show the flow above and below the thermocline.

$$n_i(\mathbf{x}, t) = \int_0^t dt' \; e^{L_{ij}(t-t')} \delta_{j1} \nu(t') g(\mathbf{x}, t, t')$$

where the Green's function satisfies

$$\frac{\partial}{\partial t} \; g(\mathbf{x}, t, t') + J(\psi(\mathbf{x}, t), g(\mathbf{x}, t, t')) = \nabla \kappa \; \nabla g(\mathbf{x}, t, t')$$

$$g(\mathbf{x}, t', t') = s(\mathbf{x})$$

Note that the exponential in the integral above is a matrix exponential, not the exponential of each element in the matrix (see Varga, 1962). In principle, this can be found by writing the normal Taylor series for the exponential function, replacing L^n by the product of n identical matrices, and summing the series.

For the smoothly propagating wave in a channel with the source function depending only on the distance y from the shore, the flow is steady in a translating reference frame $\xi = x - ct$. In that frame, the Green's function depends only upon the elapsed time, not the start time, $g = g(\xi, y, t - t')$, and the copepod distribution is found from

$$n_i(\xi, y, t) = \int_0^t d\tau \; e^{L_{ij}\tau} \delta_{j1} \nu(t - \tau) g(\xi, y, \tau) \tag{23}$$

In Fig. 4.10 we show the distributions when the source of eggs is just a pulse $\nu(t) = \delta(t - t_0)$ in a narrow Gaussian strip along one wall so that

$$n_i(\xi, y, t) = e^{L_{ij}(t - t_0)} \delta_{j1} g(\xi, y, t - t_0)$$

The Green's function has essentially the same shape; its amplitude decreases by 44% over the 70-day period. Clearly, the waves gather material out of the edge strip and carry it across the wave pattern quite effectively. Even with fairly weak waves (10 km day^{-1} currents), the nauplii and copepodid stages can be found well offshore, while many of the adults have actually returned inshore.

When we maintain the egg source, so that ν is constant in time, we can solve for the long-term distribution (Fig. 4.11). Note that we can now take a time derivative of equation 23 to find

$$\frac{\partial}{\partial t} n_i(\xi, y, t) = e^{L_{ij}t} \delta_{j1} g(\xi, y, t)$$

so that we can simply time-step the variables forward at each grid point without having to advect the fields—that is taken care of by the local weighting factor g. This represents a substantial gain in efficiency. Separable problems of this sort are not uncommon when the biological dynamics is essentially linear. The cross-channel distributions are set by the time scale for eddy transport and the development times. For our example, the copepodids have a maximum offshore because that matches with the transport time; however, the spread in physical times makes the distributions quite broad.

Vertical Motion

Since the copepod model we are using does not have explicit light dependence, we will turn to the NPZ model, which does, to examine the importance of motion up and down in the light gradient. Equation 18 indicates that vertical velocities will be associated with flows whose horizontal velocities are not uniform with depth. In that case, the thermal wind equation implies that the local buoyancy will also vary with time and space. Let us now consider a depth-dependent (*baroclinic*) wave in the presence of a background zonal, vertically sheared flow. If the stream function has the form

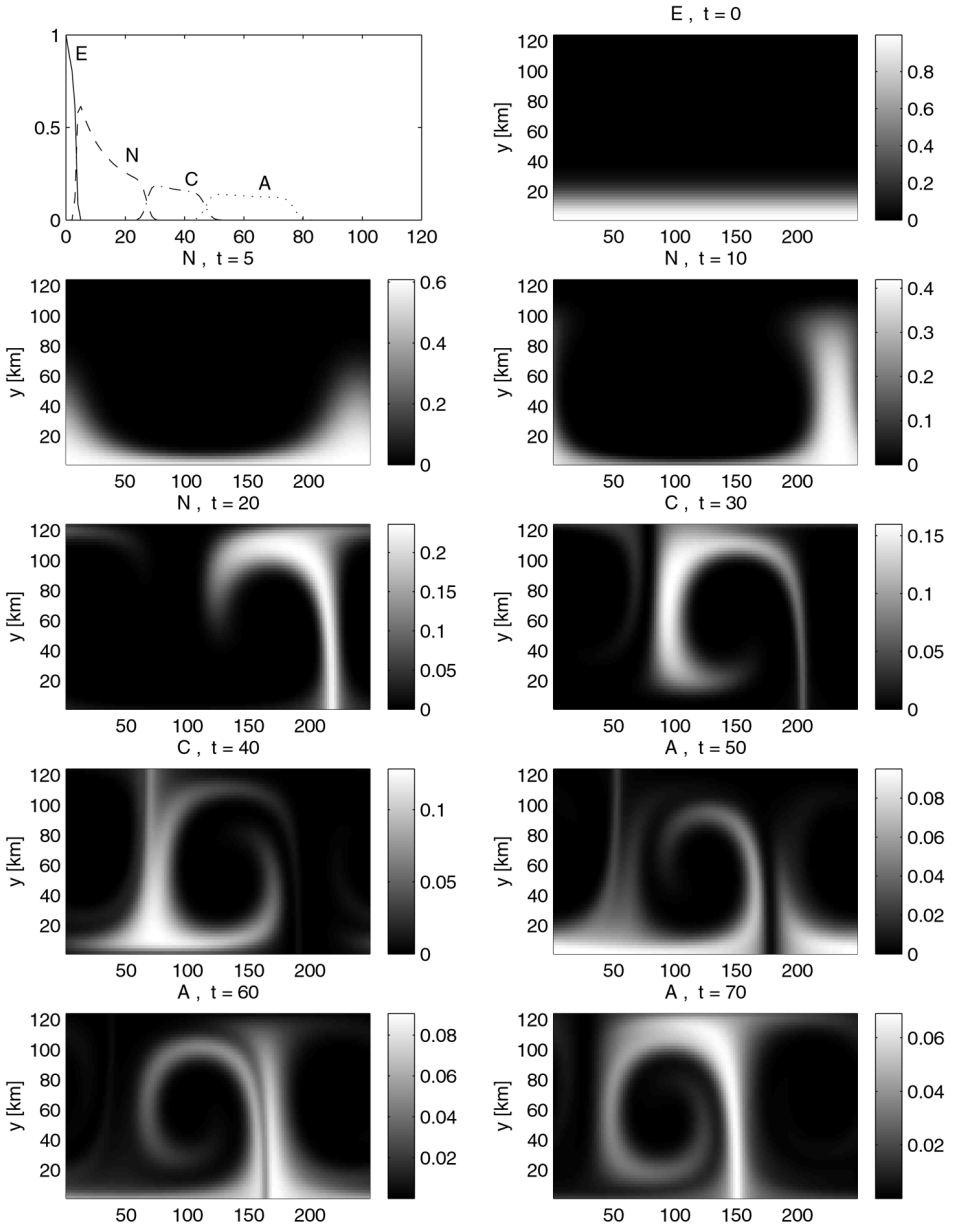

Fig. 4.10. The first panel shows the time development (in days) of the copepods summed over the variables representing concentrations in age-stage bins which fall into the categories of eggs (E), nauplii (N), copepodids (C), and adults (A). The other panels show the spatial distribution of the predominant class (indicated by the N, C or A in the plot title) at the labeled times. The distances are in kilometers with the wave having a 250-km wavelength. The densities are normalized to the maximum egg density at $t = 0$.

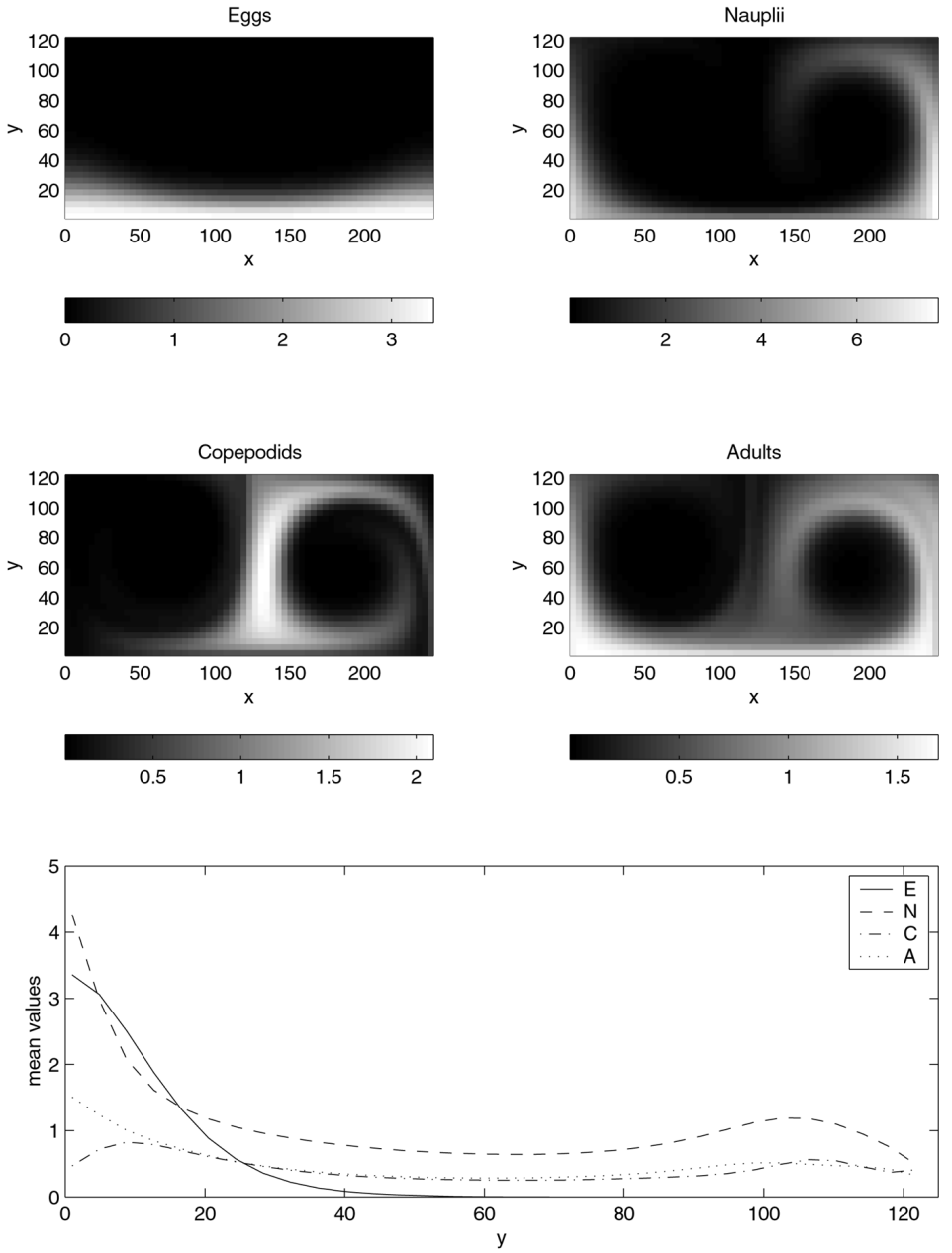

Fig. 4.11. Steady-state distribution (comoving frame) for a constant source of eggs. The nauplii, copepodids, and adults shown are from the first generation only—reproduction is not being modeled. Since we are keeping the egg source fixed in space and time, we can think of this as a case where the eggs are entering the water column from a source on the bottom (i.e., resting eggs). The bottom panel shows the channel-averaged values.

$$\psi = -U(z)y + \frac{V_0}{k} \sin[k(x - ct) + ly]F(z)$$

we find two simple relationships between the meridional flow $v = \frac{\partial}{\partial x} \psi$ and the vertical velocity:

$$[c(k^2 + l^2) - U(z)(k^2 + l^2) + \beta]v = f \frac{\partial}{\partial z} w$$

$$[c - U(z)] \frac{\partial}{\partial z} v + v \frac{\partial}{\partial z} U(z) = \frac{N^2}{f} w$$

There is no nonlinear advection of the wave by itself, since the vorticity and buoyancy fluctuations are proportional to ψ at each level, and therefore their gradients are perpendicular to $\mathbf{u} = \hat{\mathbf{z}} \times \nabla\psi$. These equations, with the boundary conditions $w = 0$ at $z = 0, -H$, specify the possible vertical structures and the phase speeds. In particular, if we have no background flow $[U(z) = 0]$, we find that

$$\frac{\partial^2}{\partial z^2} w - \left(k^2 + l^2 + \frac{\beta}{c}\right) \frac{N^2}{f^2} w = 0, \qquad w(0) = 0, \quad w(-H) = 0$$

which is a Sturm–Liouville problem having an infinite, nonnegative set of eigenvalues γ_n^2, each associated with a vertical structure function $w_n(z)$ (the eigenfunction) and a phase speed $c_m = -\beta/(k^2 + l^2 + \gamma_n^2)$. Figure 4.12 shows the vertical modal structures. Note the linearity of the vertical velocity through the upper 100 m.

The gravest (barotropic) mode has $w = 0$ and horizontal velocities that are independent of depth. It travels with speed $c = -\beta/(k^2 + l^2)$. For the baroclinic modes, the vertical velocity is not zero (implying that we will produce additional effects on the biology via movement through the light field as we have seen in Section 2). For short waves, the dynamics is essentially the same as that described above: trade-offs between changes in planetary and relative vorticity. For long waves, however, the relative vorticity is small, and the dominant contribution to the potential vorticity comes from $f(\partial/\partial z)\, b$ (Fig. 4.9*b*). Consider a region with northward motion in the upper part of the water column and southward motion at depth. In the upper water, f is increasing so the stratification must be decreasing, with the opposite being true in deep water. Thus the thermocline will be deepening in this area. However, the thermal wind equation tells us that the middepth water is denser to the east and less dense to the west of the region, implying that the thermocline is shallower on the east side of the region of positive v and deeper on the west. The temporal changes again cause the deep thermocline anomaly to shift westward.

Rossby waves, then, are characterized by restoring forces (or tendencies) induced by advection of the large-scale gradients in the potential vorticity. Linear waves characteristically propagate parallel to the PV contours, but are dispersive, since components with different scales will travel at different speeds. In addition, the nonlinear terms (which exist when multiple waves are present—or when the terms neglected in the OG approximation are not adequately small) will generally ensure that eddy propagation is not so regular. We examine these processes further in the next section.

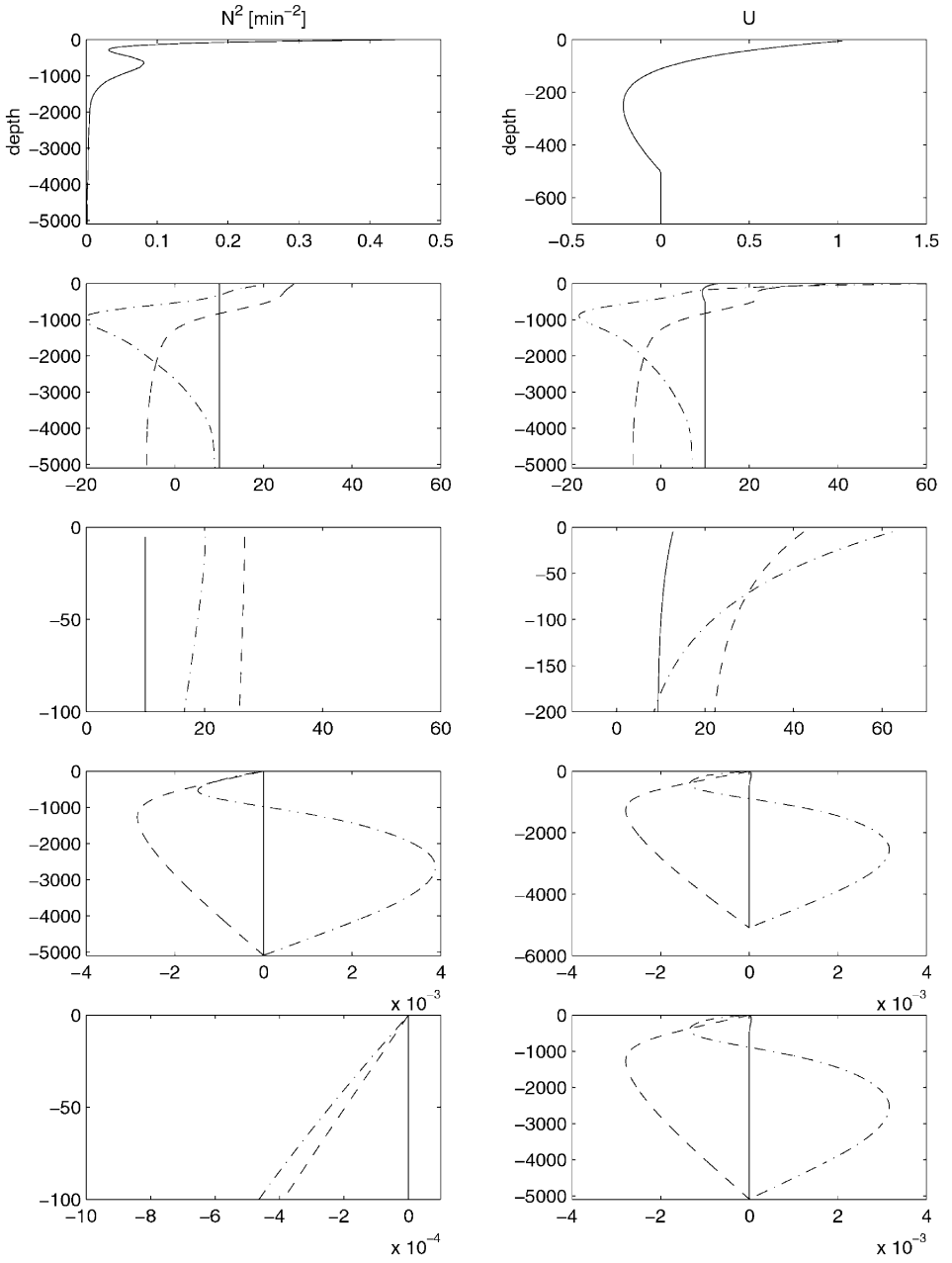

Fig. 4.12. Gravest three-modal structures for v [second and third rows (upper 100 m)] and w [fourth and fifth rows (upper 100 m)]. The modes have been normalized to have the rms v equal 10 km day^{-1}. The left figures are for $U(z) = 0$; the eigenvalues are $\gamma = 0$, $1/44.8$ km, $1/19.1$ km, and the phase speeds are $c = -3.50, -1.74, -0.53$ km day^{-1}. On the right are the cases with mean flow shown on the top row; the phase speeds are $c = -3.50, -1.74, -0.59$.

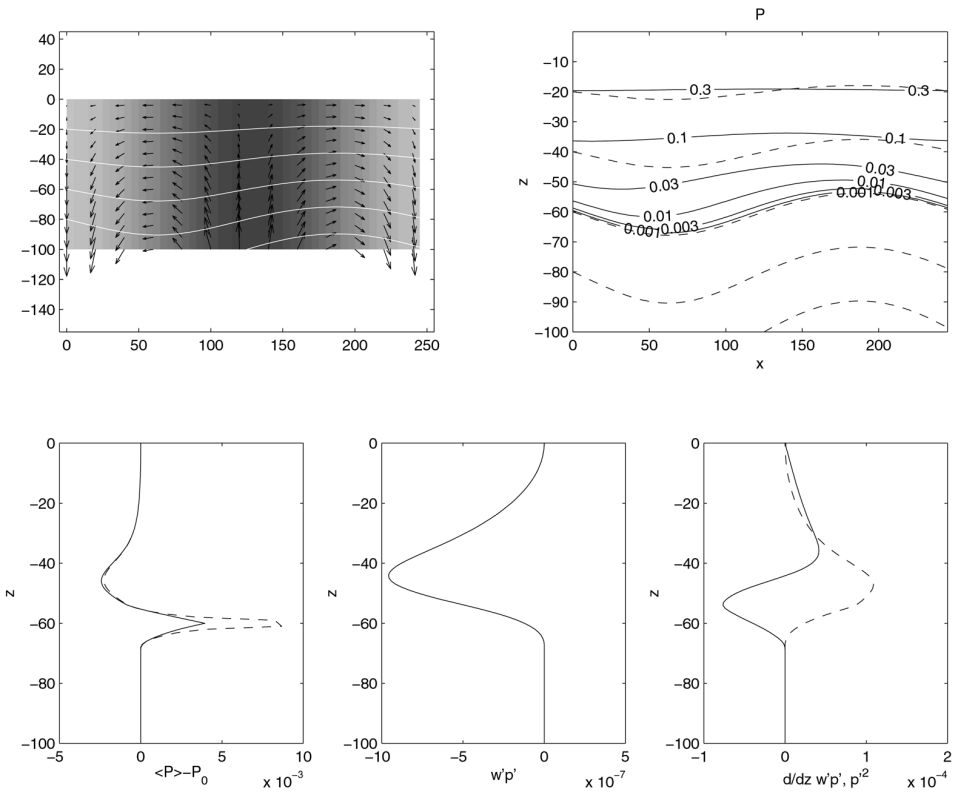

Fig. 4.13. Response of the logistic equation to a traveling Rossby wave. The left upper panel shows the zonal-vertical velocities, the density (contoured), and the meridional velocities (gray scale). Depths are in meters and zonal distances in kilometers. The right panel shows the distribution of P and trajectories/density contours (dashed). The lower plots show $\langle P\rangle - P_0$, $\overline{w'P'}$, and the two fluctuation terms $[(\partial/\partial z)\ \overline{w'P'}$ and $\overline{P'^2}$, dashed] which alter the mean. The dashed curve on the left shows the simplest prediction of the alteration in the mean, the forcing terms divided by $-|r_0 e^{z/h} - d_0|$.

The modal structures and phase speeds are altered somewhat in the presence of mean shear. For near-surface shear (see McWilliams, 1974), the surface velocities are increased (Fig. 4.12) and the westward phase speeds are decreased. The near-surface vertical velocities are not very different. Shears that extend deeper into the water column can excite baroclinic instabilities (Charney, 1947) as discussed below.

We now examine the effects of such a wave on the biology, taking the case without mean shear as an example. The wave is assumed to have a zonal wavelength of 181 km, a first baroclinic mode vertical structure (corresponding to the dashed lines in Fig. 4.12), and no meridional variation. The surface velocity is chosen to be 40 km day^{-1}, giving $(\partial/\partial z)\, w = cv\gamma_1^2/f$ of 0.004 day^{-1}, which is small compared to the fastest biological time scales. (Although this velocity is strong for a single wave, the stretching values are comparable to those seen in more complex eddy fields.) The wave can have two effects: first, if there is meridional variation of the biology, there will be rapid advection by the v velocities, causing substantial temporal changes at a point. This effect is akin to the copepod transport problem studied above. Second, even for a statistically homo-

geneous region, the vertical advection will move the biota through the light field, and the plankton will respond to the light variations. For the logistic equation 3, the resulting fields and the changes in the mean are quite similar to those shown in Fig. 4.1 if we allow for the different values of $(\partial/\partial z)\, w$. Figure 4.13 shows the flow field, the phytoplankton distribution, and the terms in the mean equation

$$\frac{\partial}{\partial z}\,\overline{w'P'} = \overline{\mathcal{P}(\overline{P}+P')}$$

$$= r_0 e^{z/h}\overline{P} - d_0\overline{P} - d_1\overline{P}^2 - d_1\overline{P'^2}$$

or

$$-\left|r_0 e^{z/h} - d_0\right|(\overline{P}-P_0) - d_1(\overline{P}-P_0)^2 = \frac{\partial}{\partial z}\,\overline{w'P'} + d_1\overline{P'^2}$$

The eddy flux is negative, reaching a minimum at about 45 m depth, so that the right-hand side is positive in the upper water and the mean P must be smaller than P_0. In the deep water, the flux divergence is negative and larger than $d_1\ (\overline{P}-P_0)^2$ (the changes in the nonlinear biological rates associated with the fluctuations), so that the mean is increased.

When we consider the more complex NPZ model, the response to the vertical velocities becomes more striking (Fig. 4.14). The upwelling excites a transient bloom near the base of the euphotic zone, in the depth ranges where the biological system is least stable. The phytoplankton at the base of the euphotic zone can vary by about a factor of 4 and are enhanced overall by 20%.

When we increase the velocities to 40 km day^{-1}, the response strengthens as well, so that the biomass of phytoplankton at the base of the euphotic zone varies by almost a factor of 4. We emphasize the strong effects of these still quite weak vertical velocities by showing time series of P at various depths in Fig. 4.15.

6. Isolated Vortices

Mesoscale and submesoscale motion in the ocean include not only the eddy field, which we tend to think of as having a broad spectrum of space and time scales—turbulence on a planetary scale—but also coherent, isolated vortices. The latter, called *rings*, are generally spawned by a strong boundary current forming a loop that cuts off (see Richardson, 1983) or by outflows. They can be remarkably persistent. In the case of the Gulf Stream cold-core rings (which were the sites of some of the earliest interdisciplinary study; Ring Group, 1981), lifetimes of several years and trajectories covering thousands of kilometers through the Sargasso Sea have been documented; indeed, the biological signature—the presence of slope water organisms—can serve as verification that significant volumes of water have come along with the vortex. Warm-core rings, formed to the north of the Gulf Stream, tend to have shorter lifetimes (order 8 months) since they are more tightly confined between the shelf and the stream, but can still play a significant role in cross-stream mixing of the biota (Olson, personal communication). Similar vortices are formed in

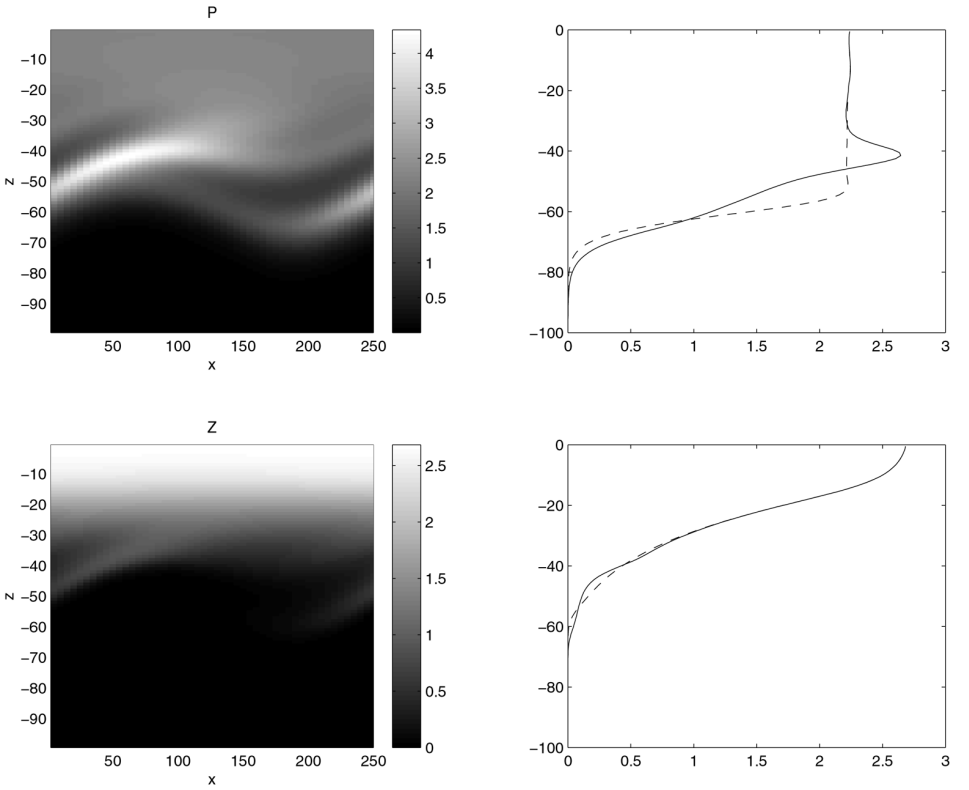

Fig. 4.14. See color insert. Response of the NPZ system to a traveling Rossby wave. The zooplankton respond only weakly, but the phytoplankton show a bloom during the upwelling phase. The left panels show the x–z structure of P and Z; the right panels show the zonal means (solid curves) in comparison to the equilibrium solutions (dashed curves).

the Kuroshio, Agulhas, Brazil, and East Australian currents, although the details of the formation process differ from place to place.

Rings affect oceanic biology in a number of ways. Transport over large distances has already been mentioned; however, the vortices are also clearly not closed systems; some species are lost and replaced by others, which are entrained from the outside or enter from below. Some species appear to be opportunists that thrive in the anomalous environment (Ring Group, 1981). The movement of vortices, which is associated with the background PV gradient as in the case of Rossby waves, also causes upwelling and downwelling with the possibility of altering the biological balances. Finally, rings can draw water off the continental shelf and force slope water onto the shelf; the off-shelf transport may have significant influence on larval fish distributions (Flierl and Wroblewski, 1985; Lobel and Robinson, 1986; Sinclair, 1988; Werner et al., 1996).

Meddies are another form of isolated vortex structure, generally found at middepth and based on their temperature and salinity characteristics, formed by detachment of a bolus of warm salty fluid from the Mediterranean outflow. Almost certainly, generation of such features will occur in other overflows, but the resulting eddies may not have such strong property anomalies and therefore may be less easy to detect.

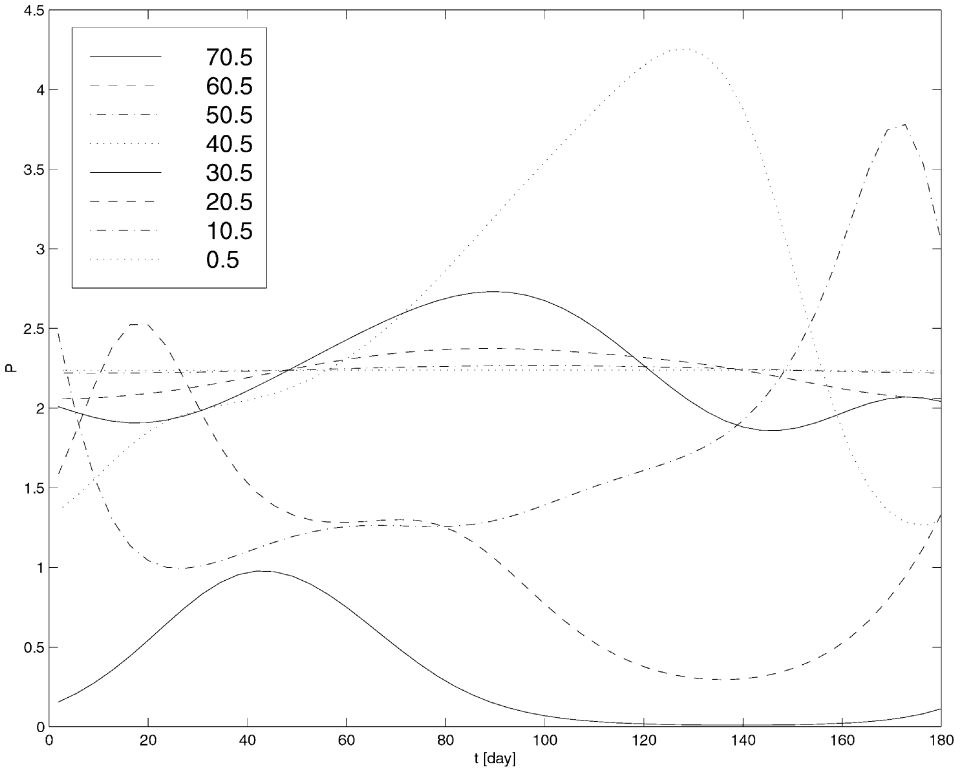

Fig. 4.15. Time series of P at the depths labeled (in meters). The shallow depths correspond to the nearly straight lines at about 2.2, while the deepest series corresponds to the series with values that are less than 1.

Again, lifetimes of over two years have been documented by float trajectories, and persistence for longer is quite likely (Hebert et al., 1990).

Let us now consider models of such features and their biological impacts in more detail.

6.1. Structure

As examples of the structure, we consider a two-layer model (equations 20) with anomalous PV within a circle of radius a in one or both of the layers. The PV equations become

$$q_i \equiv \frac{f + \dfrac{1}{r}\dfrac{\partial}{\partial r} r v_i}{h_i} = \frac{f}{H_i} \begin{cases} 1 + \Delta_i, & r < a \\ 1, & r > a \end{cases}$$

We combine these with the thermal wind equation, including the centrifugal terms

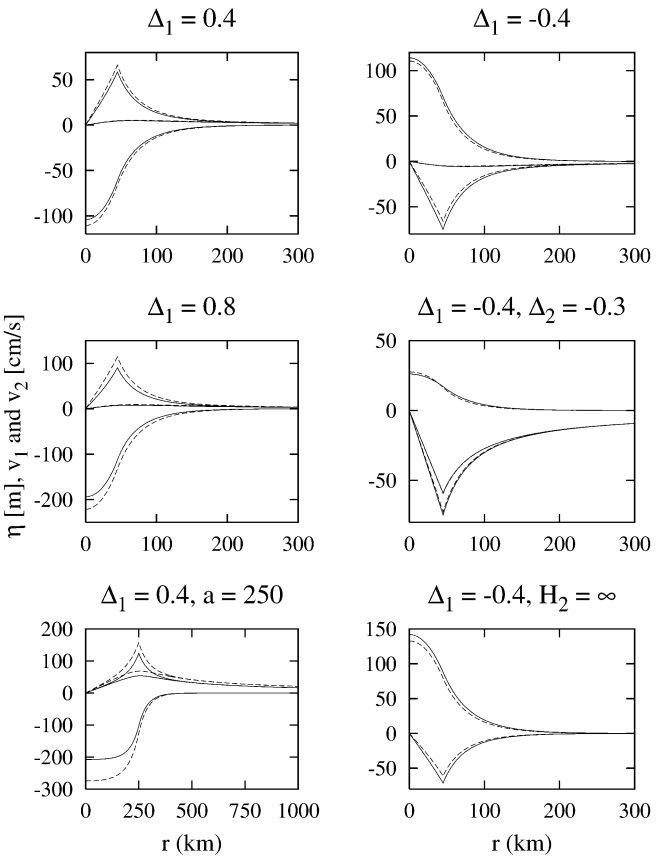

Fig. 4.16. Structure of isolated vortices for various sizes (a, in kilometers) and PV anomalies (Δ_1, Δ_2). The solid curves that go to zero at the center are the surface and (weaker) deep velocities in cm s^{-1}; the third line is the thermocline elevation in meters. The dashed curves show the QG approximation. If not otherwise noted in the title, $\Delta_2 = 0$, $a = 45$ km, $H_1 = \frac{1}{5} H_2$, $H_1 + H_2 = 5000$ m.

$$f(v_1 - v_2) + \frac{v_1^2 - v_2^2}{r} = g' \frac{\partial}{\partial r} h_1$$

We can integrate these three equations numerically; Fig. 4.16 shows some examples of eddies with various sizes, strengths, and vertical structures of the PV anomalies. These examples imply:

1. Positive (negative) anomalies in one layer induce cyclonic (anticyclonic) circulation in both layers, with the circulation being weaker in the layer without anomalies.
2. Small eddies have proportionally larger velocity differences (are more baroclinic), while large anomalies have barotropic flows except right at the edge. In essence, the inversion operator for calculating ψ from Q smooths the field (and inverts the sign), with the changes occurring over the *Rossby radius*

$$R_d = \left[\frac{g' H_1 H_2}{f^2 (H_1 + H_2)} \right]^{1/2}$$

Vertically, the signal is also smeared over a depth on the order of $(f/N)\,a$ in the stratified case. When the eddy is large compared to the Rossby radius, the vertical smearing implies that the PV anomaly acts as though it filled the full water column.

3. For circulations with the same speed, cyclones have a deeper low-pressure anomaly and a larger displacement of the thermocline than anticyclones—the pressure gradient has to balance both Coriolis and centrifugal forces. The difference increases as the Rossby number increases.
4. For typical oceanic eddy strengths, the difference between the quasi-geostrophic model, which ignores the centrifugal terms and the product $\Delta(h_i - H_i)$, and the full equations is small.
5. The upper layer structure is not greatly altered by assuming that the lower layer is infinitely deep and at rest.

6.2. *Movement*

Like Rossby waves, vortices will move when they are embedded in a large-scale PV gradient. A cyclonic ring in the northern hemisphere, for example, advects fluid with higher background potential vorticity from the north (where f is larger) down on its western side and lower PV fluid up on the east. These changes with time correspond to a westward shifting of the positive PV center of the vortex. Alternatively, we note that the centers of the stream function, relative vorticity, and the upper layer thickness coincide for a circular feature, but that the potential vorticity center will be offset to the north (south) for a cyclone (anticyclone) by the northward increase in PV associated with the β term. Thus, this center point will be advected westward. However, the details are more complex than for the plane wave case: If we calculate $(\partial/\partial t)\,q$, we find it is not exactly proportional to $(\partial/\partial x)\,q$ so that the vortex distorts in shape and the nonlinear terms begin to play a significant role (McWilliams and Flierl, 1979). Figure 4.17 shows the evolution of the various fields in a QG model, with the initial condition being a circular cyclonic PV anomaly as above. The eddy moves westward, but also northward; essentially, the dipole generated by the advection of the background PV gradient becomes strong enough to move as a vortex pair.

6.3. *Trapped Fluid*

Fluid is carried along with the eddy when the swirl velocity exceeds the translational speed; in a steadily propagating roughly circular eddy, there will be two critical points where the vector flow velocity matches the translational velocity, one near the center and one on the outer side. If we draw the trajectory of a parcel just inside the outer critical point, it will make a loop and return to the same position relative to the eddy center. Thus all the fluid within this trajectory will move along with the eddy (Flierl, 1981). Clearly, this is happening in Fig. 4.17, since the PV follows material particles. In the ocean, Lagrangian floats have stayed trapped within individual eddies for periods exceeding one year (Richardson, 1993), indicating the nonlinear nature of the propagation.

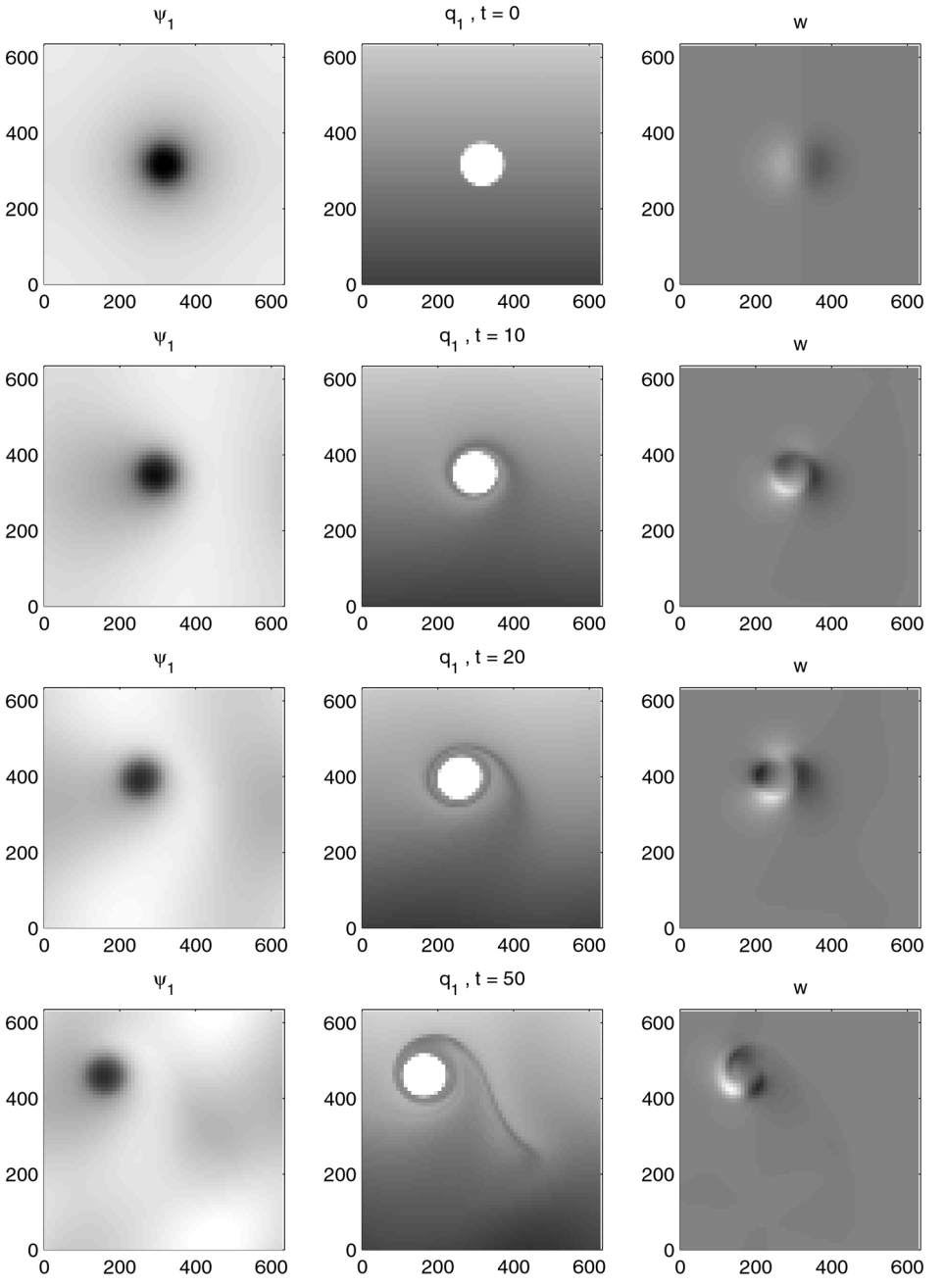

Fig. 4.17. Evolution of the PV, ψ, and $w(-h)/h$ fields for a cyclonic vortex. Gray scale ranges (black to white) correspond to (-3200, 700 km^2 day^{-1}), (-0.5, 4.5 day^{-1}) and (-0.01, 0.01 day^{-1}), respectively.

6.4. *Upwelling Flow Field*

Propagating eddies transport nutrient into the euphotic zone by both kinematic and dynamic effects. We can see how each of these works by looking at the terms in equation 19 and noting that in the nearly geostrophic regime, the thermal wind gives

$$f\hat{\mathbf{z}} \times (\mathbf{u}_1 - \mathbf{u}_2) = -g' \nabla h$$

so that

$$\frac{\partial}{\partial z} w \simeq \frac{1}{H_1} \frac{\partial}{\partial t} h + \frac{f}{g' H_1} \hat{\mathbf{z}} \cdot (\mathbf{u}_2 \times \mathbf{u}_1)$$

The kinematic effects arise from the first term and are sketched in Fig. 4.18: Consider a fluid parcel that lies just below the euphotic zone at the edge of a cyclonic eddy (point a) at time t_1. As the eddy moves to its new position at time t_2, the fluid parcel will be displaced. If the propagation of the eddy is purely linear, the parcel at point a will be lifted vertically into the euphotic zone to point c. On the other hand, if the propagation speed were negligible compared to the fluid velocity, the parcel would move almost horizontally to point b. Nonlinearity does not strongly alter the propagation speed of an isolated vortex, so we would expect the vertical stretching

$$\frac{\partial w}{\partial z} \simeq -c \frac{\partial \ln h}{\partial x}$$

to increase with eddy strength; however, the length of time a parcel spends in the upwelling or downwelling phase decreases. The time-integrated stretching remains similar for flow speeds in the range 20 to 100 cm s^{-1}. An experiment with an infinitely deep lower layer (so that $\mathbf{u}_2 = 0$) isolates the kinematic effect. The resulting vertical velocities are purely dipolar. The dynamical effects from the second term clearly alter the structure significantly; the vertical velocity now has a strong quadrupole moment as well and is somewhat larger. As Bryden (1979) noted, turning of the horizontal velocity with depth is diagnostic of vertical velocities in a steady flow; it allows the velocity vector and the gradient of the buoyancy to be nonparallel, so that advection of density contributes to w. Thus, the efficacy of the induced flux depends critically on the details of the propagation mechanism (McGillicuddy et al., 1995).

As an example of the biological effects, we use the NPZ model of Section 1 but take the light level to be averaged over the upper 50 m and presume that the upwelling fluid has only nutrients, while the downwelling fluid carries phytoplankton and zooplankton below the euphotic zone, whereupon they decay back to N. As Flierl and Davis (1993; hereafter, FD93) show, this simple mixed layer model gives a sink term on the P and Z equations:

$$\frac{\partial}{\partial t} p_i + \mathbf{u} \cdot \nabla p_i = \mathcal{P}_i + \begin{cases} p_i \dfrac{\partial w}{\partial z}, & w > 0 \\ 0, & w < 0 \end{cases} \tag{24}$$

Figure 4.19 shows the phytoplankton and zooplankton fields at different times. We

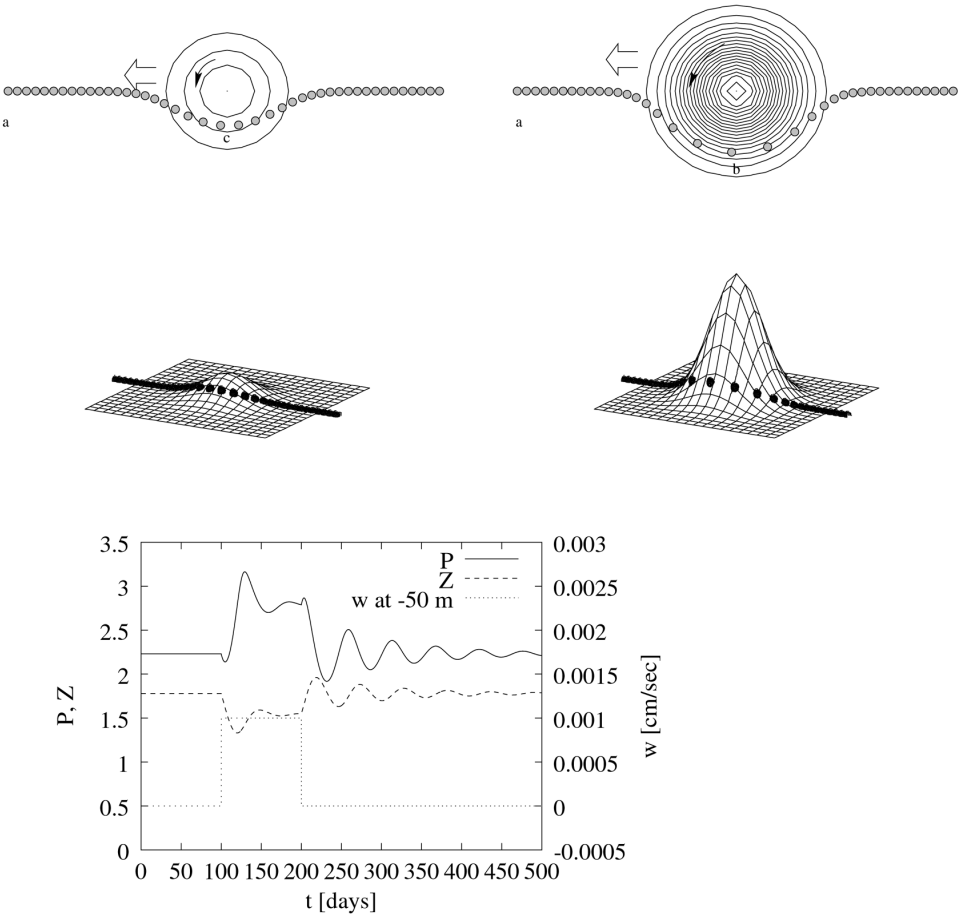

Fig. 4.18. Vertical motions associated with eddy translation. The upper panels show the motion of a particle relative to a cyclonic eddy moving westward; the middle panels give a three-dimensional view showing the vertical excursion as well. For the left sides, the maximum swirl velocity is 0.09 cm s^{-1}; for the right 0.4, with the translation speed being 0.2. The lower figure shows the response of the NPZ model to a transient upwelling event.

can understand this behavior by considering the response to a single upwelling event (Fig. 4.18; see also FD93, Fig. 6.1); initially, the concentration of P and Z is reduced by dilution. But the upwelling brings nutrients up for the phytoplankton and they respond quickly; the zooplankton are affected mostly by the dilution and have a reduction in population overall. Maintained upwelling in essence increases the death rates of both groups, which leads to higher phytoplankton and lower zooplankton equilibria. When the upwelling shuts off, the populations spiral back to the original equilibrium; this is the period in which the zooplankton may have temporary increases in density. The figure shows this behavior with initial decreases in both, followed by a phytoplankton increase and a banded zooplankton structure. The variation in P is about 8% of the mean and in Z about 6%.

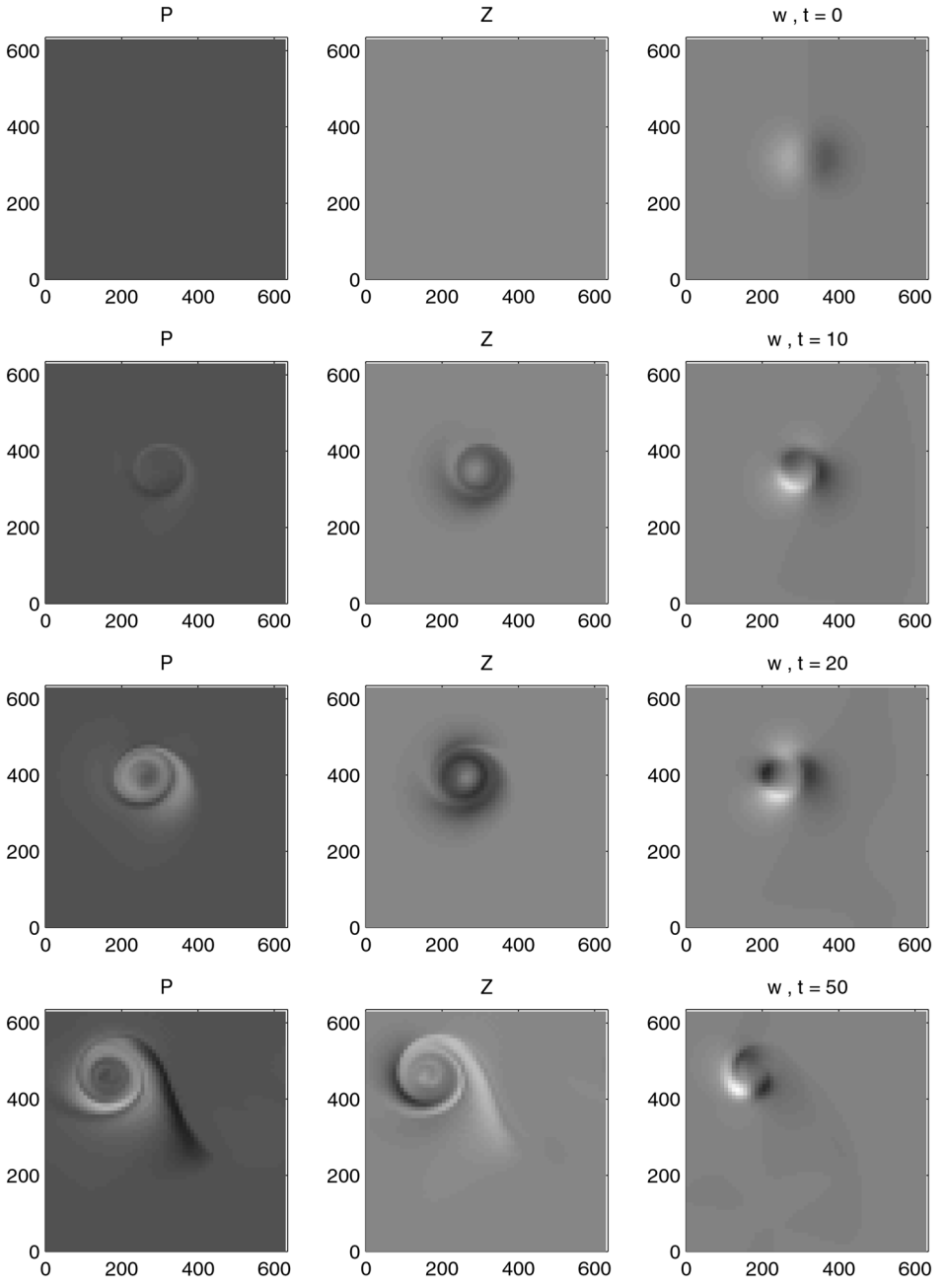

Fig. 4.19. Evolution of P and Z in eddy. Greyscale ranges correspond to (2.15, 2.4) for P and (1.7, 1.85) for Z.

6.5. Multiple Eddies

The dynamical contribution to upwelling becomes even more significant when multiple eddies interact [McGillicuddy et al., 1995; McGillicuddy and Robinson, 1997a (hereafter MR97)]. Using a coupled quasigeostrophic and surface boundary layer model, MR97 constructed long-term (multiyear) aseasonal (summertime) simulations characteristic of the mesoscale eddy environment in the Sargasso Sea. Incorporation of a simplified biological model into these calculations facilitated study of the mechanisms by which eddy processes can transport nutrients into the euphotic zone. Results show that upwelling due to the formation of cyclonic eddies and subsequent intensification caused by interaction with surrounding features cause sporadic nutrient injections into the surface layer.

A typical eddy-driven nutrient injection event extracted from the MR97 simulations is shown in Fig. 4.20. On day 2740, a cold eddy is entering the field of view from the east. It is interacting with a pair of warm features to the northwest. Over the next 15 days the two warm eddies merge and the cold eddy intensifies as the entire interacting complex propagates westward. During this time the cold feature develops an elongate tail which streams out to the northeast. By day 2770 the vortex tail has dissipated and the cold eddy has intensified as it takes on a nearly circular form. The interacting warm feature has also revolved counterclockwise around the cold eddy. The nutrient flux distribution corresponds directly to the eddy dynamics. Upwelling in the interior of the cold eddy due to its intensification associated with the warm eddy interaction lifts nutrients into the euphotic zone.

The mechanism can be conceptualized by considering a density surface with mean depth coincident with the base of the euphotic zone. This surface is perturbed vertically by the formation, evolution, and destruction of mesoscale features. Shoaling density surfaces lift nutrients into the euphotic zone, where they are rapidly utilized by the biota. Deepening of the isopycnals pushes nutrient-depleted water out of the well-illuminated surface layers. The asymmetric light field thus rectifies vertical displacements of both directions into a net upward transport of nutrients, which is presumably balanced by a commensurate flux of sinking particulate material. Two aspects of this process favor complete utilization of the upwelled nutrients. First, the time scale for biological uptake is fast (order of days) with respect to the physical supply mechanism (eddy lifetimes on the order of months). Second, because the nutrient enhancement takes place in the eddy's interior, the circulation tends to isolate it from the surrounding waters, which allows biomass to accumulate until the nutrients are exhausted.

It is important to point out that the eddy-induced flux depends not only on the vertical structure of the isopycnal displacements, but also on the sense in which they are being perturbed by the eddy dynamics. The latter characteristic is largely determined by the developmental stage of the eddy within its lifetime (i.e., whether it is in the process of formation/intensification or decay). We can consider these two stages of eddy development for three different characteristic vertical structures: a cyclone (which lifts both the seasonal and main thermoclines), an anticyclone (which depresses both the seasonal and main thermoclines), and a mode-water eddy (which lifts the seasonal thermocline and depresses the main thermocline). The process of eddy formation and intensification leads to upwelling in the near-surface region in the cases of cyclones and mode-water eddies, and downwelling in the case of anticy-

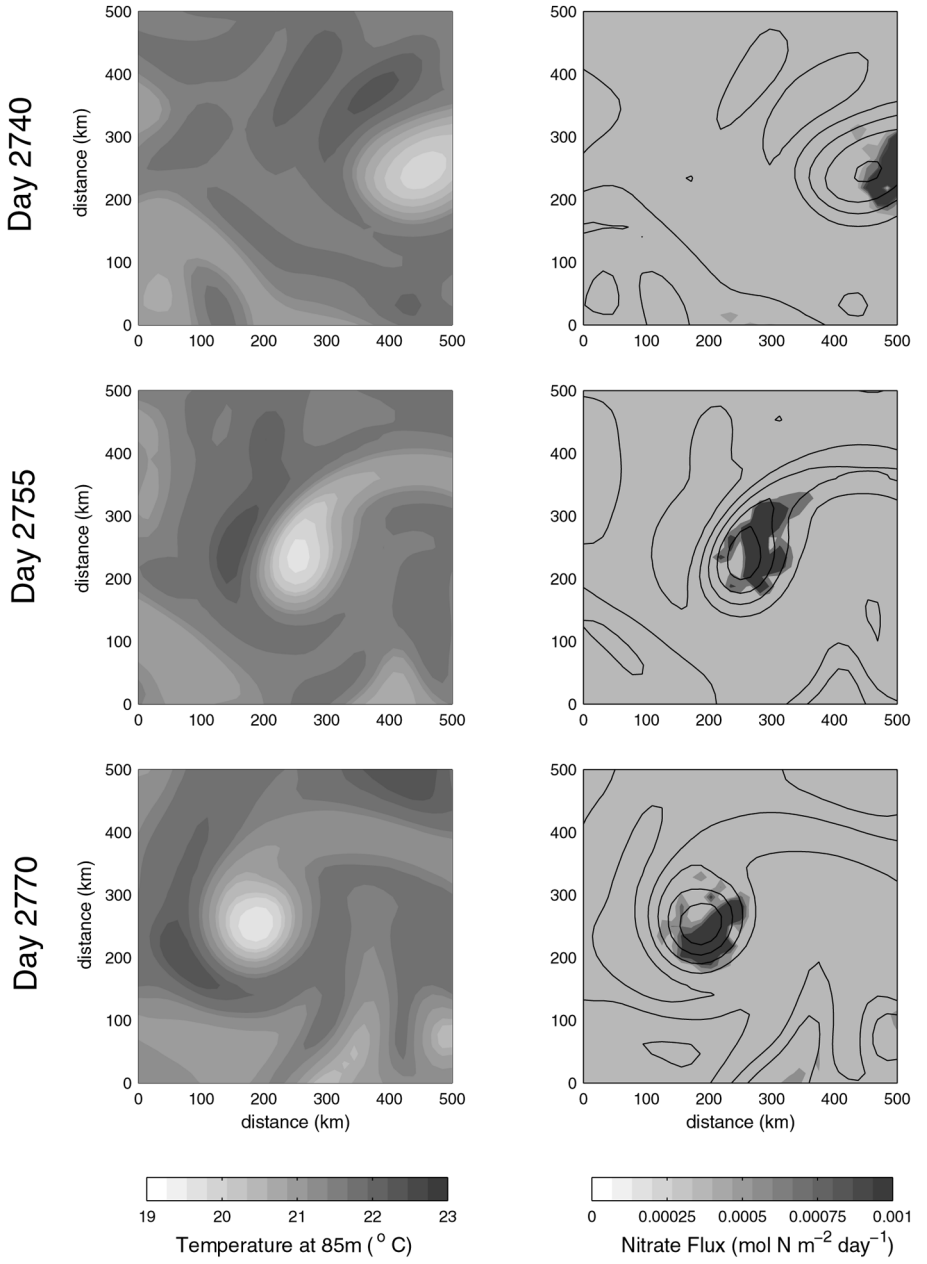

Fig. 4.20. See color insert. Typical eddy-driven nutrient injection event extracted from the MR97 simulations: temperature at 85 m (left column) and nitrate flux across the base of the euphotic zone (right column). For convenience, temperature contours from the left-hand panels are overlaid on the nutrient flux distributions. The area shown here is a 500-km^2 subdomain.

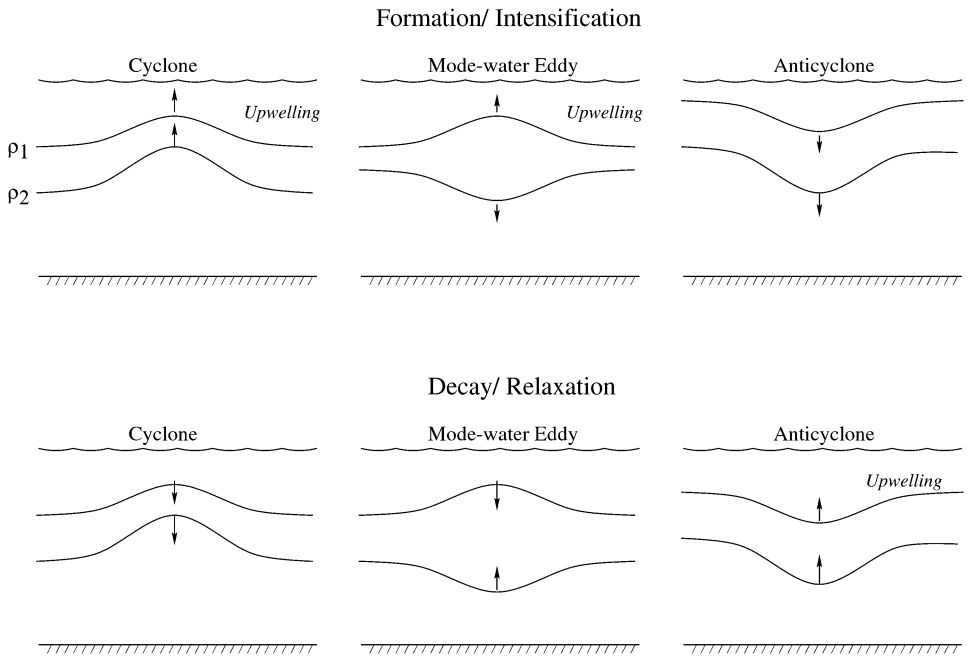

Fig. 4.21. Isopycnal displacements associated with three types of eddies in the process of formation/intensification (top row) and decay (bottom row). Two density surfaces are depicted in each case: one in the seasonal thermocline (ρ_1) and one in the main thermocline (ρ_2).

clones (Fig. 4.21). Conversely, relaxation of the density perturbations associated with eddy decay results in upper ocean downwelling in cyclonic features and mode-water eddies, while causing *upwelling* within anticyclones.

Several different lines of evidence suggest that eddy-driven nutrient flux represents a large portion of the annual nitrogen budget in the Sargasso Sea (McGillicuddy et al., 1998). The high-resolution regional numerical simulations of MR97 indicate that the magnitude of the eddy-induced upwelling caused by cyclonic eddy formation and intensification is sufficient to balance the nutrient demand implied by geochemical estimates of new production. Nitrate flux calculations based on satellite altimetry and a statistical model linking sea level anomaly to subsurface isopycnal displacements provide estimates of comparable order (Siegel et al., 1999). Oschlies and Garçon (1998) showed that including eddies in a basin-scale simulation of the North Atlantic significantly increased productivity over a coarse resolution case. Observations of a nutrient pulse caused by the passage of a mesoscale eddy were obtained using novel chemical sensing technology deployed on the Bermuda Testbed Mooring (McNeil et al., 1999). Finally, mesoscale biogeochemical surveys in the Sargasso Sea have revealed that variations in upper ocean nutrient and pigment distributions are largely controlled by vertical isopycnal displacements associated with the eddy field (McGillicuddy et al., 1999).

At least two types of eddies are involved in nutrient transport in the Sargasso Sea. The mooring observations and shipboard surveys described above have revealed evidence of eddy-induced upwelling associated with both cyclones and mode-water

eddies. Analysis of the hydrographic time series at Bermuda suggests that mode-water eddies are rare in comparison to more typical cyclones, occurring only four times in 9 years of biweekly to monthly observations (Siegel et al., 1999), although sampling remains an issue. Thus, the relative importance of the two types of features remains an open question because so few events have been sampled directly.

Another example of eddy-induced upwelling comes from the frictional decay of anticyclonic warm-core rings north of the Gulf Stream. Flierl and Mied (1985) formulated a model of the vertical circulations that result from relaxation of the depressed density surfaces in the interiors of such features. By incorporating a simple plankton ecosystem into this model of warm-core ring 82B, Franks et al. (1986) demonstrated how a lens of phytoplankton biomass enhancement could result from the nutrient input caused by the approximately 1 m day^{-1} vertical velocities at ring center. Nelson et al. (1989) documented nitrate and silicic acid uptake rates by phytoplankton in the same ring which were sufficient to utilize the upward flux of nutrients. Thus, we have evidence for the biological ramifications of eddy-induced upwelling in at least three different type of features.

7. Eddy Transport, Stirring, and Mixing

Since ocean eddies behave as a complex mix of waves and turbulence, we must understand how each type of motion transports the biota. We begin with waves.

7.1. Stokes' Drift and Displacements

Although our early science lessons may have taught that waves do not result in net movement of particles, Stokes, in 1847, demonstrated that finite-amplitude gravity waves actually can transport material. His results apply to other types of waves, including the Rossby wave in a channel (Flierl, 1981), which we have used previously as an example flow (equation 21, Fig. 4.10). At the walls, the flows are purely zonal, with the particles moving back and forth. But they spend more time in the phase when they are moving prograde, because the relative velocity (wave–particle) is smaller, and they spend less time in the retrograde phase when the relative velocity is large. As a result, the average Lagrangian velocity is prograde. At the center of the channel, the situation is quite different. In this case, the north–south flows (which are 90° out of phase with the east–west motions) push the particle into regions where the flow is retrograde. The trajectories are shown in Fig. 4.22. For larger amplitude, the paths become more complex, with trapped (prograde) regions in which the particles return periodically to the same point relative to the wave (not offset by a wavelength) interleaved by strongly retrograde regions.

Let us now consider small-amplitude motions in detail and see how the particle drift relates to transport. We can solve for the displacement $\boldsymbol{\xi}(\mathbf{x}, t)$ of a parcel initially at position $\mathbf{x}$ by successive approximation:

$$\frac{d}{dt}\,\xi_i = u_i(\mathbf{X}+\boldsymbol{\xi}, t) \simeq u_i(\mathbf{x}, t) + \xi_j\,\frac{\partial}{\partial x_j}\,u_i(\mathbf{x}, t) + \cdots$$

The estimated mean Lagrangian motion satisfies

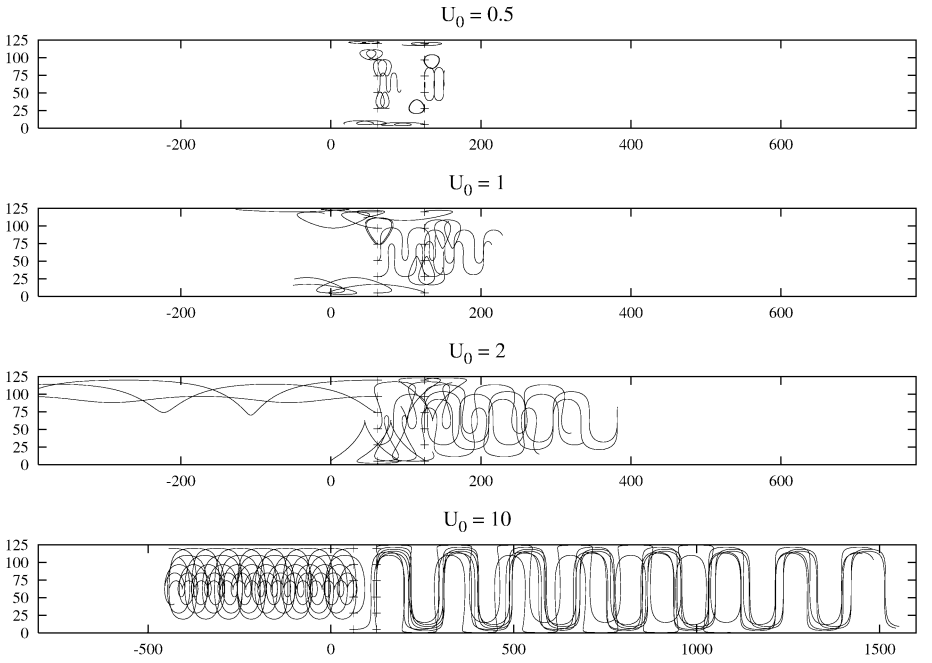

Fig. 4.22. Trajectories of particles in waves with various amplitudes. The title above each plot gives the wave amplitude (U_0 in equation 21) in km day^{-1}. The particles are set across the channel at the points marked by the +'s, one quarter wavelength apart (x = 75 km and x = 125 km). The trajectories run for one year. The phase speed is −1.4 km day^{-1}.

$$u_i^L \equiv \left\langle \frac{d}{dt}\ \xi_i \right\rangle = \frac{\partial}{\partial x_j}\ \langle u_i(t)\xi_j(t)\rangle = \frac{\partial}{\partial x_j}\ \left\langle \int_0^t u_i(t)u_j(t')\ dt' \right\rangle = \frac{\partial}{\partial x_j}\ \int_0^t R_{ij}(t-t')$$

(assuming zero mean Eulerian velocity). We can split the covariance matrix $R_{ij}(\tau)$ into a symmetric part:

$$K_{ij} = \int_0^t \frac{1}{2}\ [R_{ij}(\tau) + R_{ji}(\tau)]\ d\tau \tag{25}$$

which, as we shall see, corresponds to turbulent diffusion (Taylor, 1921) and an anti-symmetric part A_{ij}. The gradients of the latter can be viewed as an advective velocity:

$$u_i^S = \frac{\partial}{\partial x_j}\ A_{ij} = \frac{\partial}{\partial x_j}\ \int_0^t \frac{1}{2}\ [R_{ij}(\tau) - R_{ji}(\tau)]\ d\tau \tag{26}$$

which is clearly nondivergent. Thus, we have two contributions to the drift:

$$u_i^L = \frac{\partial}{\partial x_j} K_{ij} + u_i^S \tag{27}$$

For the Rossby wave example (equation 21) we can find the covariance by averaging over the phase θ, giving

$$K_{11} = \frac{U_0^2}{2ck} \sin kct \cos^2 ly, \qquad K_{22} = \frac{U_0^2 k}{2cl^2} \sin kct (1 - \cos^2 ly)$$
$$A_{12} = -A_{21} = \frac{U_0^2}{4lc} \sin 2ly (1 - \cos kct), \qquad \mathbf{u}^S = \frac{U_0^2}{2c} \cos 2ly (1 - \cos kct)\hat{\mathbf{x}} \tag{28}$$

In the time average, the flow is nondiffusive, and there is an along-channel drift.

As a second, more complex example, consider a randomly forced channel wave. Dynamically, this is presumed to satisfy

$$\frac{\partial}{\partial t} \nabla^2\psi + J(\psi, \nabla^2\psi + \beta y) = \lambda \, \mathrm{Re}[r(t)e^{ikx}] \sin ly - \lambda\nabla^2\psi \tag{29}$$

where $r(t)$ is a random time series taking values on a disk of radius r_0 [i.e., $\langle r(t)r^*(t')\rangle = \frac{1}{2}r_0^2\delta(t - t')$] and the parameter λ represents bottom drag. The stream function is

$$\psi = \mathrm{Re}[a(t)e^{ikx}] \sin ly$$

with

$$\frac{d}{dt} a + (\lambda + i\omega)a = \frac{\omega\lambda}{\beta k} r, \qquad \omega = -\frac{\beta k}{k^2 + l^2} \quad \text{(Rossby wave frequency)}$$

We can find the correlation function for ψ and take suitable derivatives to obtain

$$R_{ij}(\tau) = \frac{1}{2} U_0^2 e^{-\lambda\tau} \begin{bmatrix} \cos \omega\tau \cos^2 ly & \frac{k}{l} \sin \omega\tau \sin ly \cos ly \\ -\frac{k}{l} \sin \omega\tau \sin ly \cos ly & \frac{k^2}{l^2} \cos \omega\tau \sin^2 ly \end{bmatrix}$$

with $U_0 = \omega\lambda^{1/2} r_0 l/2\beta k$ being the characteristic zonal velocity. Carrying out the integrals in equations 25 and 26 gives the nonzero terms

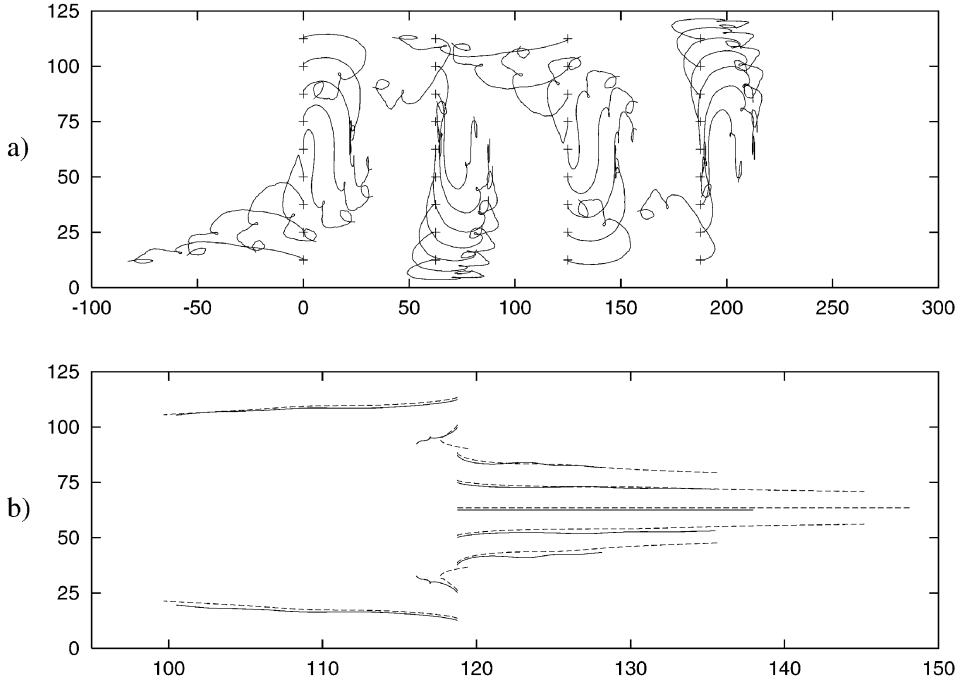

Fig. 4.23. Some trajectories in the randomly forced problem (upper) and the mean motions for an ensemble of 200 experiments (lower): dashed lines are the mean trajectories predicted from 1.30. The waves are weak ($U_0 = 0.5$ km day^{-1}), and the decorrelation time ($1/\lambda = 100$ days) is shorter than the wave period of 183 days.

$$K_{11} = \frac{1}{2}\, U_0^2\, \frac{\lambda}{\lambda^2+\omega^2} \cos^2 ly, \qquad K_{22} = \frac{1}{2}\, U_0^2\, \frac{k^2}{l^2}\, \frac{\lambda}{\lambda^2+\omega^2} \sin^2 ly$$

$$A_{12} = -A_{21} = \frac{1}{2}\, U_0^2\, \frac{k}{l}\, \frac{\omega}{\lambda^2+\omega^2} \sin ly \cos ly, \qquad u^S = \frac{1}{2}\, U_0^2 k\, \frac{\omega}{\lambda^2+\omega^2} \cos 2ly \tag{30}$$

The finite decorrelation time for the flow now makes the motion dispersive (with anisotropic eddy diffusivities). In Fig. 4.23 we show sample trajectories in a weakly forced problem ($U_0/c \sim 0.2$) which illustrate both the dispersion and the drift.

Now let us examine the transport of biological properties and passive scalars to understand both the identification of K_{ij} with diffusion and the modifications that enter because of biological interactions. We assume that the perturbations induced by the advection are small, that biological movements and mixing are unimportant, and that the waves dominate over the mean flow. Then

$$\frac{\partial}{\partial t}\, p_i' - \mathcal{P}_{ij} p_j' = -u_n'\, \frac{\partial}{\partial x_n}\, \overline{p}_i$$

The solution

$$p_i'(t) = -\int_0^\infty e^{\tau \mathcal{P}_{ij}} u_n'(t-\tau)\, \frac{\partial}{\partial x_n}\, \overline{p}_j$$

is well behaved as long as all the real parts of the eigenvalues of $\mathcal{P}_{ij}$ are negative. We can now evaluate the eddy fluxes of the biological properties

$$\langle u_m'(t) p_i'(t) \rangle = -\left[\int_0^\infty e^{\tau \mathcal{P}_{ij}} R_{mn}(\tau) \right] \frac{\partial}{\partial x_n}\, \overline{p}_j \tag{31}$$

We can again split out the symmetric and antisymmetric parts,

$$\langle u_m p_i' \rangle = -K_{mn;\,ij}\, \frac{\partial}{\partial x_n}\, \overline{p}_j + u^S_{m;\,ij} \overline{p}_j$$

dropping a term that is spatially nondivergent and cannot affect the mean fields. Summation over both spatial coordinate index n and the biological variable number j is implied here. The effective Stokes' drift becomes

$$u^S_{m;\,ij} = \frac{\partial}{\partial x_n} \left[\frac{1}{2} \int_0^\infty e^{\tau \mathcal{P}_{ij}} R_{mn}(\tau) - \frac{1}{2} \int_0^\infty e^{\tau \mathcal{P}_{ij}} R_{nm}(\tau) \right]$$

and the effective diffusivity is

$$K_{mn;\,ij} = \frac{1}{2} \int_0^\infty e^{\tau \mathcal{P}_{ij}} R_{mn}(\tau) + \frac{1}{2} \int_0^\infty e^{\tau \mathcal{P}_{ij}} R_{nm}(\tau)$$

For a passive scalar, $\mathcal{P}_{ij} = 0$, these reduce to equations 25 and 26; thus, the flux is indeed a combination of advection by the Stokes' drift velocity $\mathbf{u}^S p$ and eddy diffusion $-K_{mn}(\partial/\partial x_n)\overline{p}$. For biologically active variables, the situation is quite different for two reasons: We must sum over the biological variables and the coefficients will depend on the decay times inherent in $\mathcal{P}_{ij}$. We can see two important properties of the wave-induced transports and mixing:

1. The diffusive flux of one property (e.g., phytoplankton concentration) depends not only on its gradient but the gradients of other properties as well. Advection by the Stokes' drift also depends on the values of the other variables. For example, consider Figs. 4.3 and 4.7: even though $\overline{P}$ is uniform in the surface layer, upward movement of a parcel will cause P to begin to increase, since the uptake term is out of balance with the grazing—the parcel retains its lower Z value. When the parcel moves back down, P will again change, but it will generally not return to its original value, so that there will be a net flux of P associated with the Z gradients.

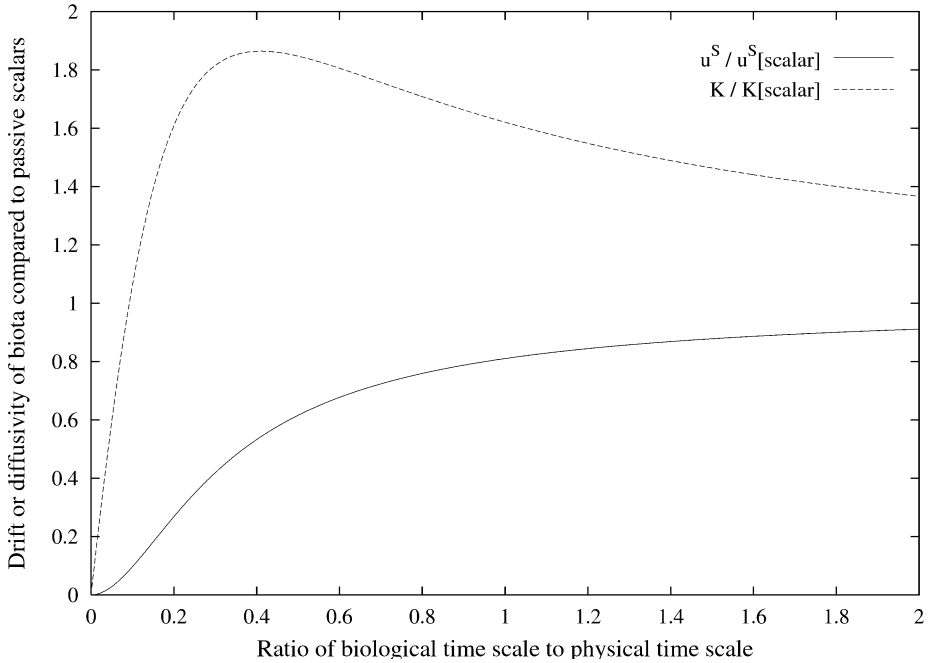

Fig. 4.24. Maximum values across the channel of the Stokes drift and diffusivity for different biological time scales compared to physical decorrelation times ($\lambda/d_1\overline{P}$). These are found by taking the ratio of the terms in 1.30 with λ replaced by $\lambda + d_1\overline{P}$ to the terms as written; thus u^s[bio]/u^s[scalar] = ($\lambda^2 + \omega^2$)/([$\lambda + d_1\overline{P}$]$^2 + \omega^2$) and K[bio]/K[scalar] = ([$\lambda + d_1\overline{P}$]/$\lambda$) × ($u^s$[bio]/$u^s$[scalar]).

2. The transport coefficients are not the same as those applying to passive scalars. For example, let us consider a single-variable system such as the logistic equation 3, where $\mathcal{P}_{11} = -d_1\overline{P}$. The Stokes drift and diffusivities for our randomly forced Rossby wave case can be found by replacing λ with $\lambda + d_1\overline{P}$ in equation 30. Essentially, the biology decorrelates more rapidly than the passive scalars (which are affected only by the decorrelation of the flow); as a result, the effective diffusivities are higher and the Stokes' drifts weaker (Fig. 4.24).

For complex biology, we can write $\mathcal{P}_{ij}$ in terms of its eigenmodes:

$$\mathcal{P}_{ij} = E_{ik}\sigma_k E^{-1}_{kj}$$

and obtain complicated expressions for the transport coefficients:

$$u^S_{m;ij} = \frac{\partial}{\partial x_n} E_{ik}\left[\frac{1}{2}\int_0^\infty e^{\tau\sigma_k}R_{mn}(\tau) - \frac{1}{2}\int_0^\infty e^{\tau\sigma_k}R_{nm}(\tau)\right]E^{-1}_{kj}$$

with similar expressions for $K_{mn;ij}$. Since each mode will have a different decay time, it will advect and diffuse at rates different both from passive scalars and from other modes. The net transport by eddies is therefore complex and also quite model dependent (cf. Wroblewski and O'Brien, 1981). While the formulas above could provide

a parameterization of the transport, the implication seems to us to be that resolving the eddies explicitly in simulations is going to be more fruitful and illuminating.

7.2. Chaotic Mixing and Transport

When the wave amplitude becomes large (so that the fluid speeds exceed the propagation speed of the wave), trapped regions develop where particles are carried along with the wave in its motion (refer to Fig. 4.22). The boundary of the trapped fluid is a streamline in the moving frame and passes from one stagnation point on the wall to a second one farther east. Particles near this boundary spend a long time in the vicinity of the stagnation point, with those on the bounding streamline taking an infinite time to leave the wall on one end and to reach the wall on the other. Thus, we can anticipate that these regions play an important part in mixing (Dewar and Flierl, 1985). If the flow is not a pure, steadily propagating wave but has some other weak variability (even periodic), particles will be shifted across the bounding streamline. Which side they end up on after passing by the stagnation point depends on the precise sequence of back-and-forth motions. Figure 4.25 shows an example of this behavior, produced by arranging the forcing in equation 29 so that the wave amplitude oscillates by 10%. We see that fluid is entrained into and detrained from the trapped area near the rear stagnation point. In essence, chaotic mixing occurs because particles approaching a stagnation point will be ejected to one side or another, but which side is selected depends very sensitively on the starting position and time, so that particles that are initially close together or that pass the same point at different times can end up widely separated.

8. Instabilities and Generation of Eddies

Ocean eddies can be formed by a number of different processes: direct generation by wind, shedding from topography, localized convection (Legg and Marshall, 1993), seasonal variability, and so on. But instability of the wind- and thermally driven circulations (including, of course, the western boundary currents and other jets) is the most probable cause of energetic mesoscale motions. These instabilities extract either kinetic energy (from the horizontal shear) or potential energy (from the horizontal density gradients, which, by the thermal wind relationship, are connected with the vertical shears).

Some of the first investigations of mesoscale effects on upper ocean biota focused on the dynamics of mesoscale jets (Woods, 1988). Jet meandering can lead to large changes in relative vorticity which must be compensated by changes in layer thickness in order to conserve potential vorticity. These vortex stretching terms give rise to very high vertical velocities (order 10 to 100 m day^{-1}) that occur in submesoscale patches along the flanks of the meander systems. This type of vertical motion has been measured directly with Lagrangian floats deployed in the Gulf Stream (Bower and Rossby, 1989), inferred from hydrographic observations of fronts in the subtropical convergence zone (Pollard and Regier, 1992), and simulated numerically (Onken, 1992). Strass (1992) documented evidence of chlorophyll patchiness on the scale 10 to 20 km that is characteristic of mesoscale upwelling at fronts. Flierl and Davis (1993) incorporated a simple ecosystem into a model of the Gulf Stream that included intense vertical transports of this nature. Their results show that upwelling in the flank

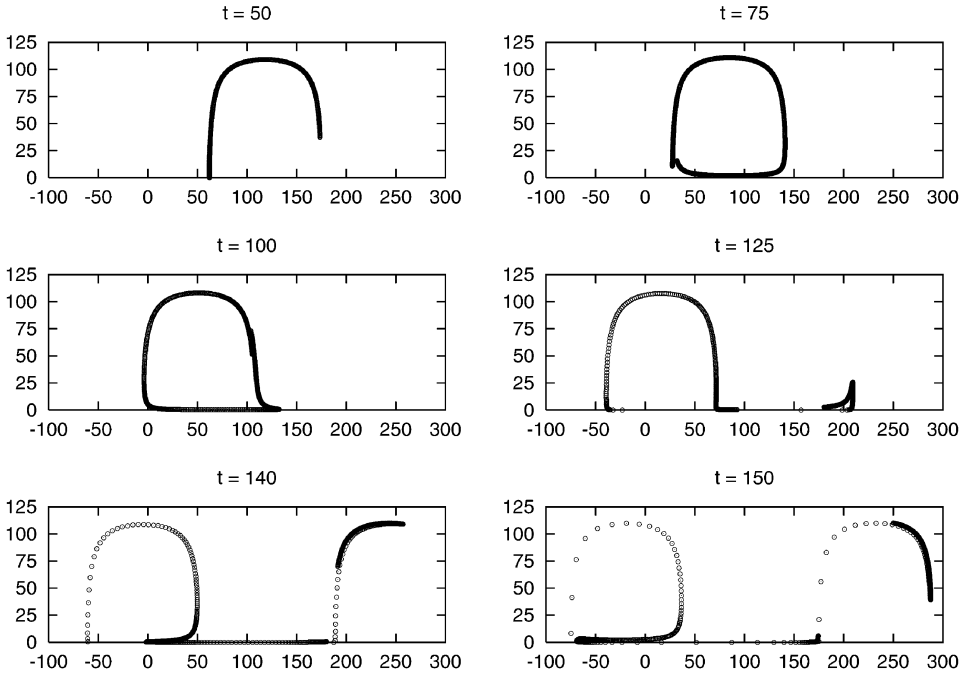

Fig. 4.25. Particle motion in a periodically varying wave. The beginning of the segment moves to the left of the stagnation point, while the end part moves to the right. Eventually, the particles mix throughout a band around the stagnation streamline. $U_0 = 10$ km day^{-1}, $c = -1.4$ km day^{-1}, and the amplitude oscillates with a period of 91 days.

of a meander can in fact stimulate the growth of phytoplankton. However, upwelled fluid is subsequently advected downstream into a region of downwelling that tends to suppress the biological response. The key question with respect to net impact on the biota is how the time for transit between upwelling and downwelling patches compares to the time required for full utilization of upwelled nutrients. In the Gulf Stream case studied by FD93, relatively rapid horizontal advection prevents the biological response from going to completion, thereby limiting the net enhancement of phytoplankton biomass and productivity to 10 to 20%. However, the upwelling and development were also relatively weak because FD93 dealt with stable jets. We shall extend their work to unstable jets, examining both barotropic and baroclinic growth to see how each works and how each might affect the biology.

8.1. Barotropic Jet

Let us begin with a jet that has no vertical shear:

$$u = U_0 \operatorname{sech}^2(y/L), \qquad v = w = 0$$

For this flow the variable part of the potential vorticity is $-(\partial/\partial y)\,u$ (Fig. 4.26*a*), so that the PV gradient is negative on the sides of the jet and positive in the center. Consider a wave that perturbs the PV contours as shown. If we calculate the flows

induced by the anomalies in Q along the centerline, we see that they tend to increase the disturbances in the wings of the jet. Similarly, the anomalies in the wings tend to magnify the displacement of the centerline. Clearly, this configuration will lead to growth in the disturbance if we can maintain the phase relationships shown (i.e., if the waves in the wings slide by 180° relative to the center, the induced flows would instead mutually decrease the perturbations). The shear in the jet will try to shift the central wave eastward while the Rossby wave processes will cause a westward propagation in the center and eastward on the edges. For long-enough wavelengths, this propagation is sufficiently fast that the waves can remain in phase. In the case when the PV gradients are everywhere positive, the argument above fails because no organization of the waves in the different regions leads to increase in all perturbations—one will always decrease while the others are increasing. This is the basic physics behind Rayleigh's theorem, which states that instability can occur only when the PV gradient changes sign.

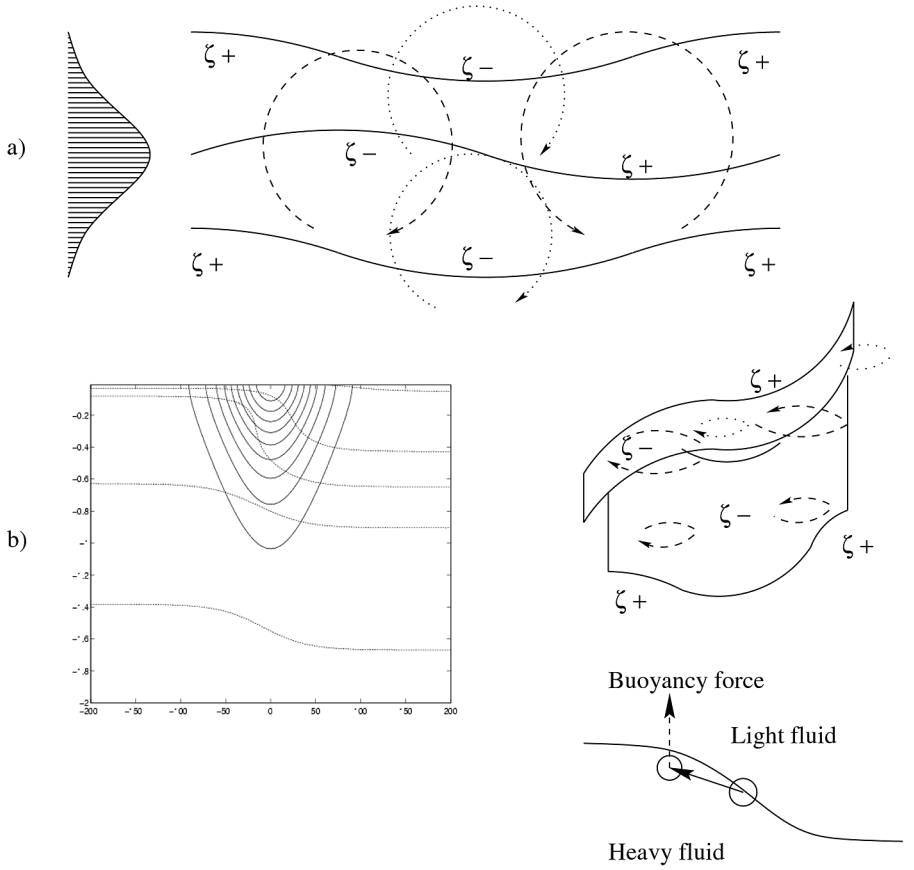

Fig. 4.26. (*a*) Instability mechanism for barotropic jet, showing the Q contours, sign of ζ, and induced flows; (*b*) velocity and PV fields for a baroclinic jet and instability mechanism in terms of PV anomalies and of buoyancy forces which have positive projections along the original displacement vector, thereby tending to increase the displacement.

Figures 4.27 and 4.28 show the evolution of the disturbance and the transport by the developing instability. For the particular configuration we are using, the instability has two phases, one in which the perturbations grow and break the jet into a *vortex street* with the positive vortices on the north side and the negative ones on the south. However, this configuration suffers a secondary instability and the vortices merge to form a larger street. The flow is now constrained by the geometry (a channel), so that the final larger-scale pattern decays only by viscosity. The tracer is entrained somewhat into the initial street but is mixed much more effectively as the vortices merge.

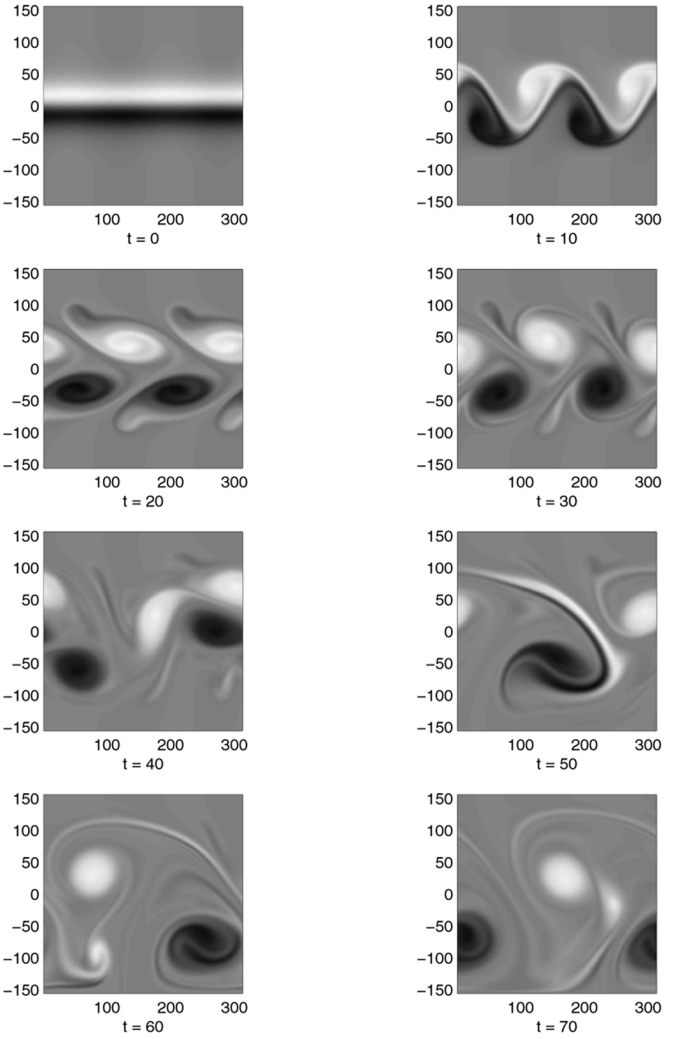

Fig. 4.27. Development of the instability of a barotropic jet. The Q field is shown with the gray scale range from -2 to 2 day^{-1}.

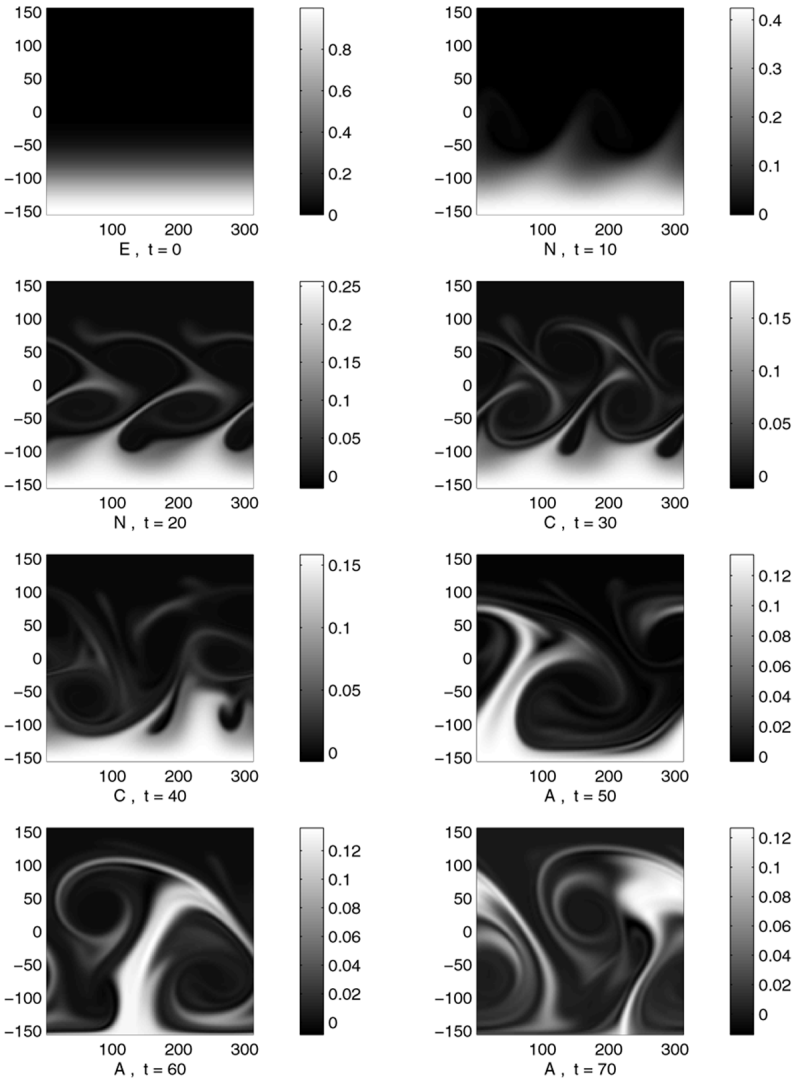

Fig. 4.28. See color insert. Development of a copepod population in the unstable jet, beginning with a cohort of eggs near the shore. The passive scalar pictures look almost the same, except the gray scale would be the same (0 to 1) for all the pictures.

If we consider the development of a copepod population that is born near the shore at the time when this wave is developing, we see patterns such as those in Fig. 4.28. The early stages appear nearshore, with entrained filaments extending around the street, while the later stages are drawn far offshore by the turbulence induced when the vortices merge. We have chosen a rather dramatic case in which the instability develops rather strongly during the time when the copepods are developing; in general, we would expect to see many different patterns, depending on the exact state of the flow when the eggs are produced.

8.2. *Baroclinic Jet*

A second form of instability, associated with the vertical shear and the horizontal density gradients, is also likely to be an important source of eddies. This type, called *baroclinic instability*, draws its energy from the potential energy associated with the jet. Since the density surfaces tilt, some heavier water is higher and some lighter water is lower than they would be if the isopycnals were level. Thus potential energy will be released if the isopycnals level out. To understand the instability process, we can examine the potential vorticity structure of a baroclinic jet

$$u = \operatorname{sech}^2 y \, \frac{h_1 e^{z/h_1} - h_2 e^{z/h_2}}{h_1 - h_2}$$

(Fig. 4.26*b*); the PV gradient is positive in the upper water column and negative in the deep water. In essence, the uplifting of the thermocline to the north results in stronger stratification (higher PV) near the surface compared to the southern side and weaker stratification (lower PV) in the deep water. The mechanism for the instability is again the mutual reinforcement of waves on the two PV gradients (Fig. 4.26*b*). Where the upper front (sharp PV gradient region) is pushed northward, we have negative PV anomalies, causing anticyclonic flow throughout the water column. If the crest in the lower layer front lags behind (to the west), its displacement will be enhanced. The flows induced by the perturbation in the lower layer front position in turn cause cyclonic flows that enhance the upper disturbance (see Meacham, 1991). Figure 4.29 shows the development of such a disturbance calculated with a two-layer QG model; pinched-off rings are formed and interact with each other and with the jet to form a complex, turbulent flow.

Baroclinic instability also induces significant vertical motions. We can use an energy argument to demonstrate this: Consider the perturbation momentum equations (from equations 11 to 13)

$$\frac{\partial}{\partial t}\,\mathbf{u}' = -\overline{2\boldsymbol{\Omega}_{\text{eff}}} \times \mathbf{u}_3' - 2\boldsymbol{\Omega}_{\text{eff}}' \times \overline{u}\hat{\mathbf{x}} - \nabla(\phi' + \overline{u}u') + b'\hat{\mathbf{z}}$$

$$\frac{\partial}{\partial t}\,b' = -\overline{u}\,\frac{\partial}{\partial x}\,b' - v'\,\frac{\partial \overline{b}}{\partial y} - w'\left(\frac{\partial \overline{b}}{\partial z} + N^2\right)$$

The evolution of the perturbation kinetic energy ($K' \equiv \langle \frac{1}{2}|\mathbf{u}'|^2 \rangle$, with the $\langle\cdot\rangle$ representing a volume average) is found by dotting the momentum equation by $\mathbf{u}' + w'\hat{\mathbf{z}}$ and integrating:

$$\frac{\partial}{\partial t}\,K' = \left\langle \overline{u}v'\,\frac{\partial}{\partial y}\,u' \right\rangle + \left\langle \overline{u}w'\,\frac{\partial}{\partial z}\,u' \right\rangle + \langle w'b' \rangle$$

$$= -\left\langle u'v'\,\frac{\partial \overline{u}}{\partial y} \right\rangle - \left\langle u'w'\,\frac{\partial \overline{u}}{\partial z} \right\rangle + \langle w'b' \rangle$$

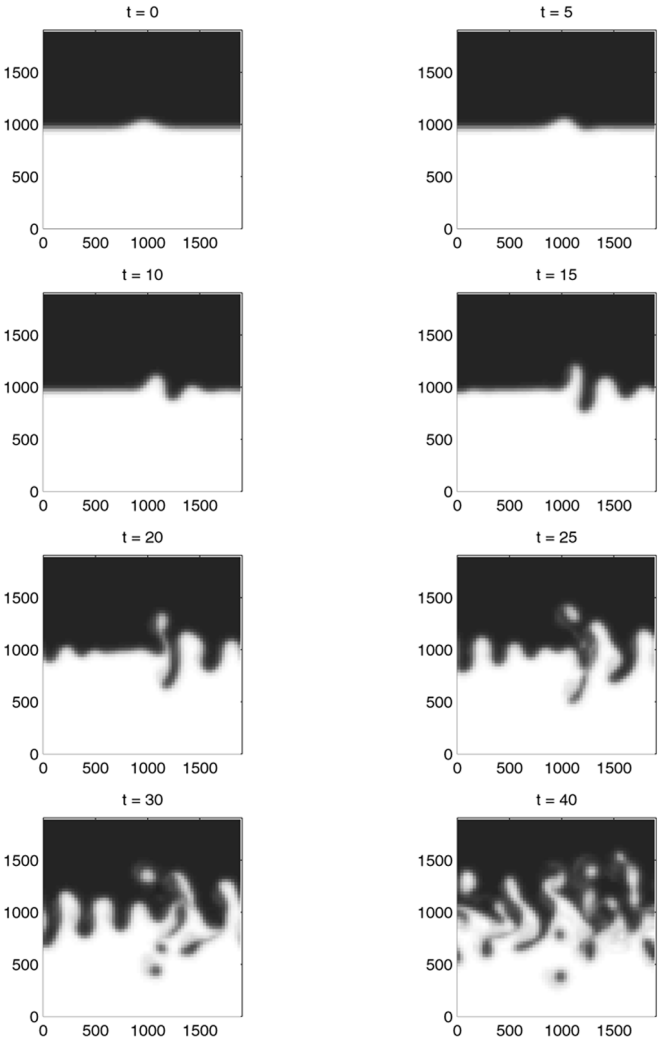

Fig. 4.29. Baroclinic instability of a jet. The field shown is the thermocline depth h. Gray scale range is 200 to 1000 m.

assuming that the normal flow vanishes at the boundaries. A downgradient flux of zonal momentum releases energy from the mean allowing growth of the perturbation. In essence, a uniform flow has less kinetic energy than a nonuniform flow with the same momentum $\langle \frac{1}{2}\overline{u}^2 \rangle > \frac{1}{2}\langle \overline{u} \rangle^2$; hence, flattening the profile gives energy that can be put into the perturbation. Perturbation kinetic energy can also be generated when light fluid rises and heavy fluid sinks. The vertical flux of zonal momentum term is important for Kelvin–Helmholtz instabilities (leading to growing and breaking internal gravity waves) but is negligible for mesoscale motions.

Similarly, we can examine the evolution of the *available potential energy* of the

perturbation $A' \equiv \langle \frac{1}{2} b'^2 / \overline{N}^2 \rangle$, with $\overline{N}^2 \equiv N^2 + \partial \overline{b}/\partial z$ being the local stratification in the unperturbed state:

$$\frac{\partial}{\partial t} A' = - \left\langle v' b' \, \frac{1}{\overline{N}^2} \, \frac{\partial \overline{b}}{\partial y} \right\rangle - \langle w' b' \rangle$$

Thus the kinetic energy gain from the $\langle w'b' \rangle$ term comes out of the eddy potential energy. The latter is produced by north–south fluxes of buoyancy down the mean gradient. Reduction of horizontal density gradients implies that the isopycnals are, on the average, flattening out, so that the mean potential energy is decreasing.

In the simplest case of baroclinic instability, the zonal flow is independent of y; growth of perturbation kinetic energy clearly requires vertical motions so that $\langle w'b' \rangle$ is positive and $\langle v'b' \; (1/\overline{N}^2) \; (\partial \overline{b}/\partial y) \rangle$ must be strongly negative. As Eady (1949) and Charney (1947) showed, the particles tend to move at an angle to the horizontal which is about half the angle that the sloping isotherms make, so that light fluid is still rising through heavy fluid (Fig. 4.26*b*)—thus, this form of instability is sometimes called *slantwise convection*.

The effects of the vertical motions associated with baroclinic instability on oceanic biology appear in our extension of FD93 to an unstable jet. Figure 4.30 shows the flow development and the biological effects (using the mixed layer model equation 24) when the lower layer is very deep and baroclinic instability is not able to act. Even though the initial disturbance is quite large, the vertical velocities remain small and the biological perturbations are about 36% and 25% of the means for P and Z, respectively. Again as in FD93, the higher effective death rate of zooplankton (from dilution and removal to beneath the mixed layer) gives a higher phytoplankton equilibrium, while the increase in phytoplankton death rate reduces the sustainable zooplankton population even though there is influx of nutrients.

In contrast, when we use a realistic lower layer depth, we see much stronger development (Fig. 4.29) and much more biological variability (Fig. 4.31) since the vertical velocity has been increased by a factor of 6. However, we caution that some of the upwelling-induced changes may be difficult to see in the ocean; in particular, when there is a gradient in properties across the jet, it can mask the dynamical changes. Figure 4.32 illustrates this point by beginning with a change in the total nutrient by a factor of $\frac{2}{3}$ across the jet and a change in the equilibrium Z by a similar factor. The phytoplankton field shows the meandering clearly, while the zooplankton distribution looks much more like the temperature.

8.3. Instability Criterion

The generalization of Rayleigh's theorem to the stratified QG jet states that the flow will be stable if $\partial \overline{q}/\partial y$, $-(\partial \overline{b}/\partial y)|_{\text{top}}$, and $(\partial \overline{b}/\partial y)|_{\text{bottom}}$ are everywhere the same sign. (One or more of these fields may be uniformly zero, as well.) In the barotropic case, the density is horizontally uniform and instability requires a change in sign of the potential vorticity gradient, while baroclinic instability may occur when the PV gradient changes sign vertically or when the distance between the isopycnals which intersect a boundary and the boundary itself increases northward. This, too, can be thought of as a change in sign of the PV gradient:

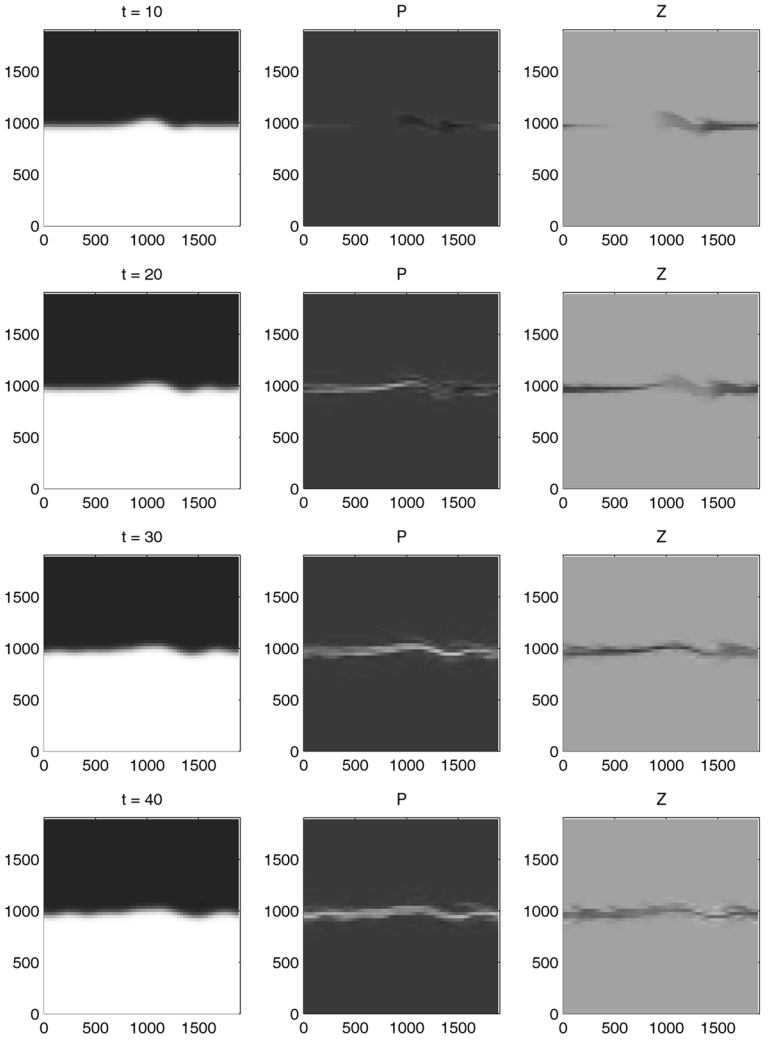

Fig. 4.30. Thermocline depth, P, and Z fields for a jet in the absence of instability. Gray scale range is 2 to 3 for P, 1.4 to 2 for Z.

$$\frac{\partial \overline{q}}{\partial y} = \frac{\partial}{\partial y} \frac{f + \zeta}{h}$$

In the interior, for the simplest case, $\partial \overline{q}/\partial y$ is positive, dominated by β. But the northward thickening of the layers near the boundary acts like a gradient that is negative. Proofs of this theorem can be found in Pedlosky (1979) and have been extended to the primitive equations by Ripa (1991). In effect, they imply that oceanic jets will be unstable. Even slow interior flows may be susceptible to growing disturbances when they are nonzonal (Charney and Flierl, 1981).

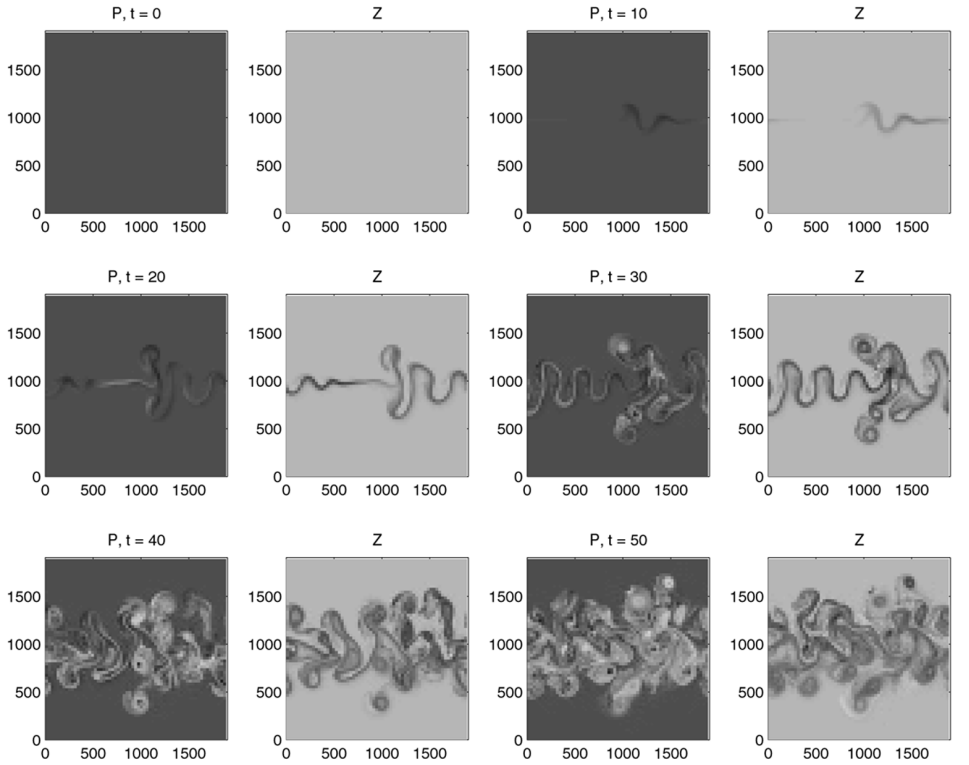

Fig. 4.31. *P* and *Z* fields for a jet with baroclinic instability. Gray scale range is 1 to 5 for *P* and 0 to 2.5 for *Z*.

9. Near-Surface/Deep-Ocean Interaction

The upper ocean plays host to a convolution of variability arising from three fundamental sources: atmospheric forcing, motions in the ocean's interior, and their interaction. For the most part, the local effects of air–sea exchange of heat, salt, and momentum are fairly well understood. These have been articulated into a set of one-dimensional physical models which are quite capable of simulating atmospherically driven changes in near-surface properties (Martin, 1985). Biological processes have been incorporated into many such models, providing a framework for analysis of the response of the plankton to these forcings (Evans and Garçon, 1997). Less well known are the direct impacts of mesoscale and submesoscale flows on upper ocean ecosystems, some of which have been described in the preceding sections. Probably the most poorly understood class of physical–biological interactions has to do with how the surface boundary layer interacts with the deep ocean. The nature of this interplay has a twofold impact on upper ocean dynamics, in that it not only supports additional mechanisms of vertical transport, but also modulates the air–sea fluxes, creating spatial variability in near-surface stratification and the depth of the mixed layer.

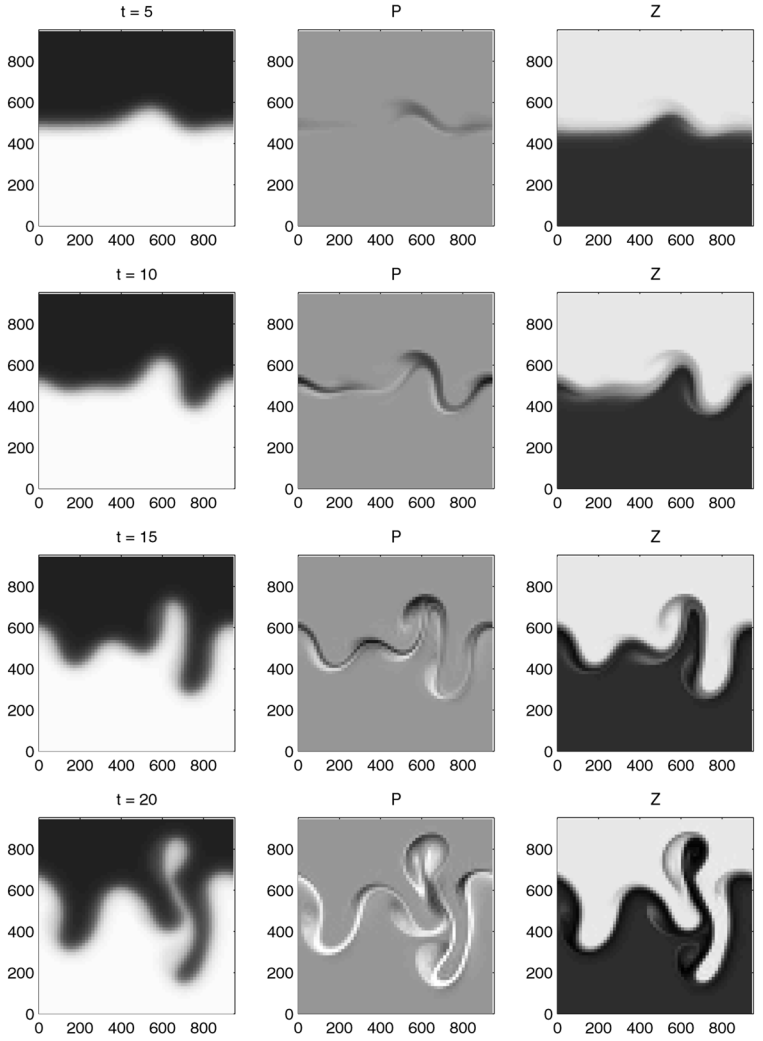

Fig. 4.32. See color insert. P and Z fields for a jet with a background gradient in N_T from 3 in the south to 8 in the north. Gray scale range is 1.7 to 2.6 for P and 1 to 2.7 for Z.

9.1. Vertical Transport Processes

Eddy Motions and the Generalized Ekman Divergence

Various researchers recognized long ago that the superposition of a wind-driven Ekman flow on a preexisting mesoscale velocity field gives rise to ageostrophic circulations involving significant vertical transports (Stern, 1965; Niiler, 1969). Submesoscale patches of vertical velocity are implied by the *generalized Ekman divergence*, which includes vortex stretching terms associated with advection of the interior vorticity field by the boundary layer velocity. For the upper ocean, vertical momentum transport can be represented as a stress-divergence term,

$$\frac{1}{\rho_0}\,\frac{\partial}{\partial z}\,\boldsymbol{\tau}$$

added to the right-hand side of the momentum equations 11; alternatively, we can write the friction in terms of the Ekman velocity:

$$f\hat{\mathbf{z}}\times\mathbf{u}_e \equiv \frac{1}{\rho_0}\,\frac{\partial}{\partial z}\,\boldsymbol{\tau}$$

We form the vertical vorticity equation by taking the curl of the momentum equations and dotting with the vertical unit vector:

$$\left(\frac{\partial}{\partial t}+\mathbf{u}\cdot\nabla+w\,\frac{\partial}{\partial z}\right)(\zeta+f)=(f\hat{\mathbf{z}}+\nabla\times\mathbf{u})\cdot\nabla w+\nabla\cdot f\mathbf{u}_e$$

In the surface layers, the horizontal velocity can be written as the sum of the geostrophic $\mathbf{u}_g$ and Ekman $\mathbf{u}_e$ flows, with the latter having large horizontal vorticity but relatively little vertical vorticity because of the large scale of the winds.[4] We can average over the depth of the Ekman frictional layer, h, taking into account that the variations in the geostrophic flow of this thin layer are negligible:

$$(f+\zeta_g)\,\frac{w(-h)}{h}\simeq\nabla\cdot f\langle\mathbf{u}_e\rangle-\langle\mathbf{u}_e\rangle\cdot\nabla(\zeta_g+f)+\left\langle\hat{\mathbf{z}}\cdot\frac{\partial}{\partial z}\,\mathbf{u}_e\times\nabla w\right\rangle$$
$$-\left(\frac{\partial}{\partial t}+\mathbf{u}_g\cdot\nabla\right)(\zeta_g+f)$$

Without the interior eddies, we would simply balance $f(w/h)$ with the divergence of the Ekman flow; the eddies alter the proportionality factor as well as add additional terms.

The detailed structure of these vertical circulations depends on the juxtaposition of two velocity fields. When the wind is uniform, the vertical motion results from vortex stretching caused by advection of the interior vorticity by the boundary layer velocity (the second term on the right). An example of this type of motion is shown in Fig. 4.33, which compares the vertical velocity patterns in an isolated eddy both with and without wind. In the case without wind [panel (*a*)], the only source of vertical velocity is vortex stretching in the interior. Alternating patches of very weak upwelling and downwelling occur around the border of the eddy as it develops slight asymmetries from its initially circular configuration. In the case with wind, a southward Ekman transport advects low ζ fluid across the northern flank of the eddy into an area of higher vorticity. The increase is produced by downwelling in that region,

[4] Since the wind stress depends on the difference between the air and water velocities, there actually can be stress variations on the oceanic mesoscale (Dewar, 1986); such processes represent another way in which the eddies and the upper ocean interact.

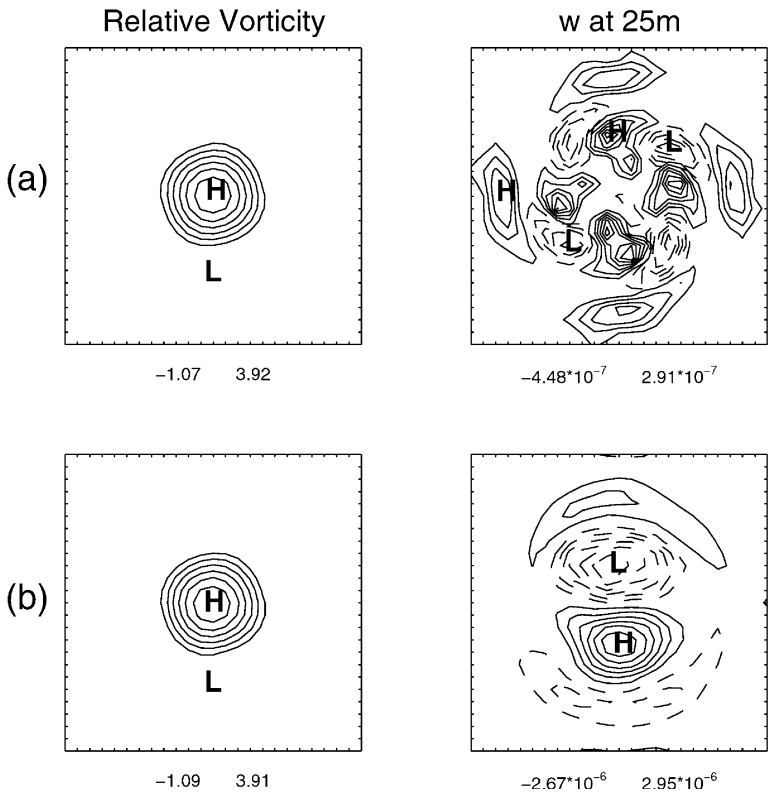

Fig. 4.33. Maps of nondimensional vorticity at 50 m and vertical velocity (m s^{-1}) at 25 m for numerical experiments (*a*) without wind and (*b*) with a 10 m s^{-1} westerly wind. Both cases are initialized with an axially symmetric vorticity distribution and integrated for 37 days with a coupled quasigeostrophic and surface boundary layer model. Numbers below each plot indicate minimum and maximum values as well as the contour interval. Note that the contour interval for vertical velocity in the case with wind is five times that used in the case without wind.

which results in vortex stretching. In the southern portion of the feature, high ζ water is advected out of the feature toward lower vorticity areas, resulting in upwelling.

The net impact of these submesoscale patches of vertical velocity caused by the interaction of the eddies and wind stress has been studied in a set of numerical experiments extending the results of MR97 (in their Section 5.5). These seasonal simulations are intended to represent a perpetual summertime situation in the oligotrophic open ocean, in which the euphotic zone (the upper 100 m) is significantly deeper than the average mixed layer (order 10 m). Any nutrients that are upwelled into the upper part of the euphotic zone (the upper 75 m, where the observed mean nitrate concentration goes to zero in summer) are assumed to be fully utilized by the biota. Below the euphotic zone, nutrients are restored to their observed concentration as a function of density via a first-order process with a remineralization time scale of three months. This particular experimental design does not treat the mixed layer explicitly, as upwelled nutrients are assumed to be fully utilized prior to reaching that depth. Diapycnal processes are included only as a background diffusivity of 1.0 m^2 s^{-1}. For more details on the numerics and general experimental design, see MR97.

TABLE II
Eddy–Wind Stress Experiments

Run	Wind Source	Experiment	Stress × 10^{-2} (N m^{-2})	Curl × 10^{-8} (N m^{-3})	EKE (cm^2 s^{-2})	Nutrient Flux (mol N m^{-2} yr^{-1})
1	None	Control	0.0	0.0	126.4	0.36 ± 0.0005
2	Climatology	Mean summer stress	3.74	0.0	262.6	0.49 ± 0.001
3	Simulated NSCAT	July–Sept. stress	1.34	2.98	90.4	0.31 ± 0.0005
4	Simulated NSCAT	Mean stress	1.34	2.98	117.5	0.38 ± 0.0007
5	Simulated NSCAT	Filtered stress	1.27	3.03	142.5	0.46 ± 0.0006
6	Simulated NSCAT	Mean filtered stress	1.27	3.03	99.3	0.37 ± 0.001
7	NSCAT	Nov. 1996 stress	6.43	10.35	130.0	0.40 ± 0.0008
8	NSCAT	Mean stress, curl	6.43	10.35	204.8	0.41 ± 0.001
9	NSCAT	Stress, no curl	6.43	10.35	83.8	0.38 ± 0.0009
10	NSCAT	Stress, no vorticity advection	6.43	10.35	168.6	0.44 ± 0.0005

A summary of the results is shown in Table II. Run 1 serves as the control, in which no wind forcing was used; this is MR97's central simulation. Their wind-driven case (run 2) used steady climatological wind. We present here eight new experiments using a variety of wind products, such as those provided by spaceborne scatterometers, which resolve spatial variability in the wind stress. The first four were produced prior to the availability of NASA's NSCAT data and used the simulated NSCAT winds described in Milliff et al. (1996). The first two (runs 3 and 4) allow us to compare the response to forcing, which includes high-wavenumber spatial structure to one having uniform winds over the domain. The average wind velocities in the two runs are the same. We then forced the model using a filtered version of these winds, with a wavenumber content like that of typical wind products derived from atmospheric general circulation models. The last four experiments are based on objectively analyzed NSCAT winds observed during November 1996. This wind product is described in Liu et al. (1998) and was kindly provided by W. Tang. The central NSCAT simulation (run 7) will be compared with one forced by the mean and two additional experiments in which the two terms of the surface boundary condition calculation are turned off, one at a time.

In this ensemble of simulations, no apparent relationship exists between either wind stress or its curl and nutrient flux into the euphotic zone (Fig. 4.34*a* and *b*). However, Figure 4.34*c* shows that nutrient flux is significantly correlated with eddy kinetic energy (EKE). The control experiment demonstrates that the eddy-induced nutrient flux is substantial, accounting for more than half the nitrogen demand in the region. This result is described in detail in MR97. Climatological wind forcing results in a 36% higher nutrient flux, which is the highest of all the experiments described herein. The simulated NSCAT runs (3 to 6) are forced at stress values that are intermediate between the control and climatological simulations, yet the resulting nutrient flux ranges from 14% lower to 28% higher than the control. Simulations utilizing NSCAT winds are forced by significantly higher stresses and curl, since the winds were derived from November observations rather than the summertime values used in previous experiments. The nutrient flux in the central NSCAT simulation (run 7) is similar to, but slightly higher than, the control run. Surprisingly, the simulation forced by the mean of these winds (run 8) results in a nutrient flux that is nearly

identical to the previous case. The final two runs show that both terms in the generalized Ekman divergence comprising the surface boundary condition appear to be important in determining EKE and nutrient flux. Elimination of the wind stress curl term (run 9) decreases EKE and nutrient flux, whereas neglecting the advection of interior vorticity by the boundary layer velocity increases them. From these experiments we conclude that vertical transport processes associated with the interaction of the wind-driven flow with the interior currents do play an important role in nutrient supply. However, the primary mechanism by whch this occurs is indirect: The eddy kinetic energy is sensitive to the wind and boundary forcing, and the nutrient flux increases for larger energy. In other words, the eddy-driven nutrient flux tends to overshadow the direct vertical transport caused by submesoscale upwelling patches associated with wind interactions.

Winds and Fronts

The preceding analysis of eddy–wind interactions is based on quasigeostrophic dynamics with a coupled surface boundary layer. Other studies have focused on wind forcing and fronts, using more complete physics in two-dimensional models of cross-frontal structure. Lee et al. (1994) used a nonhydrostatic model to simulate in more detail Niiler's (1969) problem of a mesoscale jet forced by steady winds. Diagnosis of the solutions reveals complex secondary circulations that result from the nonlinear interaction of the jet with the wind-driven flow in the Ekman layer. Franks and Walstad (1997) examined the impact of such circulations on phytoplankton patches [the subsurface chlorophyll maximum (SCM)] near fronts using a simple ecosystem model embedded in a two-dimensional primitive equation model with a surface boundary layer. Like Lee et al. (1994), they found that the orientation of the wind with respect to the front has a strong impact on the cross-frontal density contrast. Winds along the jet weaken the density gradient and tend to erode the SCM through vertical mixing. Cross-frontal wind stress sharpens the front and effectively isolates the SCM from vertical mixing. Simulations with transient forcing show that the cross-frontal scale of the SCM at any one time depends critically on the recent history of wind stress fluctuations.

9.2. Air–Sea Fluxes and Mixed Layer Depth

Mesoscale variability in the ocean can significantly affect the fluxes across the air–sea interface of properties and their distribution throughout the water column. For example, Klein and Hua (1988) showed how a steady wind-driven momentum flux operating on an eddy field can bring about spatial variations in near-surface shear, thereby creating heterogeneity in entrainment and mixed layer depth. However, the relatively low amplitude of the simulated fluctuations (order 1 m rms variation in mixed layer depth) suggests that this process is not a controlling factor in most upper ocean ecosystems. In contrast, strong mesoscale variations in mixed layer depth have been observed in warm-core rings of the Gulf Stream (Dewar, 1986) and the East Australian Current (Tranter et al., 1980). Waters in the interior of such features are more prone to convection for two reasons. First, the near-surface stratification is reduced because of the depression of the main thermocline associated with eddy formation (a direct effect). Second, during periods of cooling, heat loss to the atmosphere is enhanced relative to surrounding waters because fluid inside the eddy is so much

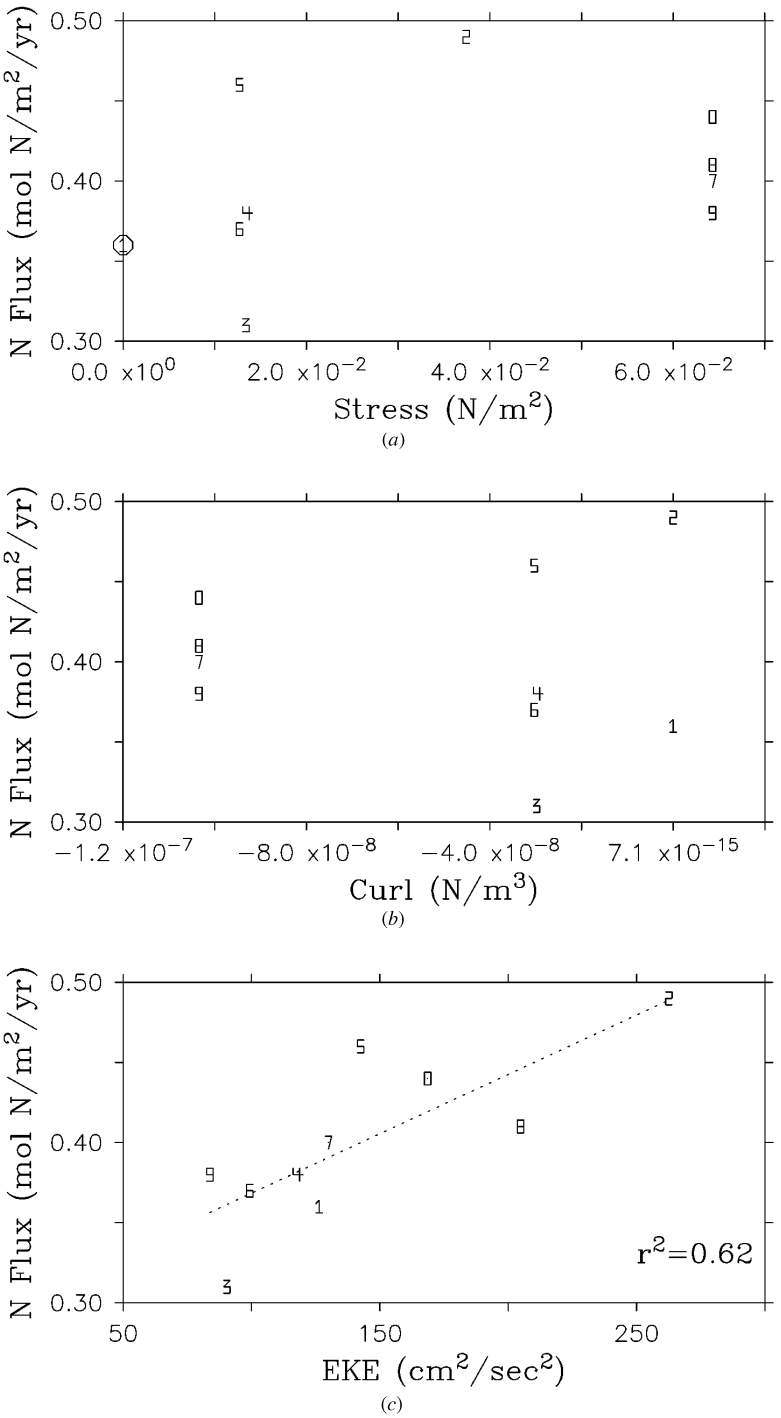

Fig. 4.34. Nutrient flux plotted as a function of (*a*) wind stress, (*b*) wind stress curl and (*c*) eddy kinetic energy for the simulations in Table II. The numerals in each panel refer to run number.

warmer. Together, these factors can contribute to very deep mixing within such features, greatly increasing nutrient supply and productivity.

Realistic simulation of the near-surface manifestation of mesoscale flows necessitates accurate representation of the baroclinic structure of the upper ocean. This requirement is particularly stringent in areas (such as the Sargasso Sea) where the mean current profile causes eddies to be surface intensified (McWilliams, 1974). MR97, for example, found six vertical levels to be adequate for the interior QG model; however, their nested surface boundary layer model (Walstad and Robinson, 1993) extends from the surface down to 250 m with 10-m resolution. The calculated physical fields have statistical properties (spatial and temporal autocorrelation functions and profiles of eddy kinetic energy) that are consistent with observations.

To determine the extent to which the MR97 calculations depend on high resolution in the near-surface region, we conducted an additional experiment, changing the coupled QG–SBL configuration so that the interior is barotropic and recomputing the MR97 simulations. The resulting amplitude of the eddy-induced nutrient flux is reduced by an order of magnitude in comparison with the more realistic case. Thus, the barotropic model is not sufficient to capture the ramifications of the cyclonic eddy formation/intensification mechanism in full. If they are to provide adequate simulations of the impact of mesoscale or submesoscale processes on upper ocean ecosystems, coupled interdisciplinary models require quite realistic physics.

10. Concluding Remarks

Wafted by a favouring gale
As one sometimes is in trances,
To a height that few can scale,
Save by long and weary dances;
W. S. Gilbert, 1885

The studies to date, including the ones presented here, argue that the mesoscale and submesoscale eddy field—the oceanic weather—does indeed play an significant role in the biological dynamics of the ocean. The vertical motions provide a mechanism for generating variability, while the horizontal motions transport and mix the biota. These processes can be examined by analytical methods such as perturbation theory (including weakly nonlinear effects), but such approaches, while providing considerable insight, are generally restricted to very simple systems.

Numerical models, on the other hand, provide a powerful framework for testing hypotheses concerning complex oceanic phenomena. Collections of diverse processes can be articulated into prognostic mathematical expressions which form a basis for simulating the behavior of the various mechanisms and their interaction. However, the oceanographic conclusions that can be drawn from such numerical experiments are also limited by the degree to which the essential characteristics of the natural system are represented. If an important aspect has been omitted in the model formulation, inferences based on the simulations can be compromised.

We have discussed a number of areas in which models are still rudimentary and where we have much to learn. In the realm of physics, the interaction between the eddy field and the surface boundary layer, especially if we factor in surface fronts and winter convection, is not yet fully explored. Other topics that touch on biologi-

cally important aspects of the eddies but which are not that well understood include stratified turbulence in the presence of shear and/or nonzonal flows, the interactions between vortices, jets, waves, and turbulence, and the role of steep topography (e.g., the shelf or islands) in mesoscale dynamics.

In the biological arena, the questions run much deeper. Can we really represent well enough the multitudinous species with different characteristics and life cycles using only a typically small number of variables? Can we get the information to parameterize the interactions in a model with many variables? To what degree does the biological system by itself have cycles or chaotic behavior, and how does that affect the eddy-driven variability? How significant is biological movement and patchiness?

As we have discussed, small changes in the biological models can make big differences in the response to the perturbations induced by the eddy movements. However, we believe that the fundamental results described in this chapter are robust:

1. Advection by mesoscale and submesoscale features is a significant factor in the local changes in biological properties. In addition, eddies produce local variability by modulating air–sea processes in both strength and timing.
2. Rossby waves, coherent vortices, and geostrophic turbulence move the biota vertically through the varying light field and can thereby generate considerable biological variability.
3. Eddies are a major mechanism for horizontal transport, via both Stokes drift and eddy diffusion.
4. The net vertical flux of nutrient induced by eddies can be significant. However, it is not clear what fraction of the total global transport is accomplished by eddies; such conclusions await better understanding of the global eddy field, the interaction with the surface boundary layer, and the rates and pathways of consumption and export.

As these points indicate, the influence of ocean eddies on the ecosystem has both local and global aspects. While both data and models confirm that any attempt to understand, simulate, or predict changes at a particular place must include the eddy motions, their role in the biology of the world's oceans is not yet clear. We now have a few simulations of the global circulation including eddy effects; however, an eddy-resolving, strongly nonlinear model is still a way off. Similarly, we have much to understand about modeling oceanic biology. However, progress is being made in both these areas, and we believe that the new and more complex experiments to come will confirm the importance of the eddies in the structure of the general circulation and in the distributions and dynamics of life in the sea.

Acknowledgments

We would like to acknowledge support for this work by grants from NSF (OCE-9525809, OPP-9910052 and OCE-9725974, OCE-9632540), ONR (N00014-98-1-0608), NASA (NAG5-6455) and JPL (960517). Reviews from J. S. Wroblewski and D. B. Olson were extremely helpful in revision and clarification of the manuscript. This is U.S. JGOFS contribution 645 and WHOI contribution 10281.

References

Angel, M. V. and M. J. R. Fasham, 1983. Eddies and biological processes. In *Eddies in Marine Science*, A. R. Robinson, ed. Springer-Verlag, New York.

Aref, H., 1983. Integrable, chaotic, and turbulent vortex motions in two-dimensional flows. *Annu. Rev. Fluid Mech.*, **15,** 345–389.

Bower, A. S., 1991. A simple kinematic mechanism for mixing fluid parcels across a meandering jet. *J. Phys. Oceanogr.*, **21,** 173–180.

Bower, A. and H. Rossby, 1989. Evidence of cross-frontal exchange processes in the Gulf Stream based on isopycnal RAFOS float data. *J. Phys. Oceanogr.*, **19,** 1177–1190.

Bryden, H., 1979. Poleward heat flux and conversion of available potential energy in the Drake Passage. *J. Mar. Res.*, **37,** 1–22.

Caswell, H., 1989. *Matrix Population Models: Construction, Analysis, and Interpretation.* Sinauer Associates, Sunderland, Mass.

Charney, J. G., 1947. The dynamics of long waves in a baroclinic westerly current. *J. Meteorol.*, **4,** 135–163.

Charney, J. G. and G. R. Flierl, 1981. Oceanic analogues of large-scale atmospheric motions. In *Evolution of Physical Oceanography (Scientific Surveys in Honor of Henry Stommel*), B. A. Warren and C. Wunsch, eds. MIT Press, Cambridge, Mass., pp. 504–548.

Davis, C. S., 1984. Interaction of a copepod population with the mean circulation on Georges Bank. *J. Mar. Res.*, **42,** 573–590.

Dewar, W., 1986. Mixed layers in Gulf Stream rings. *Dyn. Atmos. Oceans*, **10,** 1–29.

Dewar, W. K. and G. R. Flierl, 1985. Particle trajectories and simple models of tracer transport in coherent vortices. *Dyn. Atmos. Oceans*, **9,** 215–252.

Eady, E. T., 1949. Long waves and cyclone waves. *Tellus*, **1,** 258–277.

Evans, G. and V. Garçon, 1997. One-dimensional models of water column biogeochemistry. *Tech. Rep. JGOFS Report 23/97.* JGOFS, Bergen, Norway.

Fasham, M. J. R., H. W. Ducklow and S. M. McKelvie, 1990. A nitrogen-based model of plankton dynamics in the oceanic mixed layer. *J. Mar. Res.*, **48,** 591–639.

Flierl, G. R., 1981. Partcle motions in large amplitude wave fields. *Geophys. Astrophys. Fluid Dyn.*, **18,** 39–74.

Flierl, G. R., 1987. Isolated eddy models in geophysics. *Annu. Rev. Fluid Mech.*, **19,** 493–530.

Flierl, G. R. and C. S. Davis, 1993. Biological effects of Gulf Stream meandering. *J. Mar. Res.*, **51,** 529–560.

Flierl, G. R. and R. P. Mied, 1985. Frictionally-induced circulations and spin-down of a warm core ring. *J. Geophys. Res.*, **90**(C5), 8917–8927.

Flierl, G. R. and J. W. Wroblewski, 1985. The possible influence of warm core rings upon shelf water larval fish distributions. *Fish. Bull.*, **83**(3), 313–330.

Franks, P. and L. Walstad, 1997. Phytoplankton patches at fronts: a model of formation and response to wind events. *J. Mar. Res.*, **55,** 1–29.

Franks, P. J. S., J. S. Wroblewski and G. R. Flierl, 1986. Prediction of phyto-plankton growth in response to the frictional decay of a warm core ring. *J. Geophys. Res.*, **91**(C6), 7603–7610.

Frost, B. W., 1993. A modeling study of processes regulating plankton standing stock and production in the open subarctic Pacific Ocean. *Prog. Oceanogr.*, **32,** 17–56.

Hastings, A. and T. Powell, 1991. Chaos in a three-species food chain. *Ecology*, **72,** 896–903.

Haury, L. R., J. A. McGowen and P. H. Wiebe, 1978. Patterns and processes in the time–space scale of plankton distribution. In *Spatial Patterns in Plankton Communities*, J. H. Steele, ed. Plenum Press, New York.

Hebert, D., N. Oakey and B. Ruddick, 1990. Evolution of a Mediterranean salt lens: scalar properties. *J. Phys. Oceanogr.*, **20,** 1468–1483.

Holloway, G., 1984. Effects of velocity fluctuations on vertical distributions of phytoplankton. *J. Mar. Res.*, **42,** 559–571.

Ivlev, V. S., 1995. *Experimental Ecology of the Feeding of Fishes.* Pischepromizdat, Moscow. Translated from Russian by D. Scott. Yale University Press, New Haven, Conn., 1961.

Joyce, T. M., 1988. On regulation of primary production by physical processes in the ocean: two case studies. In *Toward a Theory on Biological–Physical Interactions in the World Ocean*, B. J. Rothschild, ed. D. Reidel, Dordrecht, The Netherlands.

Klein, P. and B. Hua, 1988. Mesoscale heterogeneity of the wind-driven mixed layer: influence of a quasigeostrophic flow. *J. Mar. Res.*, **46,** 495–525.

Lee, D., P. Niiler, A. Warn-Varnas and S. Piacsek, 1994. Wind-driven secondary circulation in ocean mesoscale. *J. Mar. Res.*, **52,** 371–396.

Legg, S. and J. Marshall, 1993. A heton model of the spreading phase of open-ocean deep convection. *J. Phys. Oceanogr.*, **23,** 1040–1056.

Liu, W., W. Tang and P. Polito, 1998. Spacebased observation of global ocean surface wind. In *Proceedings of the 2nd Symposium of Integrating Observing System.* American Meteorological Society, Boston.

Lobel, P. S. and A. R. Robinson, 1986. Transport and entrapment of fish larvae by ocean mesoscale eddies and current in Hawaiian waters. *Deep-Sea Res.*, **33,** 483–500.

Marquet, P. A., M.-J. Fortin, J. Pineda, D. O. Wallin, J. Clark, Y. Wu, S. Bollins, C. M. Jacobi and R. D. Holt, 1993. Ecological and evolutionary consequences of patchiness: a marine–terrestrial perspective. In *Patch Dynamics*, S. A. Levin, T. M. Powell and J. H. Steele, eds. Springer-Verlag, Berlin, pp. 277–304.

Martin, P. J., 1985. Simulation of the mixed layer at OWS November and Papa with several models. *J. Geophys. Res.*, **90,** 903–916.

McGillicuddy, D. and A. Robinson, 1997a. Eddy induced nutrient supply and new production in the Sargasso Sea. *Deep-Sea Res.*, **44,** 1427–1449.

McGillicuddy, D. and A. Robinson, 1997b. Interaction between the oceanic mesoscale and the surface mixed layer. *Dyn. Atmos. Oceans*, **27,** 549–574.

McGillicuddy, D., A. Robinson and J. McCarthy, 1995. Coupled physical and biological modeling of the spring bloom in the North Atlantic. 2. Three dimensional bloom and post-bloom effects. *Deep-Sea Res.*, **42,** 1359–1398.

McGillicuddy, D., A. Robinson, D. Siegel, H. Jannasch, R. Johnson, T. Dickey, J. McNeil, A. Michaels and A. Knap, 1998. Influence of mesoscale eddies on new production in the Sargasso Sea. *Nature*, **394,** 263–265.

McGillicuddy, D., R. Johnson, D. Siegel, A. Michaels, N. Bates and A. Knap, 1999. Mesoscale variations of biogeochemical properties in the Sargasso Sea. *J. Geophys. Res.*, **104**(C6), 13381–13394.

McNeil, J., H. Jannasch, T. Dickey, D. McGillicuddy, M. Brzezinski and C. Sakamoto, (1999). New chemical, bio-optical and physical observations of upper ocean response to the passage of a mesoscale eddy. *J. Geophys. Res.*, **104**(C7), 15537–15548.

McWilliams, J., 1974. MODE mean currents and eddy surface intensification. *MODE Hotline News*, **57,** 1–6.

McWilliams, J. C., 1976. Maps from the mid-ocean dynamics experiment. II. Potential vorticity and its conversion. *J. Phys. Oceanogr.*, **6,** 823–846.

McWilliams, J. C. and G. R. Flierl, 1979. On the evolution of isolated, nonlinear vortices. *J. Phys. Oceanogr.*, **9,** 1155–1182.

Meacham, S. P., 1991. Meander evolution on quasigeostrophic jets. *J. Phys. Oceanogr.*, **21,** 1139–1170.

Michaelis, L. and M. L. Menten, 1913. Die kinetic der invertinwirkung. *Biochemische Zeitschrift*, **49,** 333–369.

Milliff, R., W. Large, W. Holland and J. McWilliams, 1996. The general circulation responses of high-resolution North Atlantic ocean models to synthetic scatterometer winds. *J. Phys. Oceangr.*, **26,** 1747–1768.

Moisan, J. R. and E. E. Hofmann, 1996. Modeling nutrient and plankton processes in the coastal transition zone. 1. A time- and depth-dependent model. *J. Geophys. Res.*, **101,** 22693–22704.

Murray, J. D., 1990. *Mathematical Biology.* Springer-Verlag, Heidelberg.

Nelson, D., J. McCarthy, T. Joyce and H. Ducklow, 1989. Enhanced near-surface nutrient availability and new production resulting from the frictional decay of a Gulf Stream warm-core ring. *Deep-Sea Res.*, **36,** 705–714.

Niiler, P. P., 1969. On the Ekman divergence in an oceanic jet. *J. Geophys. Res.*, **74,** 7048–7052.

Olson, D. B., 1980. The physical oceanography of two rings observed by the cyclonic ring experiment. Part II: Dynamics. *J. Phys. Oceanogr.*, **10**(4), 514–528.

Olson, D. B. and R. R. Hood, 1994. Modelling pelagic biogeography. *Prog. Oceanogr.*, **34,** 161–205.

Onken, R., 1992. Mesoscale upwelling and density finestructure in the seasonal thermocline: a dynamical model. *J. Phys. Oceanogr.*, **22,** 1257–1273.

Oschlies, A. and V. Garçon, 1998. Eddy-induced enhancement of primary production in a model of the North Atlantic Ocean. *Nature*, **394,** 266–269.

Pascual, M. 1993. Diffusion-induced chaos in a spatial predator–prey system. *Proc. R. Soc. London Ser. B*, **25,** 1–7.

Pedlosky, J., 1979. *Geophysical Fluid Dynamics.* Springer-Verlag, New York.

Pollard, R. and L. Regier, 1992. Vorticity and vertical circulation at an ocean front. *J. Phys. Oceanogr.*, **22,** 609–625.

Richardson, P., 1983. Gulf Stream rings. In *Eddies in Marne Science*, A. R. Robinson, ed. Springer-Verlag, New York, pp. 18–45.

Richardson, P., 1993. A census of eddies observed in North Atlantic SOFAR float data. *Prog. Oceanogr.*, **31,** 1–50.

Ring Group, 1981. Gulf Stream rings: their physics, chemistry and biology. *Science*, **212**(4499), 1091–1100.

Ripa, P., 1991. General stability conditions for a multi-layer model. *J. Fluid Mech.*, **222,** 119–137.

Robinson, A. R., ed., 1983. *Eddies in Marine Science.* Springer-Verlag, New York.

Robinson, A. R., 1997. On the theory of advective effects on biological dynamics in the sea. *Proc. R. Soc. London Ser. A*, **453,** 2295–2324.

Rothschild, B. J. and T. R. Osborn, 1988. Small-scale turbulence and plankton contact rates. IRL Press, Eynsham, Oxford, England, pp. 465–474.

Sarmiento, J. L., R. D. Slater, M. J. R. Fasham, H. W. Ducklow, J. R. Toggweiler and G. T. Evans, 1993. A seasonal three-dimensional ecosystem model of nitrogen cycling in the North Atlantic euphotic zone. *Global Biogeochem. Cycles*, **7,** 417–450.

Siegel, D. A., 1998. Resource competition in a discrete environment: why are plankton distributions paradoxical? *Limnol. Oceanogr.*, **43,** 1133–1146.

Siegel, D., D. McGillicuddy and E. Fields, 1999. Mesoscale eddies, satellite altimetry and new production in the Sargasso Sea. *J. Geophys. Res.* **104**(C6), 13,359–13,379.

Sinclair, M., 1988. *Marine Populations: An Essay on Population Regulation and Speciation.* Washington Sea Grant Program, Seattle, Wash.

Steele, J. H., 1974. *The Structure of Marine Ecosystems.* Harvard University Press, Cambridge, Mass.

Steele, J. H. and E. W. Henderson, 1981. A simple plankton model. *Am. Nat.*, **117,** 676–691.

Stern, M. E., 1965. Interaction of a uniform wind stress with a geostrophic vortex. *Deep-Sea Res.*, **12,** 355–367.

Stokes, G. G., 1847. On the theory of oscillatory waves. *Trans. Cambridge Philos. Soc.*, **8,** 441–455.

Stommel, H., 1963. Varieties of oceanographic experience. *Science*, **139,** 572–576.

Strass, V. 1992. Chlorophyll patchiness caused by mesoscale upwelling at fronts. *Deep-Sea Res.*, **39,** 75–96.

Strogatz, S. H., 1994. *Nonlinear Dynamics and Chaos; With Applications in Physics, Biology, Chemistry, and Engineering*. Addison Wesley Longman, Reading, Mass.

Taylor, G. I., 1921. Diffusion by continuous movements. *Proc. London Math. Soc. A*, **20,** 196–211.

Tranter, D., R. Parker and G. Cresswell, 1980. Are warm-core eddies unproductive? *Nature*, **284,** 540–542.

Truscott, J. E. and J. Brindley, 1994. Ocean plankton populations as excitable media. *Bull. Math. Biol.*, **56,** 981–998.

Varga, R. S., 1962. *Matrix Iterative Analysis*. Prentice-Hall, Englewood Cliffs, N.J., pp. 253–255. See also G. H. Golub and C. F. Van Loan, 1996. *Matrix Computations.* Johns Hopkins University Press, Baltimore.

Walstad, L. and A. Robinson, 1993. A coupled surface boundary layer: quasigeostrophic model. *Dyn. Atmos. Oceans.*, **18,** 151–207.

Werner, F. E., R. I. Perry, R. G. Lough and C. E. Naimie, 1996. Trophodynamic and advective influences on Georges Bank larval cod and haddock. *Deep-Sea Res.*, **43,** 1793–1822.

Woods, J., 1988. Mesoscale upwelling and primary production. In *Toward a Theory on Biological–Physical Interactions in the World Ocean*, B. Rothschild, ed. D. Reidel, Dordrecht, The Netherlands.

Wroblewski, J. S., 1980. A simulation of *Acartia clausi* during Oregon upwelling, August 1973. *J. Plankton Res.*, **2,** 43–68.

Wroblewski, J. S. and J. J. O'Brien, 1981. On modeling the turbulent transport of passive biological variables in aquatic ecosystems. *Ecol. Model.*, **12,** 29–44.

DO NOT PRINT

THIS PAGE INTENTIONALLY LEFT BLANK